

THESIS

UNSTEADY REYNOLDS-AVERAGED NAVIER-STOKES SIMULATIONS OF INLET
FLOW DISTORTION IN THE FAN SYSTEM OF A GAS-TURBINE AERO-ENGINE

Submitted by

Nathan Spotts

Department of Mechanical Engineering

In partial fulfillment of the requirements

For the Degree of Master of Science

Colorado State University

Fort Collins, Colorado

Fall 2015

Master's Committee:

Advisor: Xinfeng Gao

Stephen Guzik
Hiroshi Sakurai
Goldino Alves
Jianguo Liu

Copyright by Nathan Spotts 2015

All Rights Reserved

ABSTRACT

UNSTEADY REYNOLDS-AVERAGED NAVIER-STOKES SIMULATIONS OF INLET FLOW DISTORTION IN THE FAN SYSTEM OF A GAS-TURBINE AERO-ENGINE

As modern trends in commercial aircraft design move toward high-bypass-ratio fan systems of increasing diameter with shorter, nonaxisymmetric nacelle geometries, inlet distortion is becoming common in all operating regimes. The distortion may induce aerodynamic instabilities within the fan system, leading to catastrophic damage to fan blades, should the surge margin be exceeded. Even in the absence of system instability, the heterogeneity of the flow affects aerodynamic performance significantly. Therefore, an understanding of fan-distortion interaction is critical to aircraft engine system design.

This thesis research elucidates the complex fluid dynamics and fan-distortion interaction by means of computational fluid dynamics (CFD) modeling of a complete engine fan system; including rotor, stator, spinner, nacelle and nozzle; under conditions typical of those encountered by commercial aircraft. The CFD simulations, based on a Reynolds-averaged Navier-Stokes (RANS) approach, were unsteady, three-dimensional, and of a full-annulus geometry. A thorough, systematic validation has been performed for configurations from a single passage of a rotor to a full-annulus system by comparing the predicted flow characteristics and aerodynamic performance to those found in literature. The original contributions of this research include the integration of a complete engine fan system, based on the NASA rotor 67 transonic stage and representative of the propulsion systems in commercial aircraft, and a benchmark case for unsteady RANS simulations of distorted flow in such a geometry

under realistic operating conditions. This study is unique in that the complex flow dynamics, resulting from fan-distortion interaction, were illustrated in a practical geometry under realistic operating conditions. For example, the compressive stage is shown to influence upstream static pressure distributions and thus suppress separation of flow on the nacelle. Knowledge of such flow physics is valuable for engine system design.

ACKNOWLEDGEMENTS

The research for this thesis would not have been possible without the support and guidance of numerous people, to whom I am very grateful.

I would like to express my deepest gratitude to my advisor, Prof. Xinfeng Gao, who has guided me through my M.S. study and research with enthusiasm, patience, and wisdom. I am very grateful to her for affording me many incredible opportunities, imparting her sense of curiosity, and demanding meticulousness from me. I thank her for her guidance and teaching.

I would like to thank my M.S. committee; Prof. Stephen Guzik, Prof. Hiroshi Sakurai, Dr. Dino Alves, and Prof. James Liu; for their advice, insight, and difficult questions. Also, Prof. Thong Dang from Syracuse University has been of great help in understanding the physics of turbomachinery flows, and for that I thank him.

I am grateful to Boeing Commercial Aircraft and Boeing Research & Technology for defining the direction of this research and for financial support. I thank Mark Reissig, Sho Sato, Hin-Fan Lau, Nathan Packard, Robert Moody, and Paul Park for many interesting discussions, practical suggestions and for their patience as I learned many new things. For their strong technical support, I am very appreciative of Metacomp Technologies, Inc.

I am grateful to my parents; Dr. Robert Spotts, Judy Spotts, and Kim Spotts; for their assistance throughout my academic career and am especially grateful to my father for involving me in science at an early age. I thank Howard Reichmuth for first introducing me to the joys of engineering and for inspiring me to further my abilities to understand the physical world. I am grateful to Kevin Hedin for his friendship, advice, and humor.

Lastly and most importantly, I am deeply and forever indebted to my wife, Kevin Miller, for her continual support, encouragement, love, and understanding; without which I would not have completed this work. She has been a constant source of strength, and I am very grateful to her.

TABLE OF CONTENTS

Abstract	ii
Acknowledgements	iv
List of Tables	viii
List of Figures	ix
Chapter 1. Introduction	1
1.1. Motivation and Thesis Objectives	1
1.2. Thesis Organization	2
1.3. Literature Review	3
Chapter 2. Geometric Modeling of the Engine Fan System	11
2.1. Physical Component Geometries and Configurations	11
2.2. Computational Model of the Engine Fan System	11
Chapter 3. URANS Modeling of the Engine Fan System	29
3.1. Compressible Navier-Stokes Equations	29
3.2. Averaging Concepts	31
3.3. Favre-Averaged Navier-Stokes Equations	34
3.4. Turbulence Models	35
3.5. CFD++ Solver and Solution Methods	36
3.6. Simulation Considerations for Single Stage and Full Annulus	36
3.7. Computational Resources and Costs	40
3.8. Data Post-Processing	41

Chapter 4. Results and Discussions	48
4.1. Single Passage	48
4.2. 3D Full Annulus	93
Chapter 5. Conclusions and Future Work	104
5.1. Conclusions	104
5.2. Future Work	105
Bibliography	106
Appendix A. Turbulence Models and Near-Wall Turbulence Treatment	110
A.1. Turbulence Models	110
A.2. Near-Wall Turbulence Treatment	114
Appendix B. Data Post-Processing Scripts for Single-Passage Rotor-Alone Simulations	117
B.1. Bash script for calculating performance using both rake and slice integration..	117
B.2. Tecplot macro called by Bash script in Appendix A.1	121
B.3. MATLAB script to compute circumferential averages; called by Bash script in Appendix A.1	124
B.4. MATLAB script to compute aerodynamic performance; called by Bash script in Appendix A.1	126

LIST OF TABLES

2.1	Characteristic parameters for the rotor-alone operating at 100% of design speed..	11
2.2	Pairs of grids with identical cells in J topology regions	18

LIST OF FIGURES

1.1	Contours of relative Mach number, near peak efficiency. The heavy line is at $M = 1.0$ with contour increments of 0.05. [1]	5
1.2	Isometric view of the computational domain. [2]	9
1.3	Unwrapped blade-to-blade snapshot at 90% span of stagnation pressure and temperature and static pressure. [2]	10
2.1	Representative blade sections of the rotor (left) and stator (right) at three spanwise locations: hub (black), midspan (blue) and shroud (red).	12
2.2	Multiple nozzle sizes used for single-passage calculations of stage performance with nacelle and nozzle at various operating conditions.	13
2.3	Detail of multiple nozzle sizes used for single-passage calculations of stage performance with nacelle and nozzle at various operating conditions.	13
2.4	Geometric configurations shown in the meridional plane. (a) rotor-alone with annular flow path, (b) rotor alone with center-body, (c) stage, and (d) stage with nacelle and nozzle.	14
2.5	Series of grids created by uniform coarsening, shown near the midspan as contiguous passages from fine (top) to extra coarse (bottom).	16
2.6	Coarse rotor grid used for URANS calculations, shown near the midspan.	19
2.7	Grid in the tip clearance region at the leading edge of the rotor.	20
2.8	Grid topology in rotor fillet region.	21
2.9	Surface grids for rotor-alone grid (coarse). The moving surfaces are shown in black and the stationary surfaces are shown in blue. Two passages are shown.	21

2.10	Periodic boundary of rotor grid (coarse) shown on the meridional plane with core rotor zone shown in black and inlet and outlet extension block shown in blue. ...	22
2.11	Rotor and stator grids (coarse) shown near the midspan.	23
2.12	Periodic boundary of coarse grid for the stage with center-body, shown on the meridional plane with rotor zone in black.	23
2.13	Isometric view of full-annulus grid used for URANS simulations with circumferential distortion.	24
2.14	Surface mesh (excluding mesh at shroud) of full-annulus grid used for URANS simulations with circumferential distortion.	25
2.15	Surface mesh at the shroud of full-annulus grid used for URANS simulations with circumferential distortion.	26
2.16	Periodic boundary of single-passage grids for geometric configurations including nacelle and nozzle, shown on the meridional plane.	28
2.17	Single-passage grids for geometric configurations including nacelle and nozzle. ...	28
3.1	Aerodynamic survey stations and locations for laser anemometry data in the meridional plane. Figure taken from [3].	46
3.2	Schematic representations of constant pitch lines (left) and constant chord lines (right) used to plot data in streamwise and blade-to-blade directions, respectively. Figure adapted from [3]	46
4.1	Relative Mach number at 10% span from the shroud and at 50% pitch, for the rotor alone operating near peak efficiency.	49

4.2	Relative Mach number at 30% span from the shroud and at 50% pitch, for the rotor alone operating near peak efficiency.	51
4.3	Relative Mach number at 70% span from the shroud and at 50% pitch, for the rotor alone operating near peak efficiency.	53
4.4	Relative Mach number at 10% span from the shroud and at 50% pitch, for the rotor alone operating near stall.	55
4.5	Relative Mach number at 30% span from the shroud and at 50% pitch, for the rotor alone operating near stall.	56
4.6	Relative Mach number at 70% span from the shroud and at 50% pitch, for the rotor alone operating near stall.	56
4.7	Relative Mach number at 10% (top), 30% (middle), and 70% (bottom) span from the shroud and at 63% (top-left), 188% (top-right), 25% (middle-left), 136% (middle-right), 30% (bottom-left), 121% (bottom-right) chord, for the rotor alone operating near peak efficiency.	58
4.8	Relative Mach number at 10% (top), 30% (middle), and 70% (bottom) span from the shroud and at 20% (top-left), 123% (top-right), 20% (middle-left), 118% (middle-right), 7.5% (bottom-left), 110% (bottom-right) chord, for the rotor alone operating near stall.	59
4.9	Spanwise distributions of total pressure (top-left), total temperature (top-right), static pressure (bottom-left), and exit flow angle (bottom-right) for the rotor alone operating near peak efficiency.	61

4.10	Spanwise distributions of total pressure (top-left), total temperature (top-right), static pressure (bottom-left), and exit flow angle (bottom-right) for the rotor alone operating near stall.	62
4.11	Contours of relative Mach number for the rotor alone operating at peak efficiency. Experimental (left) and CFD results were calculated on a grid with 2.8×10^7 cells and $y_1^+ < 1$ (right); 10% span from the shroud (top), 30% span from the shroud (middle), and 70% span from the shroud (bottom).	64
4.12	Contours of relative Mach number for the rotor alone operating near stall. Experimental (left) and CFD results were calculated on grid with 2.8×10^7 cells and $y_1^+ < 1$ (right); 10% span from the shroud (top), 30% span from the shroud (middle), and 70% span from the shroud (bottom).	66
4.13	Contours of relative Mach number at 10% span from the shroud for the rotor alone operating at peak efficiency; 2.3×10^5 cells (top-left), 4.3×10^5 cells with $y_1^+ < 1$ (top-right), 1.9×10^6 cells (middle-left), 3.5×10^6 cells with $y_1^+ < 1$ (middle-right), 1.5×10^7 cells (bottom-left), and 2.8×10^7 cells with $y_1^+ < 1$ (bottom-right)	68
4.14	Contours of relative Mach number at 10% span from the shroud for the rotor alone operating near stall; 2.3×10^5 cells (top-left), 4.3×10^5 cells with $y_1^+ < 1$ (top-right), 1.9×10^6 cells (middle-left), 3.5×10^6 cells with $y_1^+ < 1$ (middle-right), 1.5×10^7 cells (bottom-left), and 2.8×10^7 cells with $y_1^+ < 1$ (bottom-right)	69
4.15	Isentropic efficiency for the rotor alone operating at 100% of design speed.	71
4.16	Total pressure for the rotor alone operating at 100% of design speed.	72
4.17	Total pressure for the rotor alone operating at 100% of design speed; rake integration and slice integration shown for coarse grid series.	74

4.18	Total pressure for the rotor alone operating at 100% of design speed; rake integration and slice integration shown for coarse grid series.	75
4.19	Total pressure for the rotor alone operating at 100% of design speed; rake integration and slice integration shown for fine grid series.	76
4.20	Total pressure for the rotor alone operating at 100% of design speed; rake integration and slice integration shown for fine grid series.	77
4.21	Relative Mach number at 10% span from the shroud and at 50% pitch, for the rotor alone operating near peak efficiency with four turbulence models.	78
4.22	Relative Mach number at 30% span from the shroud and at 50% pitch, for the rotor alone operating near peak efficiency with four turbulence models.	79
4.23	Relative Mach number at 70% span from the shroud and at 50% pitch, for the rotor alone operating near peak efficiency with four turbulence models.	80
4.24	Spanwise distributions of total pressure (top-left), total temperature (top-right), static pressure (bottom-left), and exit flow angle (bottom-right) for the rotor alone operating near peak efficiency with four turbulence models.	81
4.25	Contours of relative Mach number at 10% span from the shroud for the rotor alone operating at peak efficiency; 2.3×10^5 cells; S-A model (top-left), $k-\epsilon$ model (top-right), cubic $k-\epsilon$ model (bottom-left), and SST model (bottom-right).	82
4.26	Isentropic efficiency for the rotor alone simulated with four turbulence models. ...	84
4.27	Total pressure ratio for the rotor alone operating near peak efficiency with four turbulence models.	85

4.28	Isentropic efficiency for the rotor alone, with annular and center-body flowpaths, operating at 100% of design speed.	86
4.29	Total pressure for the rotor alone, with annular and center-body flowpaths, operating at 100% of design speed.	87
4.30	Isentropic efficiency for the rotor alone, with center-body flowpath, operating at 60%, 70%, 80%, 90% and 100% of design speed, from left to right.	88
4.31	Total pressure ratio for the rotor alone, with center-body flowpath, operating at 60%, 70%, 80%, 90% and 100% of design speed.	89
4.32	Isentropic efficiency for the stage operating at 70%, 80%, 90% and 100% of design speed.	90
4.33	Total pressure ratio for the stage operating at 70%, 80%, 90% and 100% of design speed.	91
4.34	Isentropic efficiency ratio across the rotor for stage with nacelle and nozzle at static, take-off and cruise conditions. Reference isentropic efficiency is from rotor-alone simulation.	92
4.35	Total pressure ratio across the rotor for stage with nacelle and nozzle at static, take-off and cruise conditions. Reference total pressure ratio is from rotor-alone simulation.	93
4.36	Total pressure at inlet (left) and at approximately 2 chords upstream of the rotor (right).	94
4.37	Contours of absolute whirl angle in degrees (left) and meridional flow angle in degrees (right) at a station approximately 2 chord lengths upstream of the rotor. .	95

4.38	Absolute whirl angle (left) and mass flux distribution $\left(\frac{\rho U}{\rho U_{\text{inlet, clean}}}\right)$ (right) at the leading edge of the rotor.	96
4.39	Total pressure downstream of rotor for time-averaged solution (left) and time-pitch-averaged solution (right).	97
4.40	Total temperature (left) and static pressure (right) downstream of rotor for time-pitch-averaged solution.	97
4.41	Total pressure downstream of stator for time-averaged solution (left) and time-pitch-averaged solution (right).	98
4.42	Total temperature (left) and absolute whirl angle (right) downstream of stator for time-pitch-averaged solution.	98
4.43	Total pressure $\left(\frac{P_0}{P_{0\text{inlet, clean}}}\right)$ contours for an unwrapped constant radius slice at 90% span at the rotor's trailing edge.	99
4.44	Total temperature $\left(\frac{T_0}{T_{0\text{inlet, clean}}}\right)$ contours for an unwrapped constant radius slice at 90% span at the rotor's trailing edge.	99
4.45	Static pressure $\left(\frac{P - P_{0\text{inlet, clean}}}{P_{0\text{inlet, clean}} - P_{\text{avg, stn1}}}\right)$ contours for an unwrapped constant radius slice at 90% span at the rotor's trailing edge.	100
4.46	Contours of total pressure on a planar slice defined by the in-flow direction and axis of rotation, showing free jet dissipation. $M_\infty = 0.25$	101
4.47	Total pressure contours, volume streamlines colored by total pressure, and surface streamlines for configurations without the fan stage (left) and with the fan stage (right), both passing the same mass flow and at 30° AOA.	102

- 4.48 Contours of total pressure on a planar slice defined by AOA vector and axis of rotation; without the fan stage (left) and with the fan stage (right). $M_\infty = 0.25$.. 102
- 4.49 Contours of static pressure on a planar slice defined by AOA vector and axis of rotation; without the fan stage (left) and with the fan stage (right). $M_\infty = 0.25$.. 103

CHAPTER 1

INTRODUCTION

1.1. MOTIVATION AND THESIS OBJECTIVES

Inlet flow distortion is a matter of concern in gas-turbine aircraft engines due to its potential to destabilize the engine to such an extent that severe damage may occur. As modern trends in commercial aircraft design move toward high-bypass-ratio fan systems of increasing diameter with shorter, nonaxisymmetric nacelle geometries, inlet distortion during all operating regimes is becoming common. Consequently, an understanding of fan-distortion interaction as well as both the causes and effects of this interaction with relation to the fan system and surrounding components is critical to aircraft engine system design. Specifically, such an understanding will facilitate the future integration of commercial aircraft propulsion system components in a manner that mitigates the risks associated with fan system inlet distortion.

Moreover, ongoing advances in computing power and computational sciences have made high-fidelity numerical simulations an ever more attainable approach by which to elucidate the physics of complex fluid flows associated with the inlet distortion problem. Because the large degree of heterogeneity in inlet distortion flow quantities makes axisymmetric or pitchwise periodic assumptions invalid, simulations of fan-distortion interaction must include the whole annulus. Additionally, the interaction of such heterogeneous inflows with rotating blade rows is inherently unsteady, simulations must be time-accurate.

The objective of this thesis research is to perform unsteady Reynolds-Averaged Navier-Stokes simulations of the NASA 67 transonic stage with inlet distortion representative of that found in the fan system of a commercial aircraft; thus improving our understanding of

the issues related to the performance and design of the fan system. To achieve this goal, the following sub-objectives have been completed. Firstly, CAD geometry was created for the rotor, stator, and various flow paths. Secondly, an in-depth validation study was performed for the rotor alone, operating with clean inlet flow and at 100% of the design speed. This validation assessment was completed using steady-state, single-passage CFD simulations, the results of which were compared to experimental data of the detailed flow field and of the rotor's aerodynamic performance. Subsequently, single-passage simulations of both the rotor in isolation and in a rotor-stator stage configuration were performed for the rotor operating at various speeds. Operating lines for the two configurations at various speeds were validated using additional experimental data. Full-annulus simulations of the stage with circumferential inlet distortion were completed to replicate recent results by Fidalgo *et al* [2]. A series of nozzle geometries were created and added to the stage, as was a nacelle geometry. Single-passage simulations were performed for the complete system (rotor, stator, nacelle, and nozzle) operating in freestream conditions comparable to the static, take-off, and cruise conditions of a typical commercial aircraft. Finally, full-annulus unsteady Reynolds-averaged Navier-Stokes (URANS) simulations of the complete system were conducted at various angles of attack (AOA), at the take-off condition. Unsteady results were time and circumferentially averaged in a manner that allows for fan-distortion interaction and distortion transfer through the stage to be more easily understood from contour plots of various flow quantities.

1.2. THESIS ORGANIZATION

The thesis is composed of four main components. In the rest of this chapter, literature presenting numerical and experimental studies of NASA rotor 67 [3] and stage 67 [2] is

summarized. Chapter 2 details the geometric model of the engine fan system including the physical geometries, the computational configurations, and the grids used for CFD simulations. Chapter 3 presents a brief overview of the Reynolds/Favre-Averaged Navier-Stokes modeling and the turbulence models used to achieve closure for the system. Furthermore, the main elements of the finite-volume method (FVM) solver employed for all of the CFD simulations in this work are reviewed and the test cases, computational resources, and costs for these simulations are documented. In addition, the methods for post-processing the simulation data are prescribed. Chapter 4 presents the results and provides an in-depth discussion on the findings. Finally, conclusions are drawn and future work is proposed in Chapter 5.

1.3. LITERATURE REVIEW

Flows for the Rotor 67 (R67) geometry have been extensively investigated computationally and experimentally since 1984; consequently, a rich body of literature data exists for comparison and validation of the findings in the present work. Experimental measurements of flow within R67 were first taken in 1984 by Strazisar *et al.* [4] with specific emphasis on data collection for use in CFD validation. Additional data and analysis for both the rotor alone and for the rotor with an accompanying stator (of different geometry than that studied in this work) were presented in literature [5] [6] [7]. The wealth of experimental data, including detailed laser anemometry measurements at various spanwise locations and rake data, made R67 an excellent candidate for CFD validation studies. In the years since, numerous CFD predictions have been published.

Three-dimensional inviscid simulations of R67 (a single passage) at 100% of the design speed and with clean inlet flow were completed by Pierzga in 1984 using Denton's turbomachinery CFD code [8]. The code was modified to include boundary layer displacement effects by use of mass injection. Fair agreement with experimental data was obtained for the fan's performance, and the choked mass flow rate was accurately predicted. However, the complex shock structure was not well predicted, most likely due in part to the small mesh size. The mesh had a total of 0.2 million cells with only 11 cells in the radial direction and no tip clearance. In 1991, Chima [1] performed viscous three-dimensional calculations of transonic fan performance, possibly the first viscous 3D simulation of R67, for the rotor alone operating at 100% of the design speed with clean inflow. The solver used a node-centered second-order finite-difference method. An explicit multi-stage Runge-Kutta scheme with implicit residual smoothing was used. The modified Baldwin-Lomax turbulence model was adopted. The mesh topology was C-type and the grid size consisted of approximately 0.36 million cells, without tip clearance. The CFD predictions agreed well with the experimental data on the performance map. Radial profiles of stagnation quantities were predicted accurately, while static pressure and flow angle showed some disagreement with experimental data. Location and strength of shocks were predicted accurately near peak efficiency, but overpredicted near stall. Wake profiles of CFD solutions were much deeper than those reported from the experiment, but location and spreading were in reasonable agreement. Contours of relative Mach number at 30% span (from the shroud) for an operating condition near stall, as plotted by Chima [1], are shown in Figure 1.1. This figure demonstrates the extent to which this early CFD work predicted the flow within the rotor. The convention for spanwise location used by Chima is consistent with that used by Strazisar *et al.* [4], and has been adopted in this

thesis. By this convention, the shroud surface is defined as being at 0% span and the hub surface is defined as being at 100% span.

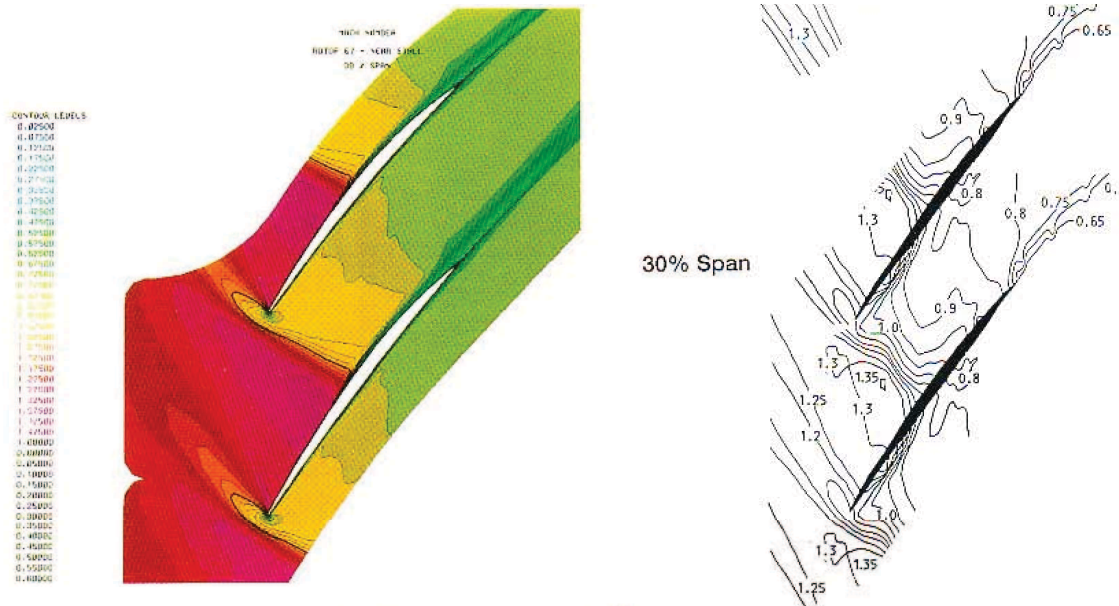


FIGURE 1.1. Contours of relative Mach number, near peak efficiency. The heavy line is at $M = 1.0$ with contour increments of 0.05. [1]

Hah and Reid [9] studied the viscous flow in R67 with a focus on understanding shock-boundary layer interaction, radial transport, and wake development in the transonic compressor. Their results were published in 1992. The CFD solver employed an implicit relaxation method with a fully conservative control volume approach. The method was of second-order accuracy with smoothly varying grids. A two-equation turbulence model, modified to include low-Reynolds number effects, was used. The same operating conditions as those used by China [1] were investigated. The mesh had approximately 0.25 million cells, and there were 6 cells in the radial direction within the tip clearance region. Overall predictions of the performance and the shock structure matched experimental data well. Strong tip clearance flow near the leading edge, as well as strong interaction between the tip-leakage vortex and

passage shock were observed. For the span locations less than 40% (from shroud), separation was found to be induced by shock-wave boundary layer interaction. For the span locations greater than 40%, adverse pressure gradients caused separation. In 1993, Jennions and Turner [10] simulated flow in R67, under the same conditions as previous studies, as part of a validation of a three-dimensional Navier-Stokes code. An explicit flow solver and an implicit k - ϵ solver were used. The grid consisted of approximately 0.33 million cells. Three individual computations were done, with differing tip clearances. Predictions of performance and radial profiles of stagnation quantities agreed well with experimental data, as did contours of relative Mach number at various spanwise locations. The complex interaction between the leading edge shock and the tip vortex was highlighted. A finite-volume solver, in which a full multigrid method was employed, was used by Arnone [11] in 1994, to simulate R67 under the same condition as Chima [1]. The results were consistent with those described by Chima [1], Hah and Reid [9], and by Jennions and Turner [10]. In 1997, Arima conducted a numerical investigation of flow within R67, using a low-Reynolds number k - ϵ turbulence model [12], and predicted static pressure closer to experimental than previous simulations for the same operating conditions. Also, low static pressure at around 60% span was predicted, which was consistent with experiment but not captured by previous simulations. Information on the CFD solver was not obtained, but the mesh was approximately 0.76 million cells with 10 cells in the tip clearance region.

Grosvenor [13] [14] reported the single passage, rotor-alone, steady-state simulations focusing on near-stall conditions and shock-wake boundary layer interaction (SWBLI) using FINE/Turbo of Numeca, a density-based compressible RANS FVM solver with added artificial dissipation. The results were published in 2007 and 2008. The Spalart-Allmaras

turbulence model was chosen due to its accurate predictions of such phenomena as boundary layer development, separation in diffusing flows, turbomachinery flows, and shock wave boundary-layer interaction; while being computationally efficient, robust, and having minimal grid resolution requirements. Uniform inflow and 100% speed (i.e. 100% of the design speed) were considered. The meshes used were of O-H topology. Coarse, medium, and fine meshes were composed of 0.24, 1.2, 9.0 million cells, respectively. The coarse and medium meshes had $1 < y^+ < 5$ and the fine mesh had $0.1 < y^+ < 0.5$. The tip clearance was about 0.5 mm with approximately 9–33 cells. The findings were in good agreement with experimental data. The fan performance calculated from rake integration differed from that calculated using slice integration. Rake values were calculated by integration, at each station, of only the discrete radial locations at which probes were located in the experiment. Slice values were calculated by integrating the entire CFD solution at the stations. Fine grids converged at lower mass flow rates than did the coarse grid. Grosvenor estimated that the medium grid was needed to resolve off-design conditions sufficiently [13]. Removing tip clearance resulted in significantly overestimated performance. In 2015, Grosvenor et al. [15] focused on a high resolution RANS nonlinear harmonic study of stage 67 tip injection physics using the same solver and turbulence model. The computational domain included components which matched an experimental rig for which test results have not been separately published. Three grids, 2.34, 18.6 and 148.0 million cells per passage, were created with 8, 16, and 32 cells in the tip clearance region, respectively. The meshes were characterized by an O-H topology. A high concentration of cells was used near the shroud. The operating conditions were uniform flow at 90% speed. It was found that the low velocity region near the shroud, at near-stall conditions, was reduced by tip injection. Injection decreased the shape factor (defined as the

ratio of the boundary layer's displacement thickness to momentum thickness) upstream of the passage shock, and shifted the tip clearance vortex downstream. As the stall condition was approached, the passage shock (normal shock) moved forward until it was in front of the blades. The distorted flow from the tip clearance vortex became less stable as it passed through the passage shock.

Fidalgo *et al.* [2] investigated the full-annulus, unsteady, three-dimensional CFD simulations of stage 67 with circumferential inlet distortion. The results of this study were published in 2012. The solver was Rolls-Royce's HYDRA, an unsteady, compressible, RANS, unstructured FVM solver with a Roe upwind scheme and dual time stepping. The Spalart-Allmaras turbulence model was employed. Adamczyk's method [16] was used to calculate time-averaged solutions without blades. The mesh statistics included an O-H topology, approximately 1.2 million cells per rotor passage, and 42 million cells in total. The study emphasized that "all the rig geometrical details, such as the rotor's 1.78-mm-radius hub fillet, were included in the grids." The size of the tip clearance was not specified and a grid independence study was not presented. The computational configuration reproduced an experimental rig in which screens were used to create a total pressure distortion upstream of the fan. The operating condition under investigation was 90% speed with an 11% deficit in total pressure over 120 degrees defined as a square wave in the circumferential direction. It is worth mentioning here that the same convention for the inlet condition specification shown in Figure 1.2 is adopted in this thesis. The CFD simulation data obtained by Fidalgo *et al.* [2] were in good agreement with the experimental results. It was observed that the fan interacted with the upstream flow, redistributing the mass flow. The local operating point of the rotor was affected not only by the incoming pressure but also by the induced

swirl caused by the mass flow redistribution. Total pressure was attenuated by the rotor, producing distortions in the stagnation temperature, flow angle, and static pressure which affected the flow in the outlet guide vane (OGV). Convection of static pressure and flow angle was suppressed in the OGV but convection of stagnation quantities were not. The trends can be seen in contours of these quantities near the shroud, as plotted by Fidalgo *et al.*, in Figure 1.3. The figure illustrates the effects of induced swirl, defined as co-swirl and counter-swirl. Co-swirl is defined as swirl in the same direction of the fan rotation, while counter-swirl is in the opposite direction.

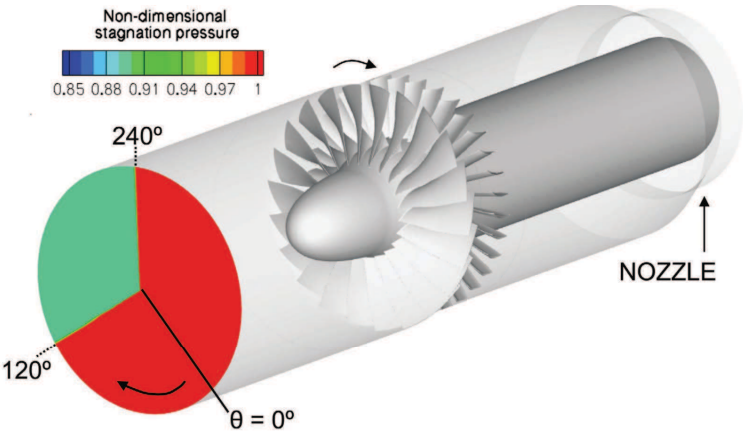


FIGURE 1.2. Isometric view of the computational domain. [2]

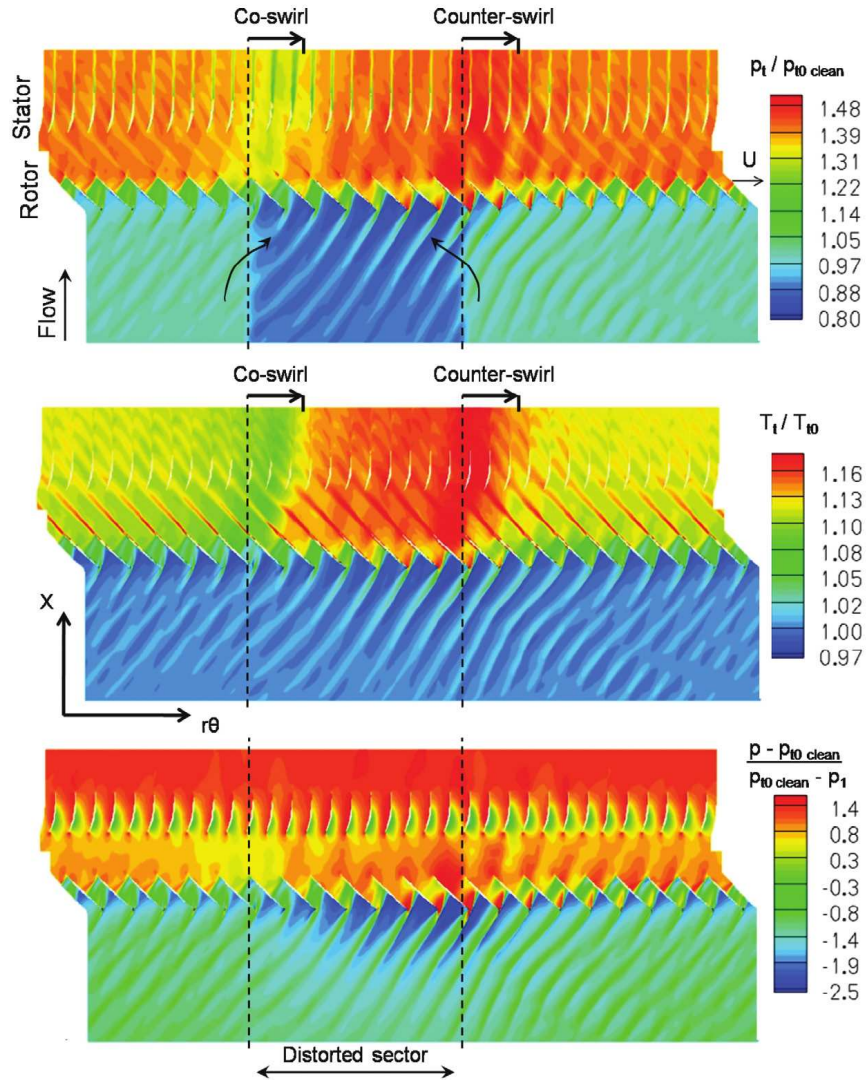


FIGURE 1.3. Unwrapped blade-to-blade snapshot at 90% span of stagnation pressure and temperature and static pressure. [2]

Simulations of R67 have also been conducted within the context of both optimization [17] [18] [19] [20] and stall inception [21] [22] research. The literature is not reviewed here, but interested readers may refer to the above references for details.

This thesis work contributes to the body of literature a benchmark case for URANS simulations of a complete engine fan system; including rotor, stator, nacelle and nozzle; with inlet distortion representative of that encountered by modern aero-engines of commercial aircraft.

CHAPTER 2

GEOMETRIC MODELING OF THE ENGINE FAN SYSTEM

2.1. PHYSICAL COMPONENT GEOMETRIES AND CONFIGURATIONS

The geometry chosen for this study is the NASA rotor 67 transonic fan stage, which is referred to herein as stage 67. The stage is comprised of a low aspect ratio rotor and a controlled-diffusion stator row [2]. The rotor has 22, multiple-circular-arc blades and is the first stage rotor of a two stage fan designed at NASA Lewis [23]. Descriptions of the rotor geometry are available in numerous references [24] [23] [3] [5] [6] [7]. For convenience, characteristic parameters of the rotor design are listed in Table 2.1. Unfortunately, specifics regarding the design of the 34 stator blades, which are of a different design than those presented in the aforementioned references, are not available. However, the stator geometry used in this thesis was obtained from NASA in Plot3D format.

TABLE 2.1. Characteristic parameters for the rotor-alone operating at 100% of design speed

Number of blades	22	Inlet tip relative Mach number	1.38
Rotation speed	16043 rpm	Rotor aspect ratio	1.56
Mass flow	33.25 kg/s	Rotor solidity at hub	3.11
Pressure ratio	1.63	Rotor solidity at tip	1.29
Isentropic efficiency	0.92	Tip diameter at inlet	51.4 cm
Rotor tip speed	429 m/s	Tip diameter at exit	48.5 cm
Tip clearance	1.006 mm	Mean hub/tip radius ratio	0.375

2.2. COMPUTATIONAL MODEL OF THE ENGINE FAN SYSTEM

2.2.1. MODEL GEOMETRY. In this work, we define the engine fan system to be all components which influence the flow within the turbomachine stage. This includes the rotor, hub, and shroud; as well the stator row, nacelle, nozzle and center-body, when present.

Discrete geometry defining both rotor and stator blade sections was received from NASA in Plot3D format. Flow path geometry for annular and spinner geometries was also received from NASA. Coordinates of blade sections were extracted from the Plot3D format and imported to SolidWorks as curves. Figure 2.1 illustrates representative blade sections of the rotor and stator at three spanwise locations; with the hub shown in black, midspan in blue, and shroud in red.

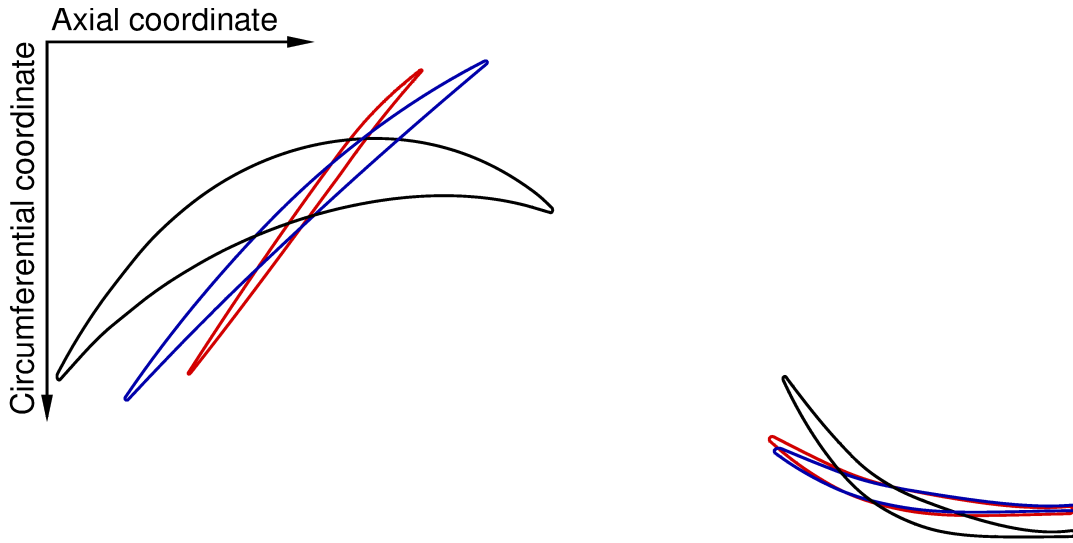


FIGURE 2.1. Representative blade sections of the rotor (left) and stator (right) at three spanwise locations: hub (black), midspan (blue) and shroud (red).

A NURBS surface was lofted through the section curves to define the blade surfaces. Coordinates for the flow path geometries (i.e. the strictly annular flow path and that including a spinning center-body) were imported into SolidWorks as curves and revolved to define hub and shroud surfaces. A rolling ball fillet with a radius of 1.78 mm was created at the interface of the blade with the hub. Constant diameter duct sections were added upstream and downstream so that the inlet and outlet boundaries were a greater distance from the rotor than was defined by the flow path coordinates received. The nacelle geometry was created with the help of subject matter experts from an aircraft manufacturer. The converging

nozzle geometry was designed by the author. Figures 2.2 - 2.3 show the multiple nozzles geometries which were designed to allow for control of the mass flow rate.

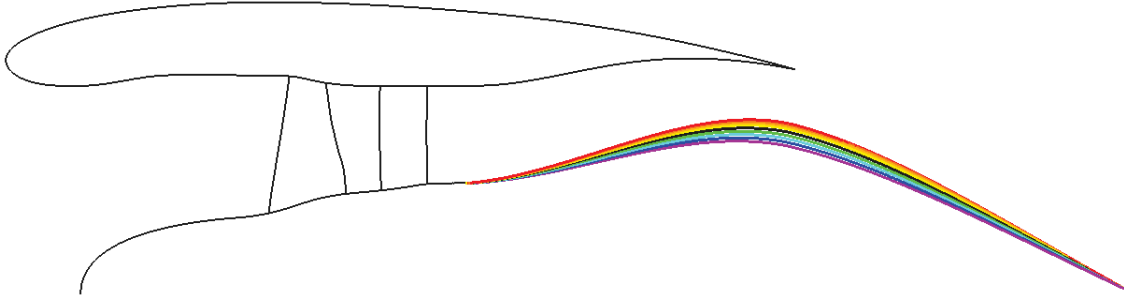


FIGURE 2.2. Multiple nozzle sizes used for single-passage calculations of stage performance with nacelle and nozzle at various operating conditions.

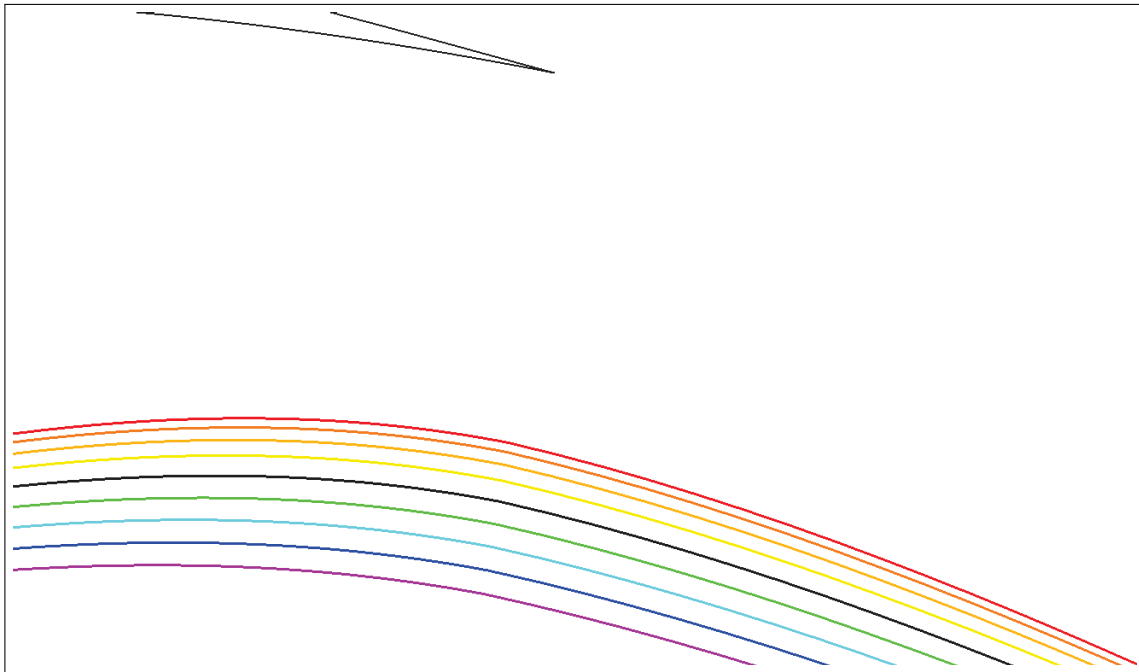


FIGURE 2.3. Detail of multiple nozzle sizes used for single-passage calculations of stage performance with nacelle and nozzle at various operating conditions.

Assemblies were created from the components described above. There are four geometric configurations, as shown in Figure 2.4. Specifically, the geometric configurations are as follows: the rotor-alone with an annular flow path (used in [3]) denoted by (a), the rotor

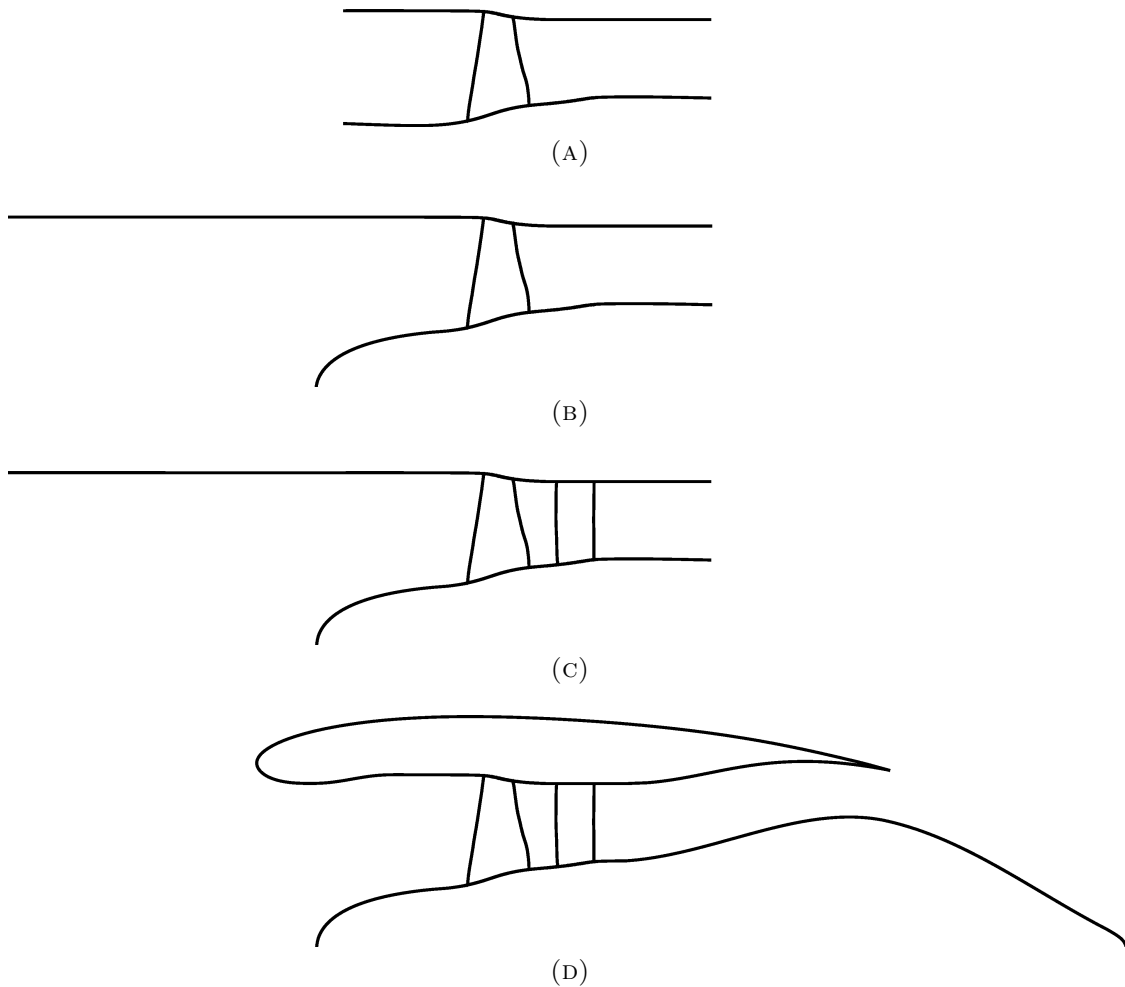


FIGURE 2.4. Geometric configurations shown in the meridional plane. (a) rotor-alone with annular flow path, (b) rotor alone with center-body, (c) stage, and (d) stage with nacelle and nozzle.

alone with a spinning center-body (as used for data recorded in 2004 and reported in [2] and [13]) denoted by (b), the complete stage with spinning center-body denoted by (c), and the complete stage with spinning center-body, nacelle, and nozzle denoted by (d). The tip clearance used in all simulations was 1.006 mm, a measurement specified in the primary reference [3]. It is notable, however, that other authors have posited that the correct tip clearance for the rotor is actually closer to 0.5 mm [13].

2.2.2. COMPUTATIONAL GRIDS. Structured grids were used exclusively, with the exception of the off-body mesh extending to the farfield domain, for the geometry inclusive of nacelle and nozzle. Structured grids were chosen as they require fewer cells for a given node count. Additionally, structured grids in turbomachinery often have cell faces implicitly aligned with the flow, reducing discretization errors in the solver. All meshes were generated with the commercial software Pointwise [25].

Particular attention was paid to near-body cell quality, to minimize error in the resolution of boundary layers. Multi-block topologies were used to allow for highly orthogonal grids despite the complex geometry. All geometric features were accurately reproduced in the grids, including the rotor's geometric features of a tip clearance gap and 1.78 mm fillet at the interface of the hub and blade.

A series of grids, of widely varying cell counts, were generated to assess the dependence of solutions upon grid resolution. Figure 2.5 shows the series of rotor grids near the mid-span as contiguous passages.

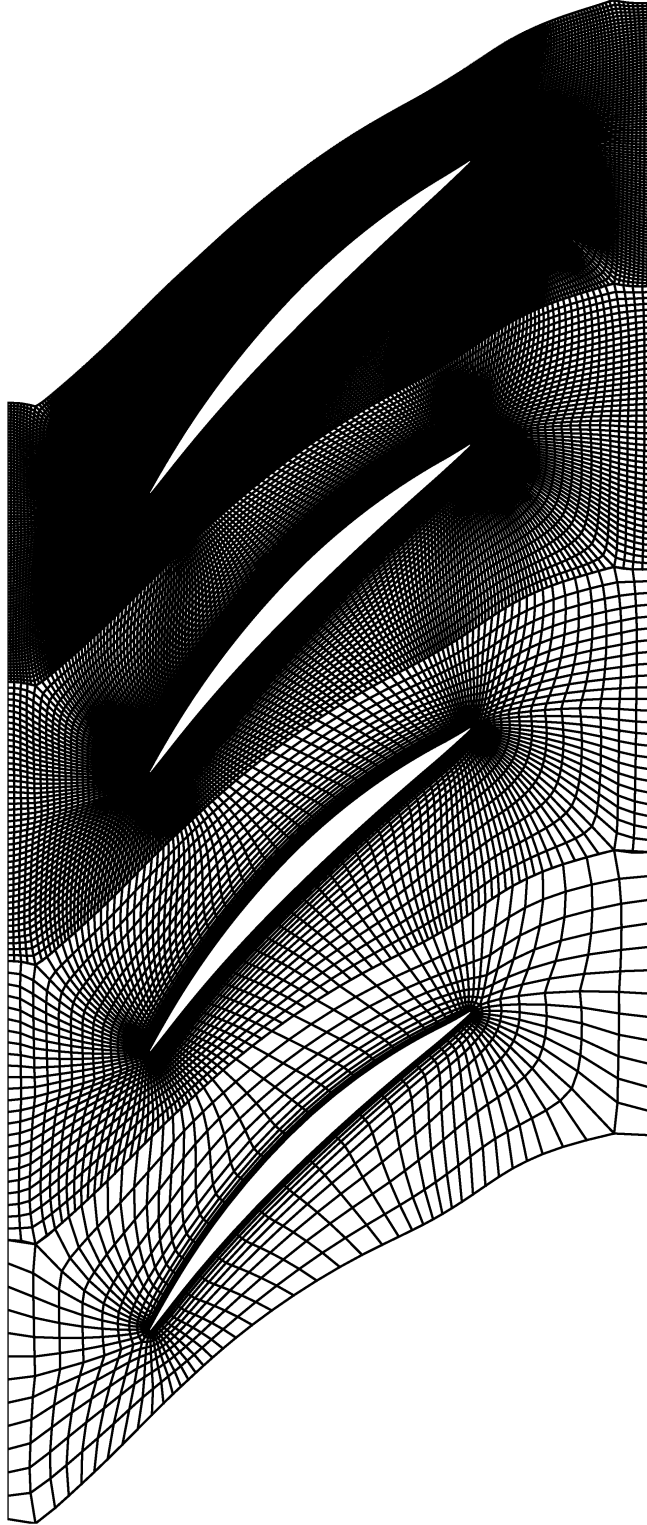


FIGURE 2.5. Series of grids created by uniform coarsening, shown near the midspan as contiguous passages from fine (top) to extra coarse (bottom).

To generate such a series of grids, the finest grid in each series was constructed with Pointwise, output to Plot3D format and uniformly coarsened using a utility within CFD++ by Metacomp Technologies [26]. Grids were coarsened successively to obtain grids with the desired cell counts. Two grid series were completed: a series of 4 grids with wall spacings suitable for the application of wall-functions within the solver and a series of 3 grids with wall spacings suitable for direct integration through the boundary layer to the wall with turbulence being modeled by low-Reynolds number formulations. Grids for use with wall-functions were designed with wall spacings which were expected to place the first cell centroid within the log-region of the boundary layer with corresponding y^+ values of between approximately 20 and 200. Wall spacing for grids designed for integration to the wall were chosen such that resultant first y^+ values were strictly less than 1. Due to the uniform coarsening, stretching ratios for fine grids were small compared to the coarsened grids. Stretching ratios of 1.05 were used for the finest grids, therefore, twice coarsened grids had stretching ratios approaching 1.25 and thrice coarsened grids had stretching ratios of approximately 1.5. The two series of grids are identical in the regions defined by the J topology, with the differences in wall spacing realized within the O-mesh regions. The regions of mesh within the O-grid (surrounding the rotor blade) are referred to as the near-body grids, while the cells within the J-mesh regions are referred to as the off-body grids. Each grid designed for integration to the wall shares an off-body mesh with one of the grids designed for use with wall-functions. Therefore, three pairs of grids may be noted, as seen in Table 2.2. The order of magnitude of the grid cell count is equal for members of any given grid pair.

TABLE 2.2. Pairs of grids with identical cells in J topology regions

Pair	Grid 1	Grid 2
A	2.3×10^5 cells with $60 < y_1^+ < 120$	4.3×10^5 cells with $y_1^+ < 1$
B	1.9×10^6 cells with $30 < y_1^+ < 60$	3.5×10^6 cells with $y_1^+ < 1$
C	1.5×10^7 cells with $15 < y_1^+ < 30$	2.8×10^7 cells with $y_1^+ < 1$

Grids were generated for a single, periodic passage of each the rotor and stator. The periodic boundaries were point-matched to avoid both the need for interpolation at these boundaries and the use of the resources required by such interpolation. The grid quality metrics observed most closely were equiangle skewness and stretching ratios. Equiangle skewness was kept strictly below 0.87 and stretching ratios for grids used in URANS simulations were approximately 1.22.

2.2.2.1. *Rotor Alone Grids.* An O-J topology was chosen for the rotor in order to minimize the cell count of the grids, minimize aspect ratios away from wall boundaries, and maximize cell orthogonality. The goal of the research was to perform URANS simulations with sliding boundaries, therefore, the circumferential spacing at the inlet and exit boundaries of the rotor grid was made uniform to reduce interpolation error at these boundaries by allowing for the interpolation cells to be closely matched in volume and node location. Figure 2.6 shows the O-J topology rotor grid used for URANS simulations. The O-J topology is named as such because of the O-mesh which wraps completely around the blade, and the J-mesh which surrounds it and is composed of two blocks.

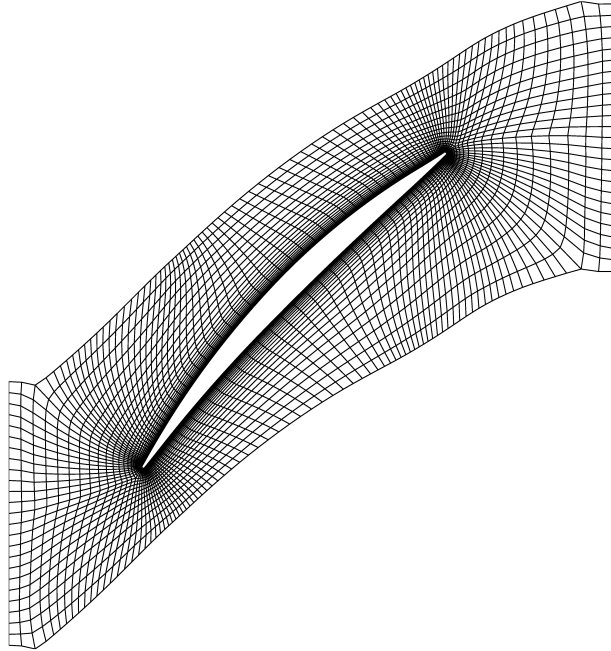


FIGURE 2.6. Coarse rotor grid used for URANS calculations, shown near the midspan.

The topology of the rotor zone mesh is not such that the rotor wake may be well resolved with clustering of the grid cells, as would be the case for O-H or O-C topologies. However, wake resolution with higher aspect ratio cells in regions of strong wake gradients, as could be accomplished with O-H or O-C topologies, would result in interpolation errors at the sliding boundary between the rotor and stator due to disparate cell sizes. Increased resolution of the wake could not be maintained across the moving boundary because the wake location is not fixed with respect to stationary zones. The tip clearance region was fully meshed, with an O-H topology ("butterfly" mesh). The grid in the vicinity of the rotor's tip, near the leading edge, is shown in Figure 2.7, with the surface grid of the rotor shaded. The fillet was meshed with a complex topology, as shown in Figure 2.8, where a slice through the fillet grid, in the direction normal to the blade surface is shown in blue. The surface mesh for the

rotor-alone grid is shown in Figure 2.9 and Figure 2.10 shows the periodic boundary of the coarse rotor grid on the meridional plane.

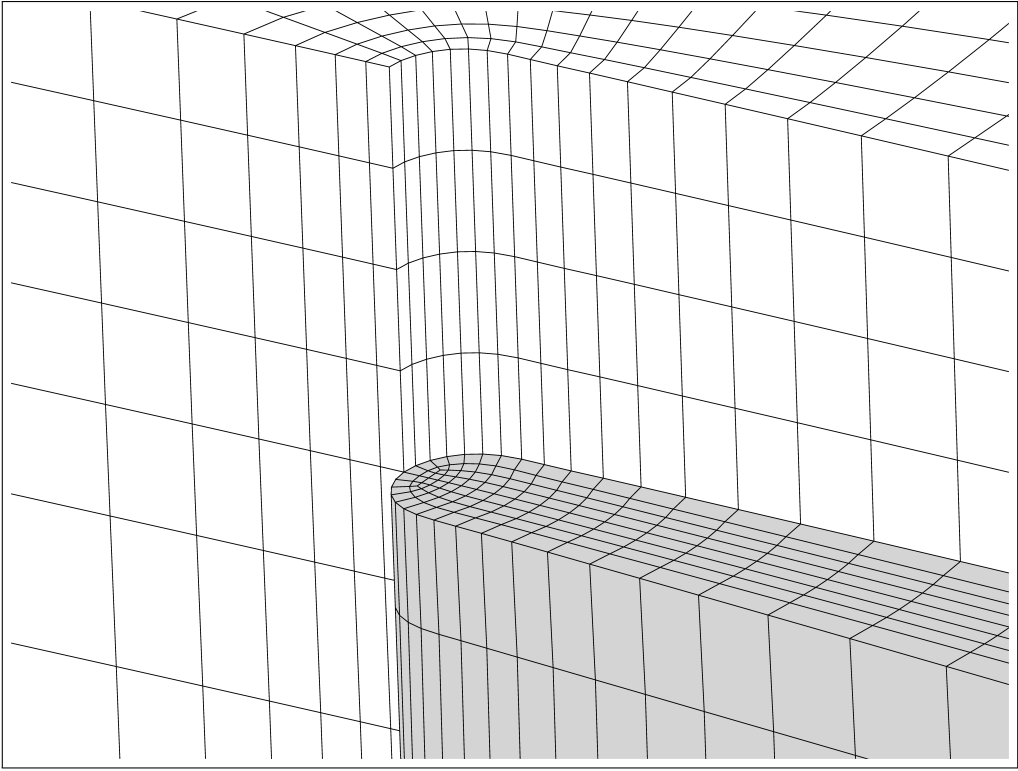


FIGURE 2.7. Grid in the tip clearance region at the leading edge of the rotor.

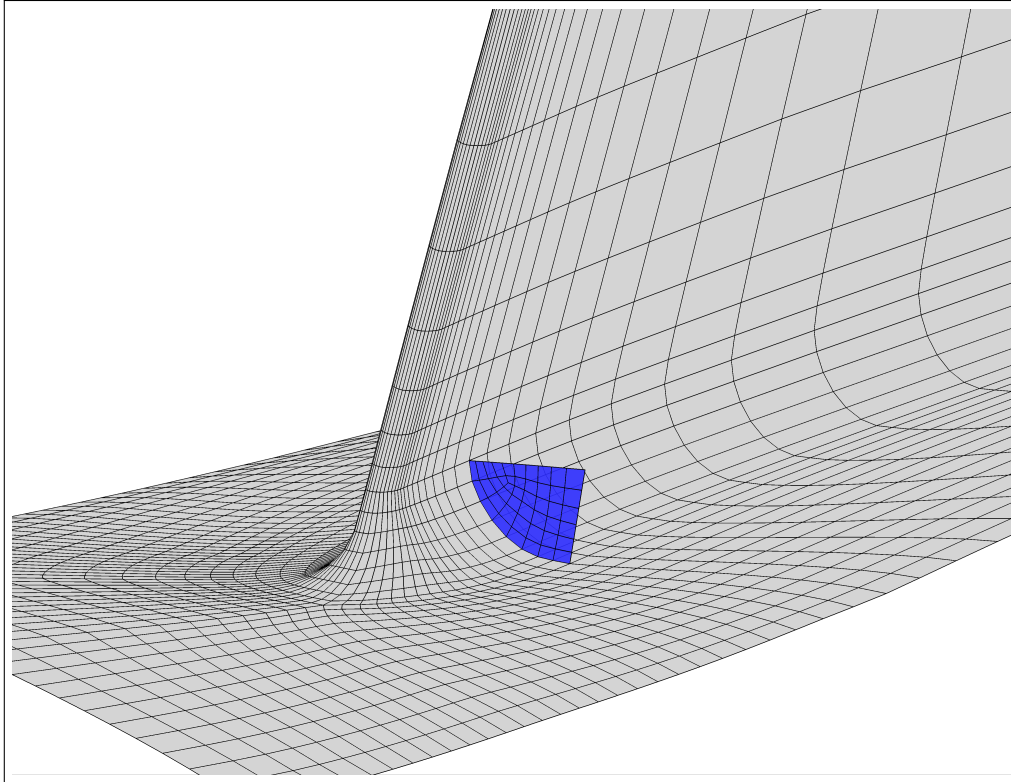


FIGURE 2.8. Grid topology in rotor fillet region.

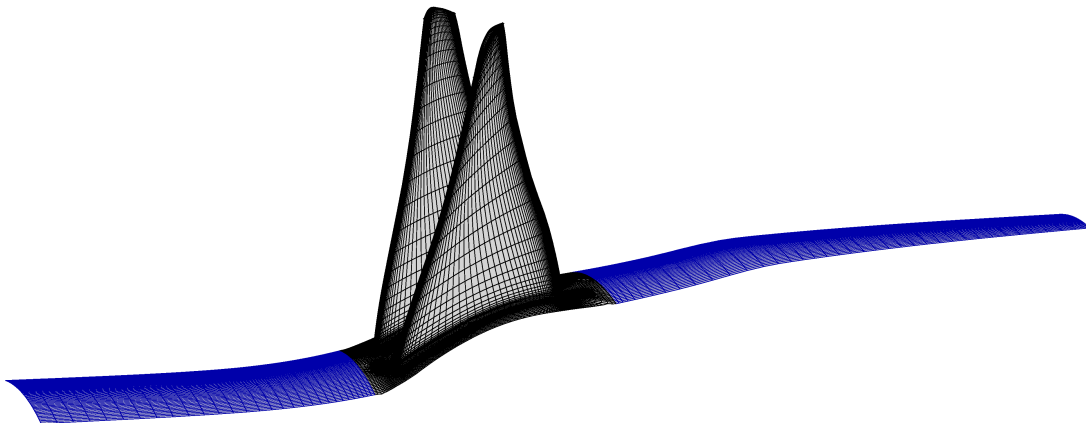


FIGURE 2.9. Surface grids for rotor-alone grid (coarse). The moving surfaces are shown in black and the stationary surfaces are shown in blue. Two passages are shown.

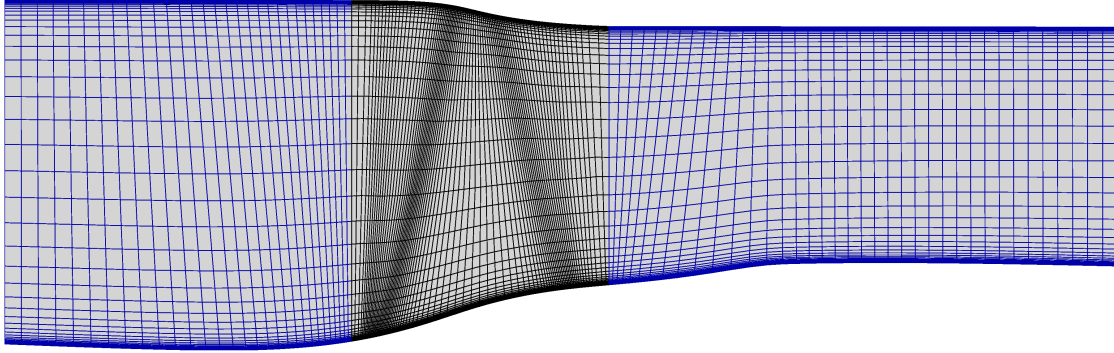


FIGURE 2.10. Periodic boundary of rotor grid (coarse) shown on the meridional plane with core rotor zone shown in black and inlet and outlet extension block shown in blue.

2.2.2.2. *Stage with Center-body Grids.* The stage with center-body was meshed separately for single-passage simulations and for full-annulus simulations. Both grids include the coarse rotor grid described previously. In addition, a grid of C topology, with an O-grid around the blade surface of the stator, was generated. Coarse grids for the rotor and stator are shown in Figure 2.11. The grid on the periodic boundary of the entire single-passage coarse grid for the stage with center-body geometry is shown on the meridional plane in Figure 2.12.

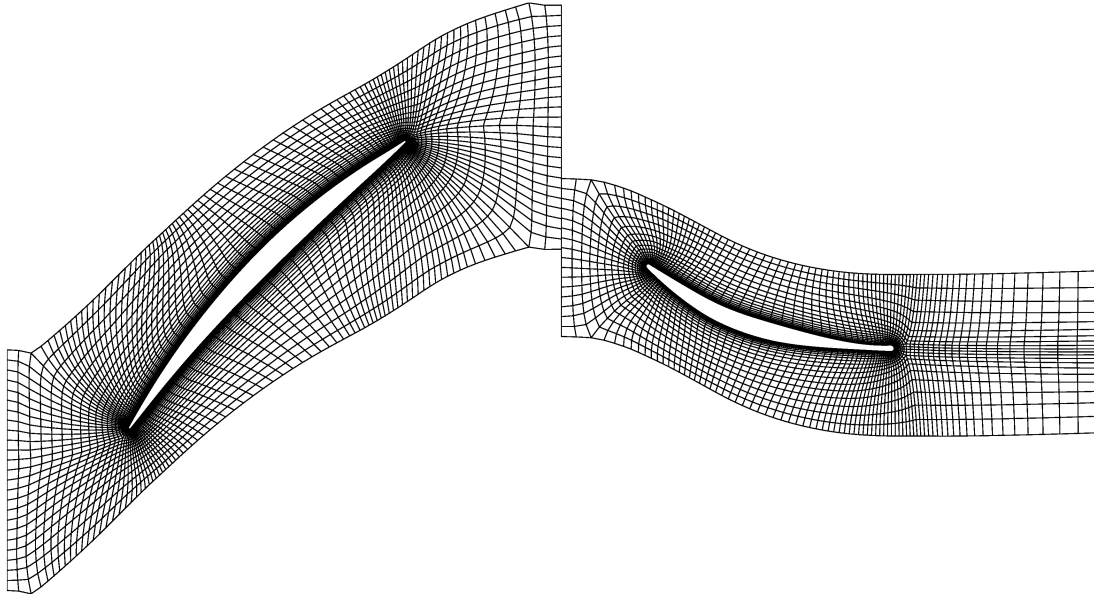


FIGURE 2.11. Rotor and stator grids (coarse) shown near the midspan.

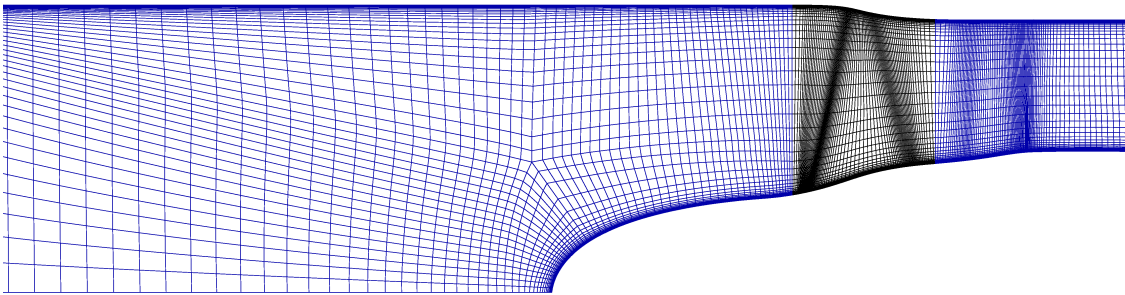


FIGURE 2.12. Periodic boundary of coarse grid for the stage with center-body, shown on the meridional plane with rotor zone in black.

For the full-annulus grid, both single-passage rotor and stator grids were replicated and rotationally transformed as needed to complete the 360 degree mesh. Mesh sections upstream and downstream of the blade grids were generated to complete the domain. For both instances, the upstream mesh included a block hyperbolically grown from the spinner surface mesh. This block was joined to an H-mesh, creating a quarter O-H mesh topology. The downstream blocks are simple H-topology grids. Upstream and downstream grids match the radial spacing of the contiguous blade sections. An isometric view of the entire grid for this

configuration is shown in Figure 2.13 and surface grids (excluding the shroud) are shown in Figure 2.14. The surface grid at the shroud, in the area of the stage, is unwrapped and illustrated in Figure 2.15.



FIGURE 2.13. Isometric view of full-annulus grid used for URANS simulations with circumferential distortion.

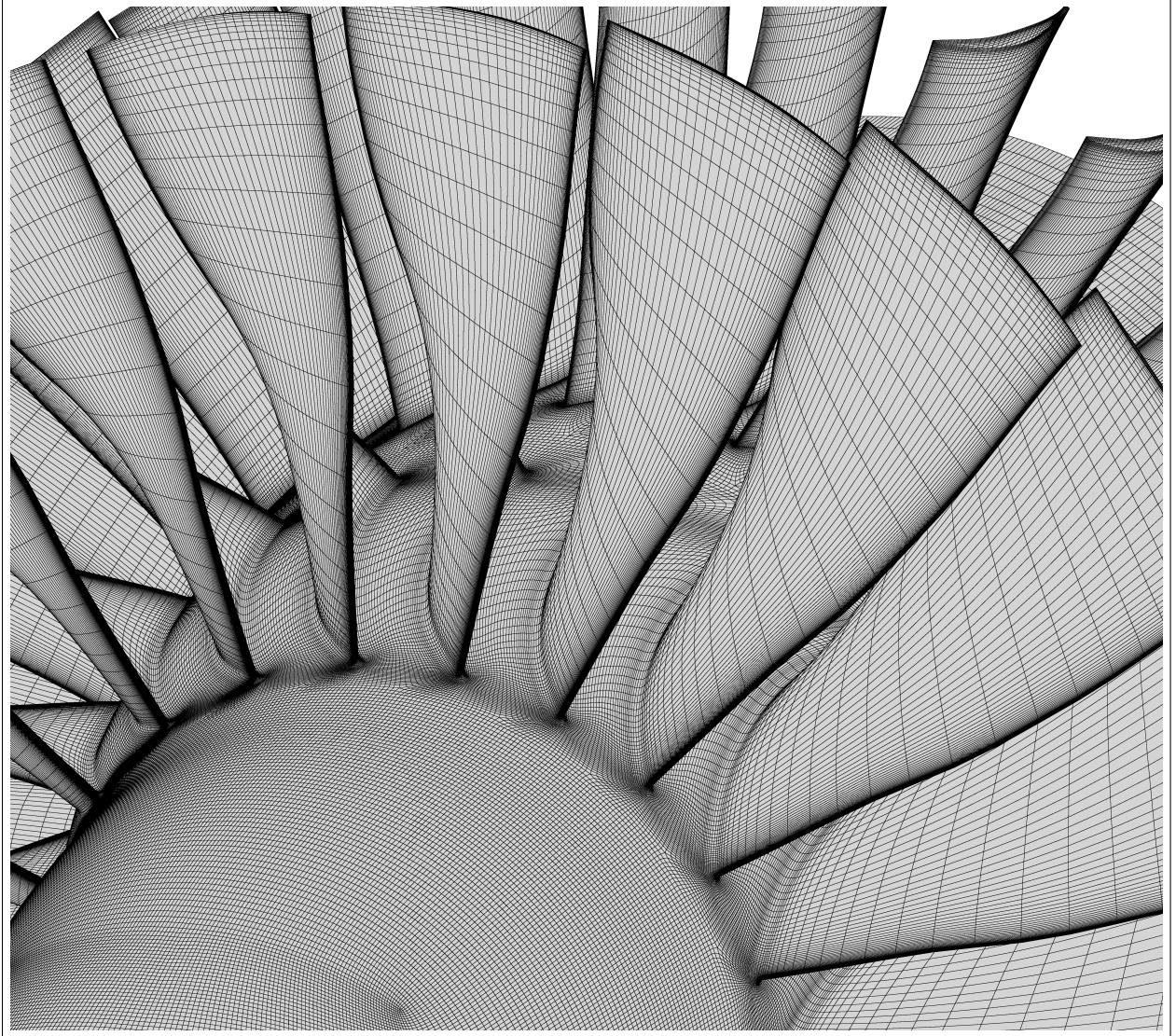


FIGURE 2.14. Surface mesh (excluding mesh at shroud) of full-annulus grid used for URANS simulations with circumferential distortion.

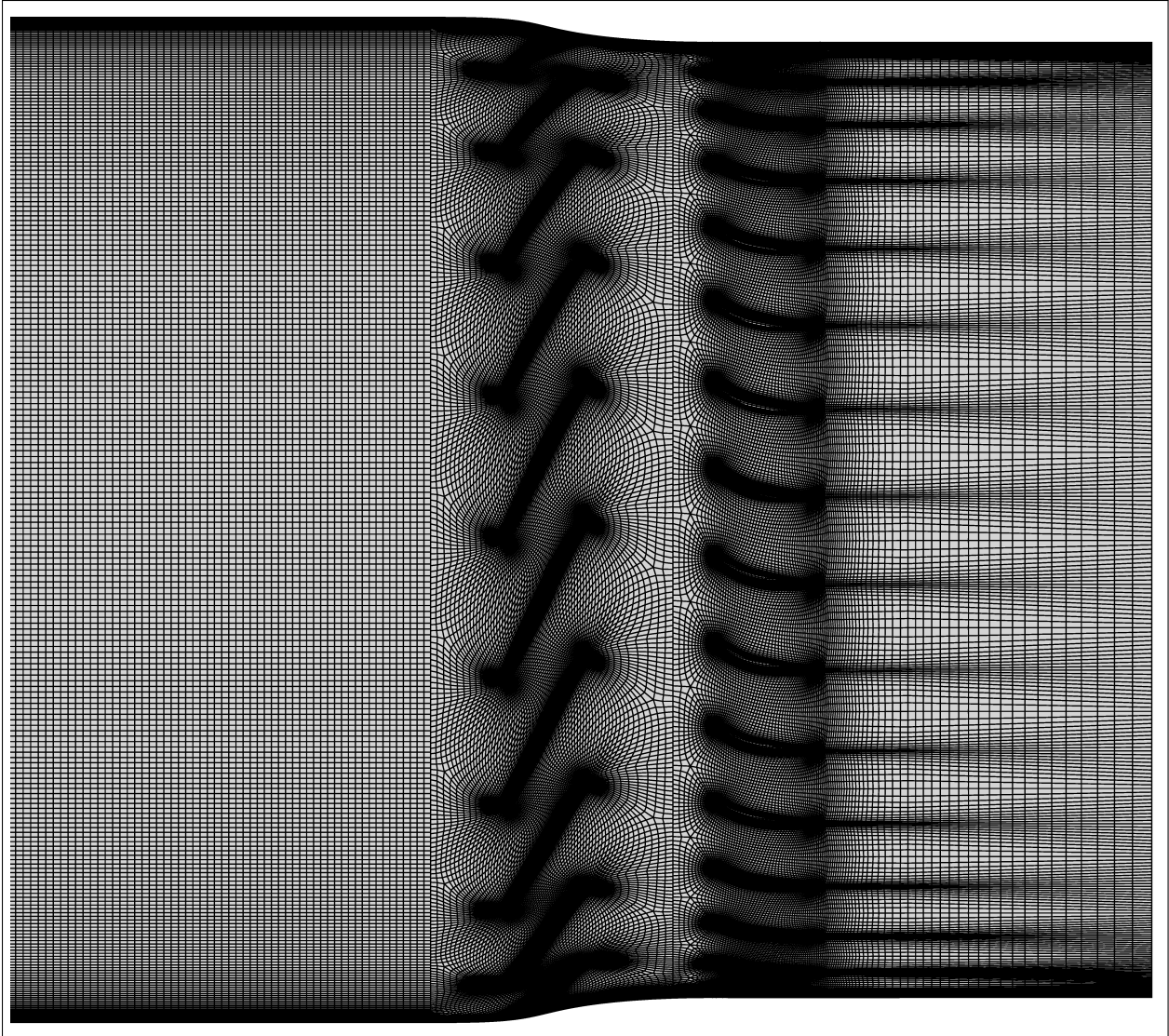


FIGURE 2.15. Surface mesh at the shroud of full-annulus grid used for URANS simulations with circumferential distortion.

2.2.2.3. *Stage with Nacelle and Nozzle Grids.* The grid for the stage with center-body, nacelle, and nozzle includes the rotor and stator grids used for the stage with center-body. Upstream and downstream grids were replaced in order to accommodate the change in geometry. An O-mesh was once again grown from each body, so that highly orthogonal cells were present where boundary resolution was needed. As was done for the stage with center-body and no nacelle, both single-passage and full-annulus grids were generated. For the single passage grids, structured grids were used exclusively. In the same manner as the stage with center body grids, the axis of rotation was avoided to eliminate degenerate hex cells. Figure 2.16 shows the periodic boundary of the single-passage grids for the geometric configuration including the nacelle and nozzle; a close-up of the grid is shown in Figure 2.17. For the full-annulus grids, off-body grids around the nacelle are unstructured and begin at the leading edge of the nacelle lip and extend to the farfield. The farfield grid was extended to 50 rotor diameters in each direction, with a half sphere shape upstream abutting a cylindrical domain downstream. A 2D slice of the unstructured grid can be seen in Figure 4.46 in Chapter 4.

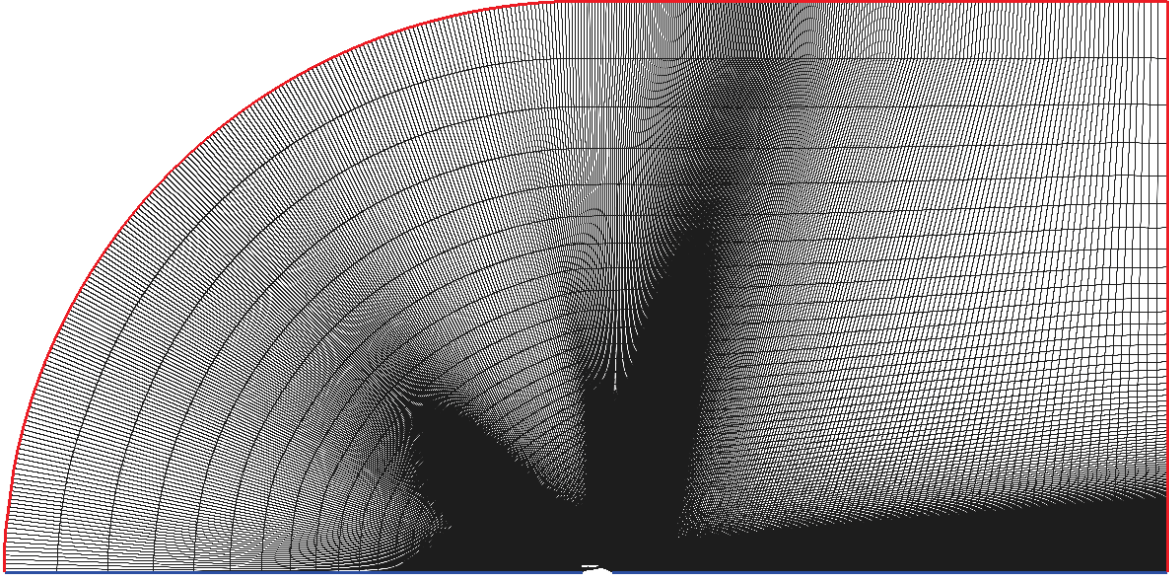


FIGURE 2.16. Periodic boundary of single-passage grids for geometric configurations including nacelle and nozzle, shown on the meridional plane.

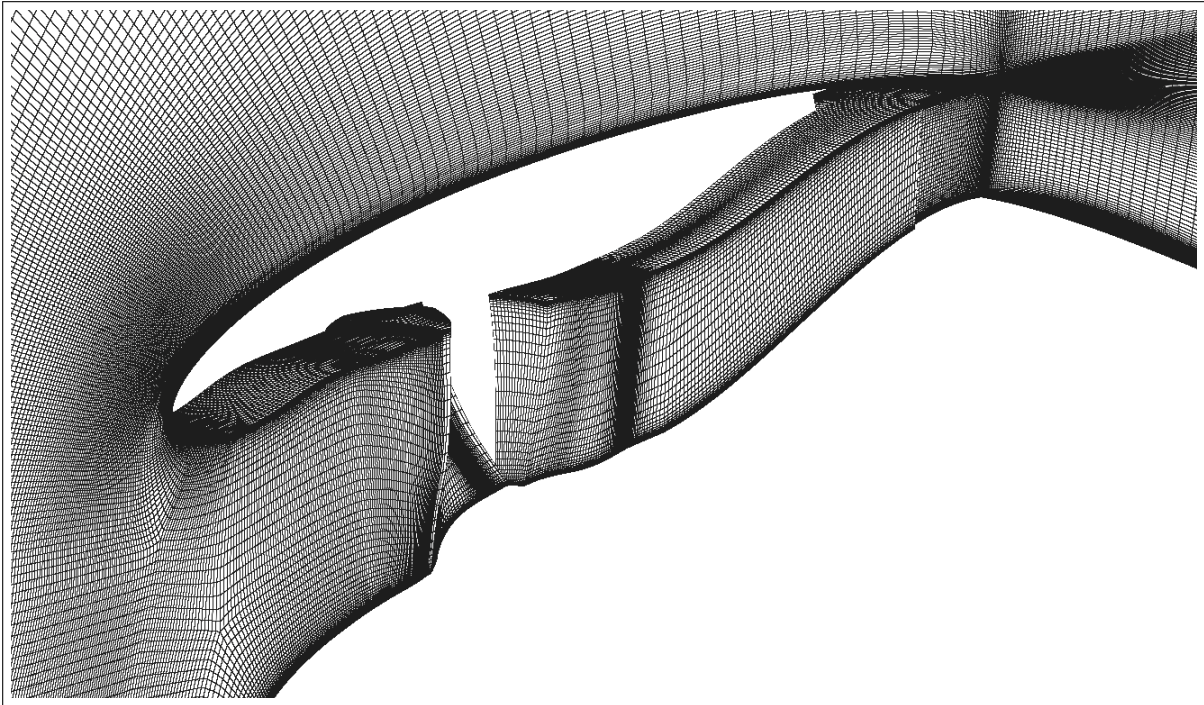


FIGURE 2.17. Single-passage grids for geometric configurations including nacelle and nozzle.

CHAPTER 3

URANS MODELING OF THE ENGINE FAN SYSTEM

In this chapter, we first introduce the concept of Favre averaging and present the Favre-averaged Navier-Stokes equations for a turbulent compressible fluid flow. Four turbulence models are considered for modeling the unresolved terms resulting from the Favre-averaging process and they are described in Section 3.4. The numerical methods of the CFD solver employed for this work are summarized in Section 3.5. The simulation cases are summarized in Section 3.6. In addition, the computational resources used for the simulations are described in Section 3.7. Finally, the post-processing methods used to extract and analyze useful data from the simulations are presented in Section 3.8.

3.1. COMPRESSIBLE NAVIER-STOKES EQUATIONS

For a compressible gas, the system of governing equations include the continuity, momentum, and energy equations. The particular form of these equations is consistent with that of Gao *et al.* [27] and given by

$$\frac{\partial \rho}{\partial t} + \vec{\nabla} \cdot (\rho \vec{u}) = 0 \quad (1)$$

$$\frac{\partial}{\partial t} (\rho \vec{u}) + \vec{\nabla} \cdot (\rho \vec{u} \vec{u} + p \vec{I}) = \vec{\nabla} \cdot \vec{\tau} + \rho \vec{f} \quad (2)$$

$$\frac{\partial}{\partial t} (\rho e) + \vec{\nabla} \cdot \left[\rho \vec{u} \left(e + \frac{p}{\rho} \right) \right] = \vec{\nabla} \cdot \left[\vec{\tau} \cdot \vec{u} \right] - \vec{\nabla} \cdot \vec{q} + \rho \vec{f} \cdot \vec{u} \quad (3)$$

where ρ is the density, t is time, \vec{u} is the velocity, p is the pressure, and \vec{I} is the identity tensor. Additionally, $e = |\vec{u}|^2/2 + h - p/\rho$ is the total specific energy with h being the enthalpy. Furthermore, μ is the molecular viscosity, $\vec{\tau}$ is the molecular stress tensor, \vec{f} is the body force, and \vec{q} is the molecular heat flux vector. The molecular fluid stress tensor, $\vec{\tau}$,

is defined as

$$\vec{\tau} = 2\mu(\vec{S} - \frac{1}{3}\vec{I}\vec{\nabla} \cdot \vec{u}), \quad (4)$$

where \vec{S} is the strain rate tensor defined by $\frac{1}{2}(\frac{\partial u_i}{\partial x_j} + \frac{\partial u_j}{\partial x_i})$. The equation of state for a thermally perfect gas is the ideal gas law, which is defined as

$$p = \rho RT, \quad (5)$$

where R is the specific gas constant. Equations (1–3) can conveniently be rewritten in the general divergence form, as

$$\frac{\partial \mathbf{U}}{\partial t} + \vec{\nabla} \cdot (\vec{\mathbf{F}} - \vec{\mathbf{G}}) = \mathbf{S}. \quad (6)$$

For implementation in numerical algorithms using the finite-volume method, the integral form of the governing equations is typically used and it takes the form

$$\frac{\partial}{\partial t} \int_{V_i} \mathbf{U} dV + \int_{V_i} \left(\vec{\nabla} \cdot (\vec{\mathbf{F}} - \vec{\mathbf{G}}) - \mathbf{S} \right) dV = 0. \quad (7)$$

The vector of the conserved solution variables for the three-dimensional case is given by $\mathbf{U} = [\rho, \rho u_x, \rho u_y, \rho u_z, \rho e]^T$. The inviscid and viscous flux dyads $\vec{\mathbf{F}}$ and $\vec{\mathbf{G}}$ are defined as

follows.

$$\vec{\mathbf{F}} = \begin{bmatrix} \begin{bmatrix} \rho u_x \\ \rho u_x^2 + p \\ \rho u_x u_y \\ \rho u_x u_z \\ (\rho e + p)u_x \end{bmatrix}, \begin{bmatrix} \rho u_y \\ \rho u_y u_x \\ \rho u_y^2 + p \\ \rho u_y u_z \\ (\rho e + p)u_y \end{bmatrix}, \begin{bmatrix} \rho u_z \\ \rho u_z u_x \\ \rho u_z u_y \\ \rho u_z^2 + p \\ (\rho e + p)u_z \end{bmatrix} \end{bmatrix}$$

$$\vec{\mathbf{G}} = \begin{bmatrix} [0, \tau_{xx}, \tau_{xy}, \tau_{xz}, u_x \tau_{xx} + u_y \tau_{xy} + u_z \tau_{xz} + \kappa \frac{\partial T}{\partial x}] \\ [0, \tau_{yx}, \tau_{yy}, \tau_{yz}, u_x \tau_{yx} + u_y \tau_{yy} + u_z \tau_{yz} + \kappa \frac{\partial T}{\partial y}] \\ [0, \tau_{zx}, \tau_{zy}, \tau_{zz}, u_x \tau_{zx} + u_y \tau_{zy} + u_z \tau_{zz} + \kappa \frac{\partial T}{\partial z}] \end{bmatrix}^T$$

The viscous stress tensor in 3D Cartesian coordinates is given by

$$\tau = \begin{bmatrix} \tau_{xx} & \tau_{yx} & \tau_{zx} \\ \tau_{xy} & \tau_{yy} & \tau_{zy} \\ \tau_{xz} & \tau_{yz} & \tau_{zz} \end{bmatrix}$$

$$= \begin{bmatrix} \frac{\mu}{3} \left(4 \frac{\partial u_x}{\partial x} - 2 \left(\frac{\partial u_y}{\partial y} + \frac{\partial u_z}{\partial z} \right) \right) & \mu \left(\frac{\partial u_x}{\partial y} + \frac{\partial u_y}{\partial x} \right) & \mu \left(\frac{\partial u_x}{\partial z} + \frac{\partial u_z}{\partial x} \right) \\ \mu \left(\frac{\partial u_y}{\partial x} + \frac{\partial u_x}{\partial y} \right) & \frac{\mu}{3} \left(4 \frac{\partial u_y}{\partial y} - 2 \left(\frac{\partial u_x}{\partial x} + \frac{\partial u_z}{\partial z} \right) \right) & \mu \left(\frac{\partial u_y}{\partial z} + \frac{\partial u_z}{\partial y} \right) \\ \mu \left(\frac{\partial u_z}{\partial x} + \frac{\partial u_x}{\partial z} \right) & \mu \left(\frac{\partial u_z}{\partial y} + \frac{\partial u_y}{\partial z} \right) & \frac{\mu}{3} \left(4 \frac{\partial u_z}{\partial z} - 2 \left(\frac{\partial u_x}{\partial x} + \frac{\partial u_y}{\partial y} \right) \right) \end{bmatrix}.$$

The source vector, \mathbf{S} contains terms related to the body force. It is defined as $\mathbf{S} =$

$$\left[0, \rho f_x, \rho f_y, \rho f_z, \rho \vec{f} \cdot \vec{u} \right].$$

3.2. AVERAGING CONCEPTS

Turbulent flows, such as those studied in this work, include random-like fluctuations of the flow properties. In theoretical and numerical methods attempting to predict these flows,

statistical approaches are typically used to account for these variations, yielding average values of the flow quantities. For incompressible flows, Reynolds averaging can be used to express flow quantities as the sum of fluctuating and constant components. It is important to note that Reynolds averaging of the conservation equations for incompressible flow introduces an additional term to the averaged conservation equations. This term, an averaged rate of momentum transfer due to turbulence, leaves the system of conservation equations unclosed unless additional equations are included in the system. While the Reynolds averaging method may also be applied to compressible flows, terms of increased complexity are introduced into the conservation equations, requiring complex correlations between the fluctuating flow properties to allow for closure of the system. This complexity is evidenced by the Reynolds-averaged continuity equation for compressible flow, given by

$$\frac{\partial \bar{\rho}}{\partial t} + \vec{\nabla} \cdot (\bar{\rho} \vec{u} + \overline{\rho' \vec{u}'}) = 0, \quad (8)$$

where $\overline{\rho' \vec{u}'}$ is the Reynolds-averaged correlation between fluctuations of density and velocity, ρ' and \vec{u}' , respectively. The term $\overline{\rho' \vec{u}'}$ does not appear in the original continuity equation and must be modeled. The application of Reynolds-averaging to the momentum equation for compressible flow introduces terms of even greater complexity, for which suitable closure approximations are correspondingly convoluted.

For this reason, the Favre averaging procedure is often used to derive ensemble-averaged conservation equations for compressible flow. Favre averaging eliminates density fluctuations from the averaged equations without removing their effect on the turbulence, a significant simplification when compared to the Reynolds averaging of the compressible Navier-Stokes equations. This simplification is a mathematical one, and does not simplify the physics

described by the equations. The Favre-averaged mean conservation equations for mass, momentum and energy are presented below. Although these equations are different from those derived by Reynolds-averaging, CFD methods which solve the Favre-averaged equations are commonly referred to as compressible Reynolds-averaged Navier-Stokes (RANS) methods, despite the semantic inaccuracy.

The Favre-averaging procedure and some notational conventions are now briefly reviewed to support an understanding of the Favre-averaged equations to be described in the next section.

The mass-averaged velocity vector, $\tilde{\vec{u}}$, is defined by

$$\tilde{\vec{u}} = \frac{1}{\bar{\rho}} \lim_{T \rightarrow \infty} \frac{1}{T} \int_t^{t+T} \rho(\vec{x}, \tau) \vec{u}(\vec{x}, \tau) d\tau, \quad (9)$$

where $\bar{\rho}$ is the conventional Reynolds-averaged density and $\vec{u} = \tilde{\vec{u}} + \vec{u}''$ with \vec{u}'' being the mass-weighted fluctuating velocity. Equation (9) can be expressed in terms of conventional Reynolds-averaging as

$$\bar{\rho} \tilde{\vec{u}} = \overline{\rho \vec{u}} = \bar{\rho} \bar{\vec{u}} + \overline{\rho' \vec{u}'}. \quad (10)$$

Substituting Equation (10) into Equation (8) one arrives at the Favre-averaged continuity equation given by

$$\frac{\partial \bar{\rho}}{\partial t} + \vec{\nabla} \cdot (\bar{\rho} \tilde{\vec{u}}) = 0, \quad (11)$$

which has a form identical to the laminar form of the equation. Throughout the rest of this thesis, the tilde symbol “ \sim ” will be dropped for mean (mass-averaged) quantities. Also, the bar symbol “ $-$ ”, will be dropped for convenience.

3.3. FAVRE-AVERAGED NAVIER-STOKES EQUATIONS

A representative mathematical model based on the Favre-averaged Navier-Stokes equations for compressible flows is presented below, since the exact formulation implemented within the CFD++ package used in this work is proprietary. The representative continuity, momentum, and energy equations for the compressible fluid flow are presented below for background information and to illustrate the need for turbulence modeling. The particular formulation below is consistent with that presented by Gao *et al.* [28].

$$\frac{\partial \rho}{\partial t} + \vec{\nabla} \cdot (\rho \vec{u}) = 0 \quad (12)$$

$$\frac{\partial}{\partial t}(\rho \vec{u}) + \vec{\nabla} \cdot (\rho \vec{u} \vec{u} + p \vec{I}) = \vec{\nabla} \cdot (\vec{\tau} + \vec{\lambda}) \quad (13)$$

$$\frac{\partial}{\partial t}(\rho e) + \vec{\nabla} \cdot \left[\rho \vec{u} \left(e + \frac{p}{\rho} \right) \right] = \vec{\nabla} \cdot \left[(\vec{\tau} + \vec{\lambda}) \cdot \vec{u} \right] + \vec{\nabla} \cdot (D_k \vec{\nabla} k) - \vec{\nabla} \cdot (\vec{q} + \vec{q}_t) \quad (14)$$

where ρ is the time-averaged density, \vec{u} is the Favre-averaged mean velocity, p is the time-averaged pressure, \vec{I} is the identity tensor, $e = |\vec{u}|^2/2 + h - p/\rho + k$ is the Favre-averaged total specific energy with h being the enthalpy, k is the specific turbulent kinetic energy, $k = \overline{u'' \cdot u''}$, and D_k is the coefficient for the diffusion of the turbulent energy ($D_k = \mu + \mu_t \sigma^*$). Additionally, μ is the total molecular viscosity, μ_t is turbulent eddy viscosity, σ^* is a turbulence model constant. $\vec{\tau}$ and $\vec{\lambda}$ are the molecular and turbulent Reynolds stress tensors (dyads), respectively, and \vec{q} and \vec{q}_t are the molecular and turbulent heat flux vectors, respectively. The pressure is given by Equation 5.

The averaging process for the Navier-Stokes equations described above, results in some unknown quantities, including the turbulent Reynolds stress tensor, $\vec{\lambda} = -\overline{\rho u'' u''}$. These quantities reflect the influence of the turbulence on the mean flow solution. The presence

of these unknowns creates a need for additional correlations in order to close the system of equations. The role of turbulence modeling is to provide appropriate approximations for these unknown terms. The turbulence modeling closures adopted in this thesis work are discussed next.

3.4. TURBULENCE MODELS

Four turbulence models, including the Spalart-Allmaras model, realizable k - ϵ model, non-linear k - ϵ model, and SST model were investigated to close the Favre-averaged Navier-Stokes equations. All four models were used for RANS simulations, while URANS simulations were only conducted using the Spalart-Allmaras model. The Spalart-Allmaras model was used where not otherwise noted. In literature, there are many different variants of each model; for clearness and completeness, each model is summarized, with values for the coefficients, in Appendix A. All of the closures rely on the Boussinesq assumption to relate the Reynolds stress tensor, $\vec{\lambda}$, to the mean flow strain-rate tensor, through a turbulent eddy viscosity, μ_t . The Boussinesq assumption is given by

$$\vec{\lambda} = -\overline{\rho \vec{u}'' \vec{u}''} = 2\mu_t \left(\vec{S} - \frac{1}{3} \vec{I} \vec{\nabla} \cdot \vec{u} \right) - \frac{2}{3} \vec{I} \rho k. \quad (15)$$

Note that because k is not readily available in the Spalart-Allmaras model, the term involving k in the Boussinesq assumption is ignored. The cubic k - ϵ model adds additional terms to the Boussinesq assumption to account for anisotropy of the mean flow strain-rate tensor.

Near-wall turbulence can be solved directly to walls on grids of sufficient resolution, using low-Reynolds number formulations. However, it is often the case in engineering practice that such grids are prohibitive due to their size and associated computational expense. For

simulations using coarse grids, in which the first centroids from the wall result in $y_1^+ > 1$, wall functions are commonly used to obtain momentum and energy fluxes for the wall boundaries. Specifics regarding the wall treatment used in the current work are presented in Appendix A.

3.5. CFD++ SOLVER AND SOLUTION METHODS

The CFD++ solver from Metacomp Technologies [26] was used for all simulations. CFD++ is an unstructured solver which uses a second-order, upwind, finite-volume method with an HLLC approximate Riemann solver to find solutions to the Reynolds-averaged Navier-Stokes equations using Gauss-Seidel relaxation accelerated with algebraic multi-grid. A number of turbulence models are available in the solver, including those described in Section 3.4. For transient simulations, second-order implicit dual time-stepping is used. Passing of information at sliding or zonal boundaries is accomplished with a second-order, least squares interpolation.

3.6. SIMULATION CONSIDERATIONS FOR SINGLE STAGE AND FULL ANNULUS

Steady-state simulations were performed for the rotor-alone geometry with an annular flow path. The computational domain included the full geometry presented by Strazisar [3], which corresponds to Figure 2.4a. In the axial direction, the domain extended approximately 0.4 rotor diameters upstream of the rotor's leading edge, to approximately 1 rotor diameter downstream of the rotor's leading edge. A single passage in the θ direction was considered. Uniform total pressure and total temperature were specified at the inlet boundary, and static pressure with radial equilibrium was specified at the outlet boundary. The hub, shroud, and rotor boundaries were specified as no-slip walls, with the entire shroud being stationary

in the absolute frame of reference. The hub, contiguous with the rotor, was specified to be stationary in the relative frame of reference, while elsewhere it was stationary in the absolute frame. The upstream location of the interface of spinning and stationary portions of the hub was specified to be consistent with the experiment [3], while the downstream interface was extended slightly from the experimental location. This was done in order to increase the grid quality in this region. Initial cases were specified with an initial condition of a uniform velocity and standard atmospheric values for pressure and temperature. The initial uniform velocity was chosen such that the initial mass flow rate at the inlet was within the rotor's operating range. Subsequent cases were often initialized with previous solutions in order to minimize run times. Except where otherwise noted, the Spalart-Allmaras turbulence model was used for all simulations completed in the current work. The steady-state simulations of the rotor-alone with an annular flow path were used to validate the CFD methods against the experimental data [3] and to determine grid dependence and turbulence modeling effects.

Steady-state simulations were also performed for the rotor-alone geometry with a center-body. The computational domain corresponded to Figure 2.4b, and extended to 2.5 rotor diameters upstream of the rotor in the axial direction and to the same distance downstream as that in the configuration of the rotor-alone with an annular flow path. A single passage in the θ direction was considered. To avoid the singularity in the mesh potentially resulting from rotation, a small tube was placed in the center at the axis. Boundary conditions for the inlet, outlet, rotor and shroud were the same as above (i.e. for the rotor-alone with annular flow path). The center-body wall was set as a rotating wall. The hub downstream of rotor was stationary in the absolute frame. The interface between spinning and stationary portions of hub was the same as above. The same initial conditions were prescribed as above.

Cases with this geometry were run in order to confirm that the addition of the spinner did not significantly alter results compared to those obtained with the annular flow path. Also, cases at part speed were run to compare against unpublished data from Strazisar, recorded in 2004, which used this geometry.

Steady-state simulations for the stage with a center-body (and no nacelle or nozzle) were performed. This configuration corresponded to Figure 2.4c. The computational domain was the same as that previously described (i.e. the rotor alone geometry with center-body), but with the addition of the stator blade. Boundary conditions were the same as previously stated, for example the stator blade was specified as a no-slip wall. The same initial conditions as above were applied. These cases were used to validate stage performance against unpublished data received from NASA.

Unsteady, full-annulus simulations of the stage with center-body (and no nacelle or nozzle) were performed. The meridional domain is illustrated in Figure 2.4c. The same boundary conditions as previously stated were used, except for the inlet boundary where an 11% total pressure deficit was specified over 120° of domain. This boundary condition was specified as shown in Figure 1.2. The initial condition was a solution from a clean flow mixing-plane simulation. The time step was set such that the moving zone rotates the distance of a single cell in θ (at the zones upstream and downstream boundaries). The time-step was approximately 7×10^{-6} seconds. These cases were used to validate stage performance against data shown by Fidalgo *et al.* [2] and to obtain useful flow field data for certain modeling purposes, the discussion of which is not permitted herein.

Both steady-state and unsteady simulations were performed for the stage with center-body, nacelle, and nozzle. The steady-state simulations considered only a single passage

in the θ direction, but the unsteady simulations included the full annulus. The farfield domain was extended to 50 rotor diameters in all directions, with a half sphere (with radius of 50 rotor diameters) upstream and cylinder downstream (length and radius of 50 rotor diameters). Three farfield flow conditions were examined with single passage calculations. These conditions were the static condition, take-off condition, and cruise condition, for which M_∞ was defined as 0, 0.25, and 0.8, respectively. The static and take-off condition assumed standard air at sea level, while the cruise condition assumed standard air at 35,000 ft. Static quantities and velocity were set at the farfield boundaries for cases at the take-off and cruise conditions. At the static condition, total pressure and total temperature were specified at these boundaries. For full-annulus simulations, only the take-off condition was examined. The nacelle was set as a no-slip wall. All other boundary conditions were set the same as described above. The initial condition for the single-passage simulations was a uniform flow field, and the initial condition for the full-annulus simulation was the solution from a multiple-reference frame simulation at same condition (i.e. the same M_∞ and AOA). The same time-step as previously described was used. These cases were investigated to understand component interactions and fan-distortion interaction.

Convergence of steady simulations was measured by observing the stability of the fan's pressure ratio and mass flow rate over the final iterations of a given case, as well as the levels of normalized residuals present at the end of the simulation. Generally, at least 4 orders reduction in the normalized residuals of the calculations was achieved. For unsteady simulations, normalized residuals were required to decrease by 2 orders of magnitude during the inner-iterations. Unsteady calculations were assumed to be converged after the mass flow rate through the fan reached a statistically steady state.

3.7. COMPUTATIONAL RESOURCES AND COSTS

Simulations in this thesis work were primarily performed on a high-performance compute server, maintained by the Computational Fluid Dynamics & Propulsion Laboratory at Colorado State University. The server consists of nine compute nodes and 24 TB of storage connected by a 40 Gbps Infiniband network. Four of the compute nodes each contain 20 Intel Sandy Bridge CPU cores, an Nvidia Tesla K20 GPU, and a 128 GB of memory. Five of the compute nodes are each configured with 24 Intel Haswell cores and 64 GB of memory. In total, there are 200 cores on the compute nodes. The server supports GPU-Direct RDMA so that MPI can be used to communicate between CPUs and GPUs.

Additionally, some simulations were performed on the ISTeC Cray High Performance Computing System built by Cray Inc. The ISTeC Cray is a XT6m model with 2,016 cores (computing devices), 2.5 terabytes of main memory and 32 terabytes of disk storage. The Cray system interconnect is based on the SeaStar2+ 2D torus topology with 6.5 us latency and 6.8 GB / second transfer speed.

The computational cost for a single-passage rotor-alone simulation with a grid of 2.3×10^5 cells was approximately 1 hour on 24 cores. The URANS simulations of the full-annulus stage on a grid with approximately 50 million cells was 1 revolution/day when using 120 cores. Approximately 15 revolutions were needed to achieve statistical convergence of the mean mass flow rate. Simulations for the full-annulus stage with nacelle and nozzle, using a mesh with more than 60 million cells took approximately 1 revolution/2 days and needed around 10 revolutions to converge.

3.8. DATA POST-PROCESSING

Analysis of data from single-passage CFD solutions was performed to obtain the aerodynamic performance of the rotor as well as pitch-averaged spanwise profiles of important flow quantities. Additionally, relative Mach number for blade-to-blade lines at constant chord and streamwise lines at constant pitch was extracted for direct comparison to experimental laser anemometry data. The locations of aerodynamic measurements stations as well as constant chord and constant pitch lines are described in detail in Section 3.8.3. In order to compare to contour plots derived from the same experimental data and to facilitate a better understanding of the flow, contour plots at constant spanwise locations were also extracted. The extraction of all data was performed by linearly interpolating the CFD solutions onto structured grids with Tecplot. Structured grids for data interpolation and processing were generated to match the CFD grids as closely as possible with respect to cell spacings, in an effort to minimize error in the interpolation. Solutions on structured grids were then post-processed to obtain the needed plots. Performance calculations and averaging were done with MATLAB. Data transfer between Tecplot and MATLAB was accomplished with a bash script written for that purpose. Bash scripts were used to automate all post processing procedures to ensure efficient and consistent post processing of the data. An example of a post-processing routine, using a Bash script, Tecplot macro, and MATLAB code is shown in Appendix B.

Full-annulus solutions of the stage were analyzed to determine the aerodynamic performance of the rotor and stage. Also, contour plots of important quantities were made from data extracted from slices normal to the axis of rotation. Slices normal to the rotational axis were taken from both instantaneous and time-averaged solutions. Some of these slices

were averaged in the circumferential direction with a moving mass flow rate weighted average, to allow for visualization of the flow field without the local influence of the blade rows. The width of the moving average envelope was that of a single periodic passage. This was done for slices downstream of the stator row, in order to remove the blade wakes. Slices of constant radius were extracted from instantaneous solutions. The constant radius slices were unwrapped and plotted in a plane with coordinates of x (axial coordinate) and $r-\theta$ (circumferential coordinate). Time averages were computed within the solver and the time averaging was done over 1 revolution after a converged solution was reached. Moving mass flow rate weighted averages were performed for total pressure in full-annulus simulations using Equation 16

$$\bar{P}_{0,N} = \frac{\sum_{n=N-0.5M}^{N+0.5M} P_{0n} \rho_n U_n A_n}{\sum_{n=N-0.5M}^{N+0.5M} \rho_n U_n A_n} \quad (16)$$

where N is the cell for which the average is determined and M corresponds to the number of cells in the circumferential direction of a single passage.

3.8.1. RADIAL PROFILES. Radial profiles of total pressure, total temperature, and relative flow angle were produced for each single-passage CFD simulation. Station locations at which radial profiles were obtained were those used by Strazisar *et al.* for aerodynamic surveys. These stations are shown in Figure 3.1. The flow field at each station location was averaged in the circumferential direction using a mass flow rate weighted average. The mass flow rate weighted averaging was performed on data interpolated to structured grids with lines of constant radius. The averaging was performed across all cells of a given radius (N), using Equations 17 - 19, where A is the cell area, and U is the velocity normal to the cell face. Only scalar quantities were able to be averaged in this manner, therefore, the relative

flow angle (β) was calculated from vector quantities before averaging.

$$\bar{P}_0 = \frac{\sum_{n=1}^N P_{0n} \rho_n U_n A_n}{\sum_{n=1}^N \rho_n U_n A_n} \quad (17)$$

$$\bar{T}_0 = \frac{\sum_{n=1}^N T_{0n} \rho_n U_n A_n}{\sum_{n=1}^N \rho_n U_n A_n} \quad (18)$$

$$\bar{\beta}_0 = \frac{\sum_{n=1}^N \beta_{0n} \rho_n U_n A_n}{\sum_{n=1}^N \rho_n U_n A_n} \quad (19)$$

3.8.2. PERFORMANCE CALCULATIONS. Aerodynamic performance of the rotor was determined for each CFD simulation and the aerodynamic performance of the stage was also calculated for solutions involving both rotor and stator. For rotor alone performance, slice and rake integrations were performed at the stations specified in the primary experimental reference [3] and shown in Figure 3.1. For stage performance, the same station upstream of the rotor was used as for the rotor-alone calculation, but the downstream station used was at the trailing edge of the stator blades. The total pressure ratio and efficiency were calculated both across the fan and across the stage for simulations involving both rotor and stator. To determine aerodynamic performance from slice data, total pressure and total temperature of slices at specified axial locations were averaged with a mass-flow rate weighted average. The total pressure ratio ($\frac{P_{02}}{P_{01}}$) was then determined across the fan and isentropic efficiency was calculated with Equation 20 [3].

$$\eta = \frac{\frac{P_{02}}{P_{01}}^{\frac{\gamma-1}{\gamma}} - 1}{\frac{T_{02}}{T_{01}} - 1} \quad (20)$$

Aerodynamic performance was also calculated using rake data in order to allow for comparison to experimental data. Circumferentially averaged radial profiles, as described above,

were linearly interpolated to the radial locations used in the experiment which were comprised of 9 survey locations between the hub and shroud. The data points at each station were then averaged to obtain a value at each station for total pressure and total temperature, which was again used to calculate aerodynamic performance. The radial distributions of total temperature were averaged with mass flow rate weighting, and the total pressure distributions were averaged with the energy average method used in reference [3]. The total temperature average was consistent with Equation 18. The average of total pressure was performed using Equation 21, in which the total pressures are converted to their enthalpy equivalents and then mass averaged. In Equation 21, the ΔA is the incremental annulus area, which was taken directly from reference [3].

$$\bar{P}_0 = \left[\frac{\sum_{n=1}^N P_{0n}^{\frac{\gamma-1}{\gamma}} \rho_n U_n (\Delta A_n)}{\sum_{n=1}^N \rho_n U_n (\Delta A_n)} \right]^{\frac{\gamma}{\gamma-1}} \quad (21)$$

3.8.3. FLOW FIELD DATA EXTRACTION FOR COMPARISON WITH LASER ANEMOMETRY DATA. A structured grid with lines of constant pitch and constant chord, all at a constant spanwise percentage was used to extract flow field data for comparison with Laser Anemometry (LA) data. These grids had 1000 vertices in the streamwise direction and 200 vertices from blade-to-blade. The spanwise positions of the grids were obtained by projecting to a surface created from data presented by Strazisar *et al.* [3]. As stated previously, this thesis adopts the convention defined by Strazisar *et al.* [3] when referencing spanwise location, with 0% span being defined at the shroud as shown in Figure 3.2, although modern convention defines the hub as being at 0% span [2]. Furthermore, it is notable that the spanwise locations defined by Strazisar *et al.* [3] were only calculated from the design streamlines at a number of discreet axial locations (i.e. rake measurement stations and the rotor's leading

and trailing edges); between these points, straight-line interpolation was used. Locations of constant span lines are shown in Figure 3.1. Grids for interpolation were generated at 10%, 30%, and 70% span from the shroud.

A schematic representation of lines of constant pitch and constant chord, for which relative Mach number data were extracted from CFD solutions and compared to LA data, is shown in Figure 3.2. Pitch within the passage was determined by the circumferential coordinate at any given axial location. The suction surface of the blade was taken to be at 0% pitch, and the pressure surface of the contiguous blade was taken to be at 100% pitch. Outside of the passage, 0% and 100% pitch were taken to be at lines extended from the leading and trailing edges at the blade inlet and outlet angles, respectively. A schematic representation of a 50% pitch line is shown in 3.2. Chord was defined by the axial distance between the leading and trailing edges of the blade at a given span, with 0% chord being defined at the leading edge of the blade and 100% chord being defined at the trailing edge of the blade. A schematic representation of constant chord lines outside of the blade passage is shown in Figure 3.2.

Because the interpolation grids had lines of constant pitch, they were not entirely within the domain of the computational grids. Interpolation required repeated rotation by the periodicity of the blade; then interpolating onto the section of the interpolation grid contained within the computational grids. Streamwise and chordwise locations of each grid point were calculated using a Tecplot macro and added to the interpolation grid as variables. Indices corresponding to the desired constant pitch or constant chord line were then extracted, and plotted against LA data. This procedure was only applied for single-passage solutions.

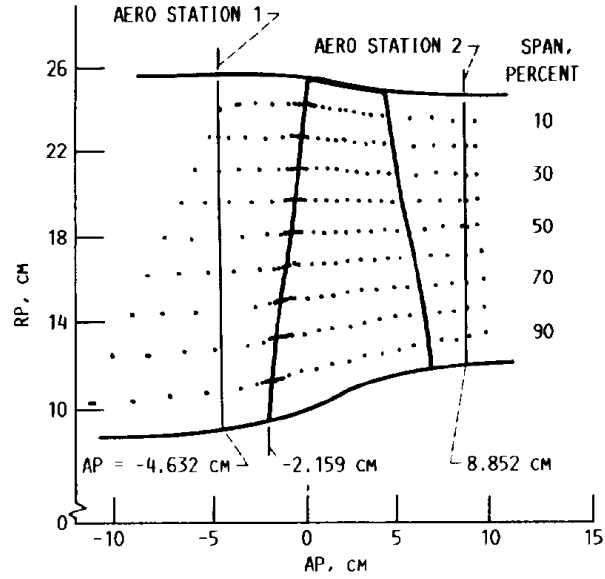


FIGURE 3.1. Aerodynamic survey stations and locations for laser anemometry data in the meridional plane. Figure taken from [3].

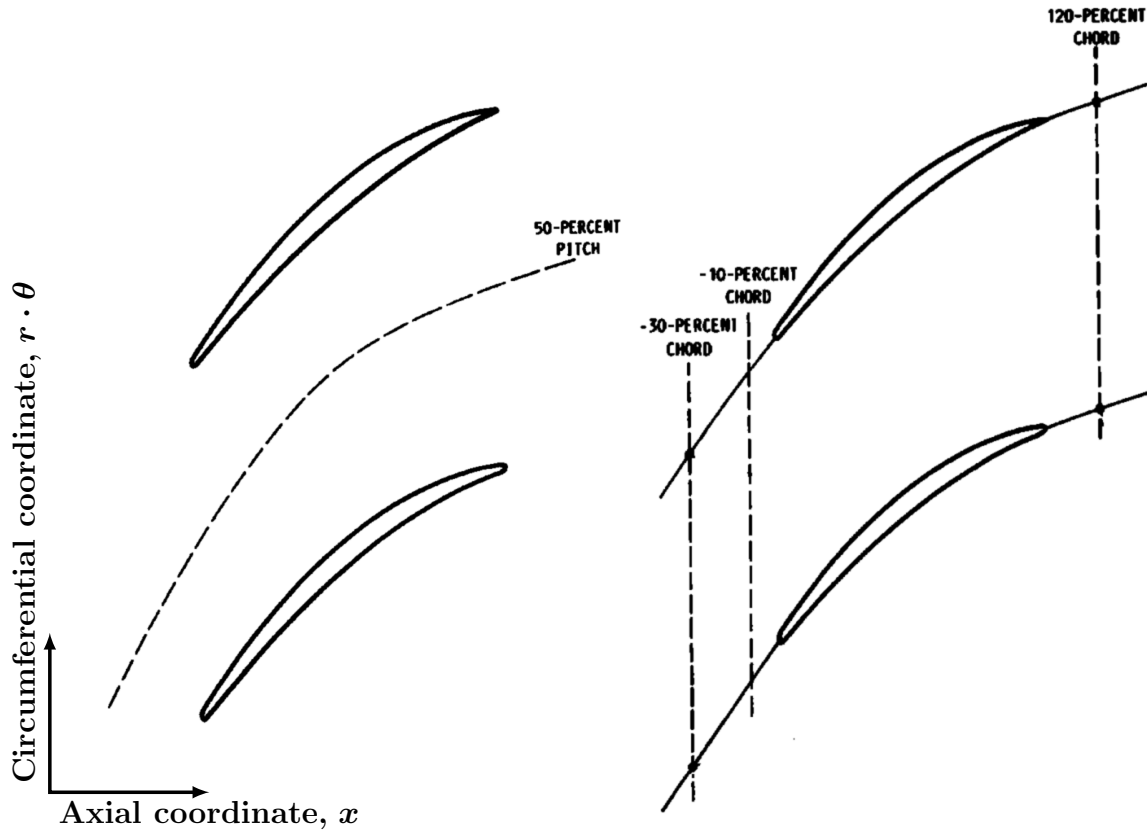


FIGURE 3.2. Schematic representations of constant pitch lines (left) and constant chord lines (right) used to plot data in streamwise and blade-to-blade directions, respectively. Figure adapted from [3]

3.8.4. FLOW FIELD DATA. For single-passage simulations, the data interpolated onto the grids used for comparison with LA data were also plotted in full, as contour plots. These blade to blade plots use $r \cdot \theta$ and the axial location as coordinates.

Flow field data for the full-annulus stage simulations was plotted by extracting data from isosurfaces of constant axial coordinate and isosurfaces of constant radial coordinate.

CHAPTER 4

RESULTS AND DISCUSSIONS

4.1. SINGLE PASSAGE

4.1.1. ROTOR ALONE. Comparisons of CFD predictions with experimental data along constant pitch lines and constant chord lines, such as those schematically represented in Figure 3.2, were performed at two operating points: peak efficiency and near stall. These conditions are defined based on the ratio of the corrected mass flow rate to the choked corrected mass flow rate and are specifically $\frac{\dot{m}_{corr}}{\dot{m}_{corr,choke}} = .989$ and $\frac{\dot{m}_{corr}}{\dot{m}_{corr,choke}} = .924$ for the peak efficiency condition and the near-stall condition, respectively. This is consistent with the definition of these conditions by Strazisar *et al.* [3]. Mass flow rates were corrected based on stagnation quantities mass-averaged upstream of the rotor. Constant pitch lines were selected at the 50% pitch location. The location and strength of the shocks at the leading edge and in the passage are easily compared along these constant pitch lines, as is the fan’s influence on the overall flow field. Constant chord lines were chosen to match those used by Chima [1]. Chima chose constant chord lines for each span location and operating condition such that a line traversed the passage shock, and another line traversed the wake. Moreover, laser anemometry data are available for the chosen chord and pitch locations.

Figures 4.1 – 4.10 show comparisons of results from CFD simulations on seven grids, as described in Chapter 2.2.2, with experimental data. These comparisons have two purposes: to assess the dependence of the solutions on overall grid resolution, and to determine the effect of the first y^+ on the simulations. The following discussion refers to grid pairs, as well as the terms “off-body” and “near-body”, all of which are previously defined in Chapter 2.2.2. Inferences regarding the dependence of CFD simulations upon overall grid resolution and the

effect of the first y^+ are made in the discussion that follows, based on comparisons between solutions within each grid series and between grids in pairs.

Relative Mach number along constant pitch lines is shown in Figures 4.1 – 4.3 for the rotor alone operating near the peak efficiency point, and in Figures 4.4 – 4.6 for an operating point near the stall condition. Relative Mach number along constant chord lines is shown, for the same two operating conditions, in Figures 4.7 – 4.8. Radial profiles of total pressure, total temperature, static pressure, and absolute flow angle are shown in Figures 4.9 – 4.10, again for the same two operating conditions.

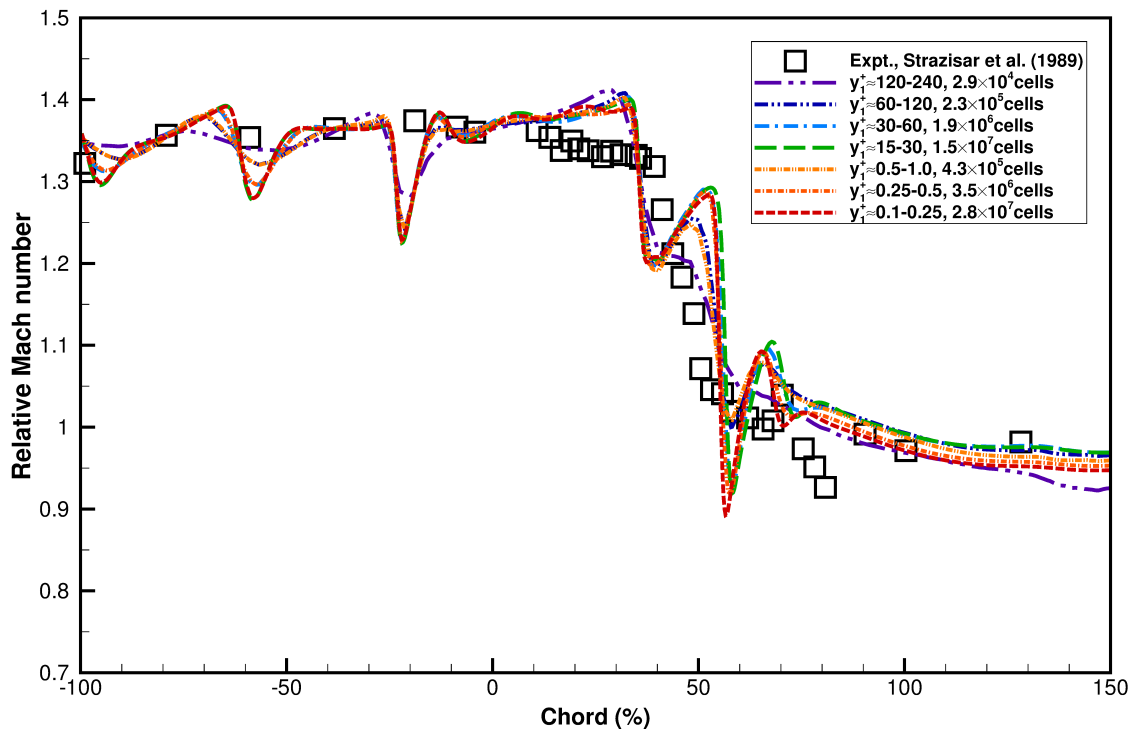


FIGURE 4.1. Relative Mach number at 10% span from the shroud and at 50% pitch, for the rotor alone operating near peak efficiency.

In Figure 4.1 the relative Mach number near the shroud (at 10% span from the shroud), clearly show the influence of leading edge shocks of nearby blades on the flow upstream of the rotor, indicated by oscillations in relative Mach number from -100% chord to 0% chord. This is most apparent at approximately -20% chord, where the constant pitch line

traverses the bow shock extending from near the suction surface of the contiguous blade. The peak Mach number of the flow before the leading edge (bow) shock is overestimated in the CFD solution at 10% span in comparison to the experimental data, but the shock location appears to be predicted correctly. Note again that in this work the span is defined from the shroud, for example 70% span is near the hub. While the CFD data from all grids but the coarsest distinctly show the shocks at the leading edge and within the passage, these features are smeared together in the experimental data. This is not surprising considering the low resolution in the experimental data and the inability of seed particles to decelerate with the flow across the shocks. The relative Mach number of the flow downstream of the rotor appears to be predicted correctly.

Figure 4.1 indicates that a grid independent solution is achieved. The prediction of the upstream influence of the fan is significantly affected by the off-body grid spacing, but appears unaffected by the wall spacing, where $y_1^+ < 1$. This is most apparent in the data farthest upstream, in which the pairs of grids with identical off-body meshes have nearly identical solutions. Also, in this region, a large difference is noticed between grids with different off-body meshes with coarser grids significantly dissipating the upstream influence of the rotor's leading edge shock. However, as the leading edge shock of the contiguous blade is traversed at approximately -20% chord, solutions on all but the coarsest grid have nearly collapsed to the same relative Mach number.

Solutions within the blade row are again observed to be largely paired according to the off-body grid spacing. Notably, the two grid pairs with the highest resolution produce very similar solutions across both the leading edge shock and the passage shock, showing grid independence at the second finest grid level. As would be expected, coarser grids smear

the shock more. The coarsest grid smears the shock to such an extent that acceleration is captured between the leading edge shock and the normal shock within the passage (passage shock). Interestingly, this qualitatively corresponds most closely to the experimental data.

Downstream of the passage shock, from approximately 80% chord to 150% chord, the relative Mach number appears to depend on y_1^+ of the grids. Relative Mach number of solutions on grids which resolve the boundary layers in greater detail is lower than on grids with the same off-body spacing but with less near-body resolution.

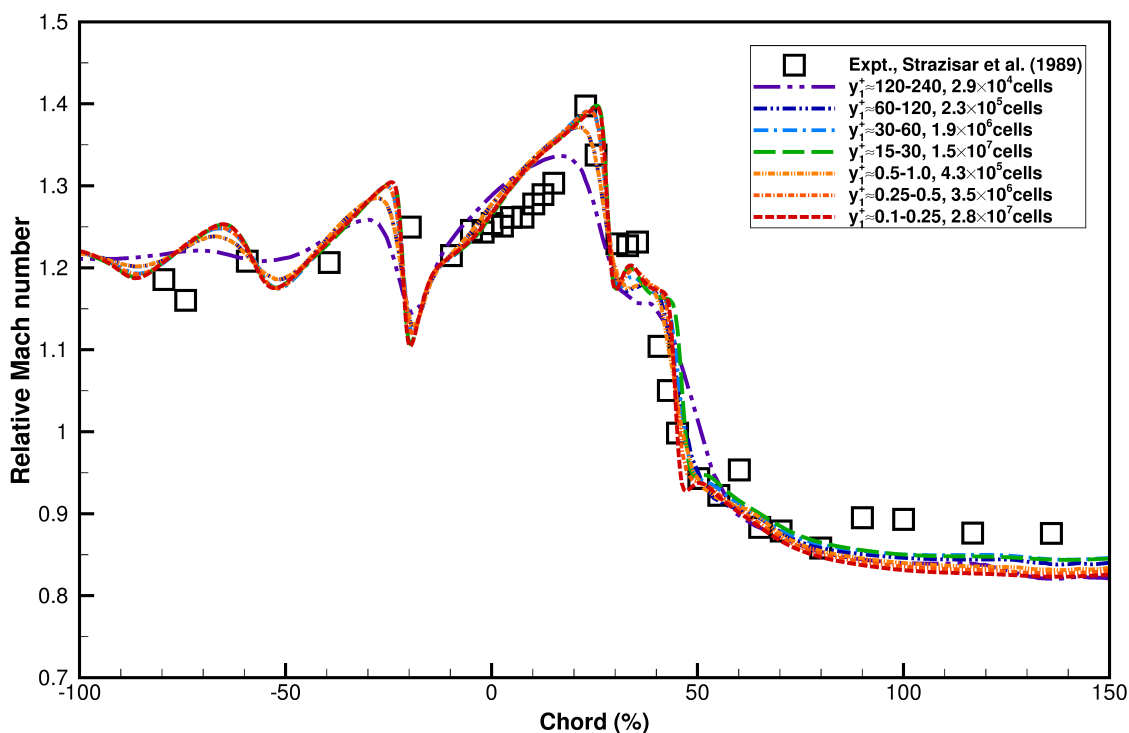


FIGURE 4.2. Relative Mach number at 30% span from the shroud and at 50% pitch, for the rotor alone operating near peak efficiency.

Figure 4.2 compares the CFD simulations to the experimental data at 30% span. In general, similar behavior to the 10% span data is observed for the flow upstream of the rotor. The CFD simulation agrees well with the experimental data overall. However, we suspect that the experimental data is too coarse to capture the variations of relative Mach number in this area. At this span, the peak relative Mach number upstream of the leading

edge shock is not overpredicted by the CFD data, as was the case at 10% span. Conversely, the relative Mach number of the flow downstream of the rotor along the constant pitch line at 30% span is underpredicted. The shock locations are predicted well at 30% span and the distinction between the leading edge and passage shocks is more similar to the experimental data than in the data at 10% span. Assuming that the dissipation near the shock in the experimental data was due to the differences between the seed particles and the fluid flow across the shocks, the presence of a weaker shock at 30% span than that at 10% span makes this similarity unsurprising.

Furthermore, it is found that the near-body and off-body grid spacing effects on the CFD simulations are similar between 30% span and 10% span. The coarser off-body grids dissipate the upstream influence of the rotor. However, the CFD simulations on all grids except the coarsest, have very similar behavior within the blade passage. Predicted relative Mach number of the flow exiting the rotor is slightly lower for grids with large y_1^+ than for grids with smaller y_1^+ .

The prediction of relative Mach number at 70% span is also examined and compared to the experimental data; a good agreement is observed as shown in Figure 4.3. The only shock present at this spanwise location is the leading-edge shock, which is much weaker than that at other locations examined. The CFD solution predicts the acceleration of the flow at approximately 0% chord, which is slightly more upstream than that shown by the experimental data. The peak magnitude of the relative Mach number is well predicted, as is the magnitude downstream of the rotor. Some acceleration of the flow after the leading edge shock is shown in the CFD prediction, whereas the experiment does not observe this behavior. Moreover, CFD solutions are not quite as sensitive to the meshes as at other

spanwise locations, as seen in Figure 4.3. However, the results from the coarsest grid are again noticeably different than those obtained from other grids. The good agreement can largely be accredited to the fact that the flow is relatively smooth at locations nearer to the hub.

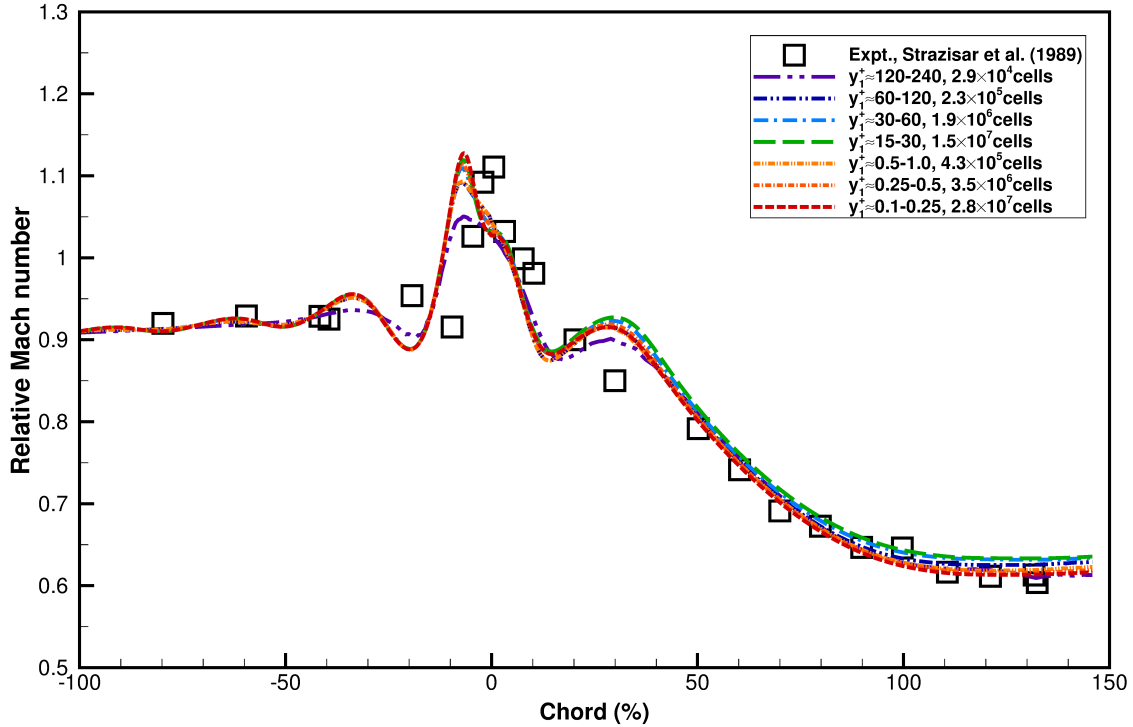


FIGURE 4.3. Relative Mach number at 70% span from the shroud and at 50% pitch, for the rotor alone operating near peak efficiency.

CFD solutions are also obtained for the rotor alone operating at the near stall point. In Figure 4.4, profiles of relative Mach number along a constant pitch line and at 10% span from the shroud are illustrated. Overall, the CFD predictions match the trend well with the experimental observations. The shock location is predicted accurately, as is the relative Mach number of the flow exiting the passage. The magnitudes of the oscillations in relative Mach number, upstream of the rotor, are closely matched between solutions on pairs of grids, although some dispersion is apparent. It can be observed that one single shockwave is present near the tip, as opposed to the two shockwaves that are present in the peak efficiency case.

In this case, CFD solutions at this location are much more sensitive to the grid resolution than for the peak efficiency case. In particular, y_1^+ values are critical for solution accuracy. For example, in addition to the greater resolution of the shock on finer off-body grids, there is also a significant difference in the resolution of the shocks between grids with the same off-body spacing and different near body spacing. At approximately 20% chord, the 2 finest grids with $y_1^+ < 1$ show a cusp, while the finest grids with $y_1^+ \gg 1$ do not. This is likely due to the fact that the grids with $y_1^+ < 1$ have many more spanwise cells in the shroud region; thus the interaction of the shocks with the boundary layer flow at the shroud can be resolved more accurately. The most significant differences between solutions on various grid levels are seen immediately downstream of the passage shock, near 50% chord. The minimum relative Mach numbers at the downstream edge of the passage shock are very sensitive to the grids, as are the subsequent downstream maxima. These differences are gradually diminished as the flow continues downstream.

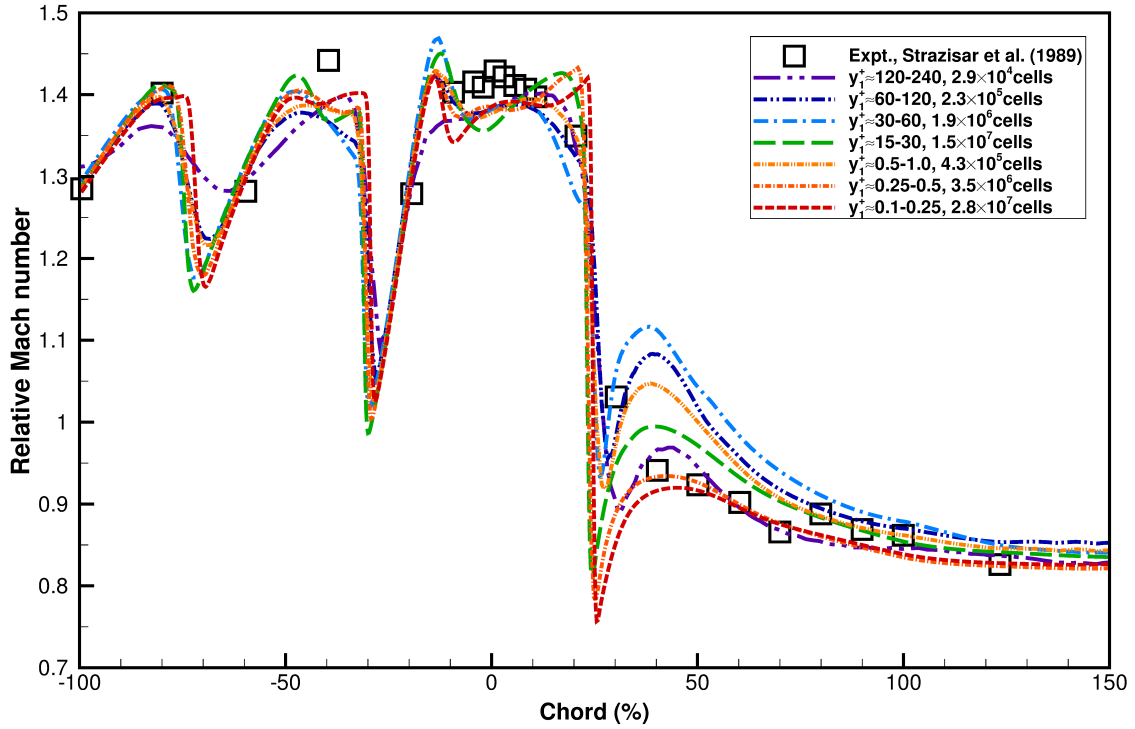


FIGURE 4.4. Relative Mach number at 10% span from the shroud and at 50% pitch, for the rotor alone operating near stall.

Figures 4.5 – 4.6 plot the relative Mach number for span locations of 30% and 70%, respectively. Overall, the spread of CFD solutions is much less nearer to the hub. The general agreement of the CFD predictions with the experimental data is excellent.

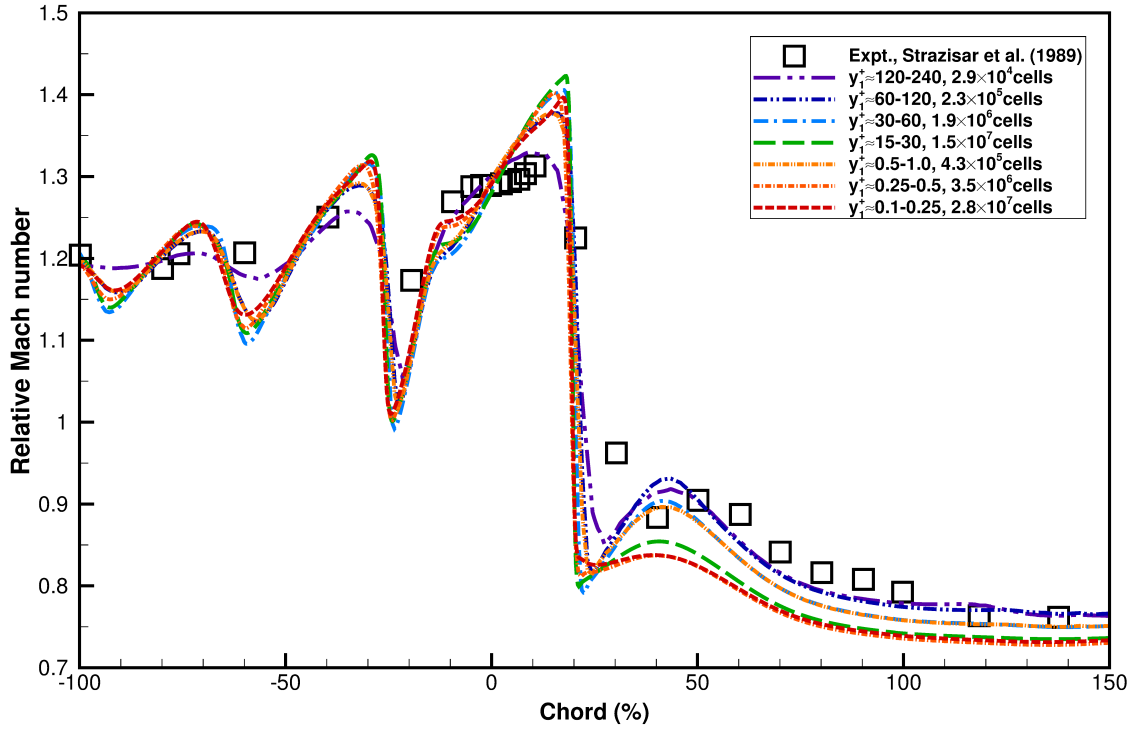


FIGURE 4.5. Relative Mach number at 30% span from the shroud and at 50% pitch, for the rotor alone operating near stall.

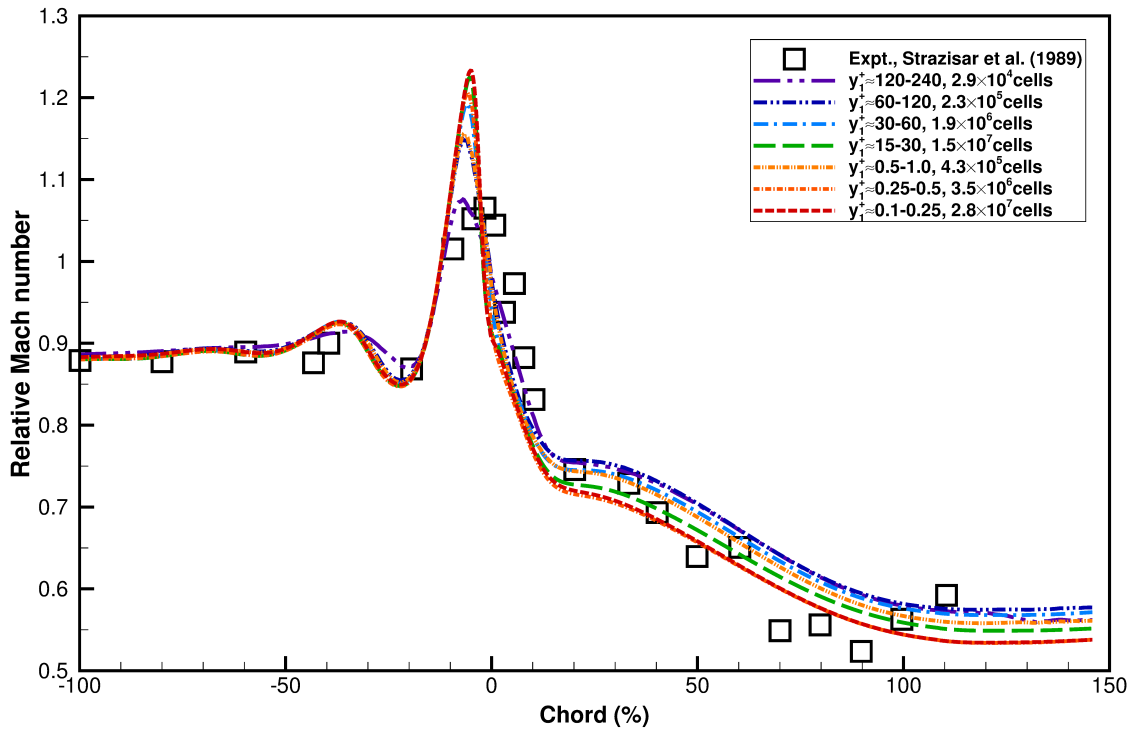


FIGURE 4.6. Relative Mach number at 70% span from the shroud and at 50% pitch, for the rotor alone operating near stall.

Figure 4.7 compares the CFD predictions of relative Mach number across constant chord lines to experimental measurements for the operating point near peak efficiency. Clearly, the shock locations of the shockwaves are accurately predicted and the computed profiles agree reasonably well with the experimental data. Near the pressure surface, the Mach number is higher than the predicted for the experimental case. According to Chima, this may be due to statistical uncertainty in the experimental data at this point, due to presence of few seed particles [1]. Additionally, there may be some further experimental error here, as this measured region appears to be within the blade metal. The predicted relative Mach numbers of flow in the wake region are lower than measured near the shroud, but agree more closely towards the hub. The minimum Mach number within the wake is deeper than measured. Again, it is suspected that the inability of experimental seed particles to follow flow with high shear rates accounts from this discrepancy.

Figure 4.8 compares the predicted relative Mach number to that measured for the operating condition near the stall point. The CFD predictions match the experimental measurements reasonably well in terms of the trend. However, the shockwaves and the wake profiles are more dissipated in the measurements than in the CFD computations. The Mach numbers in the wake region match more closely in this case than those at the peak efficiency, although the computed wake profiles are still much deeper than those measured.

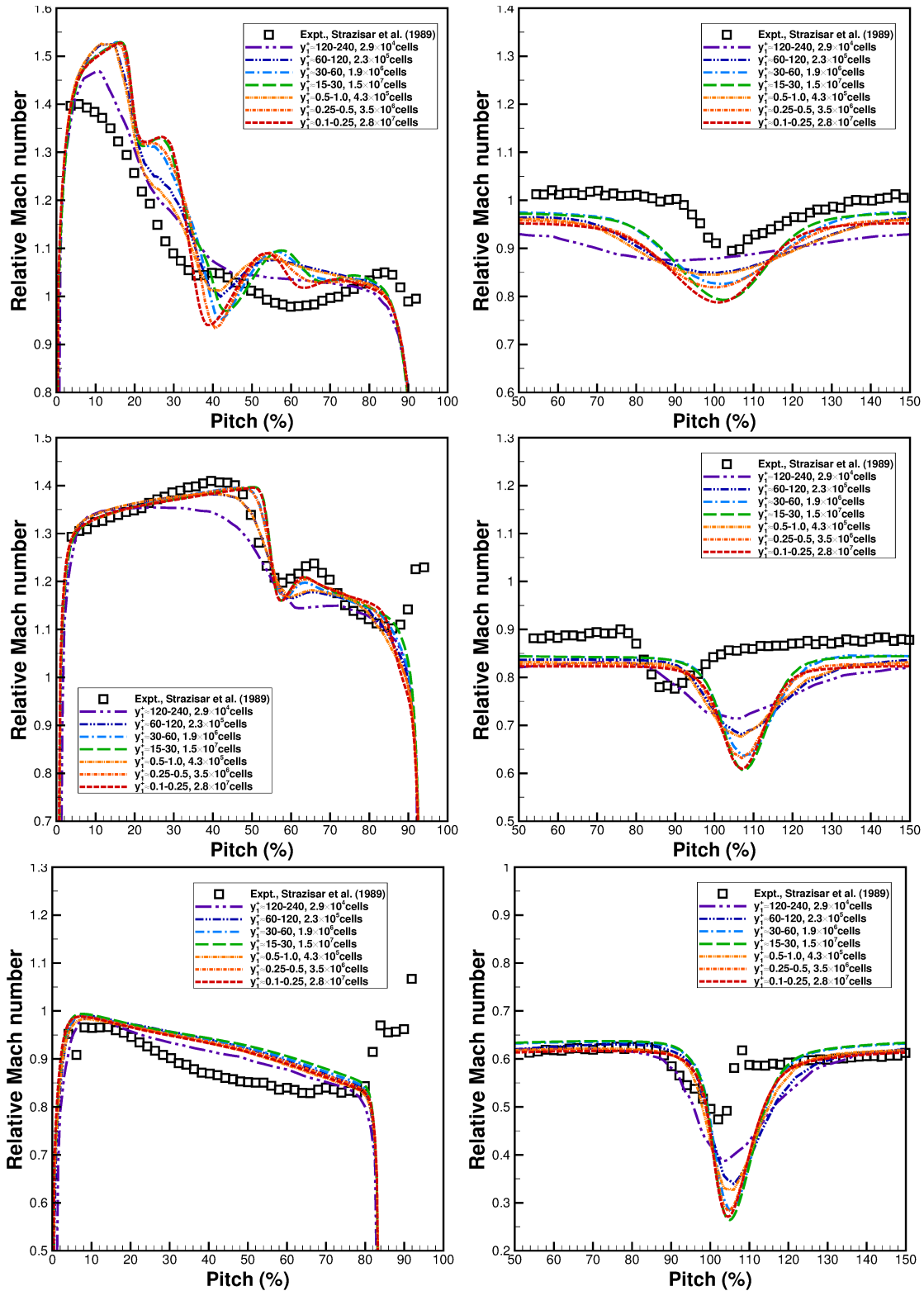


FIGURE 4.7. Relative Mach number at 10% (top), 30% (middle), and 70% (bottom) span from the shroud and at 63% (top-left), 188% (top-right), 25% (middle-left), 136% (middle-right), 30% (bottom-left), 121% (bottom-right) chord, for the rotor alone operating near peak efficiency.

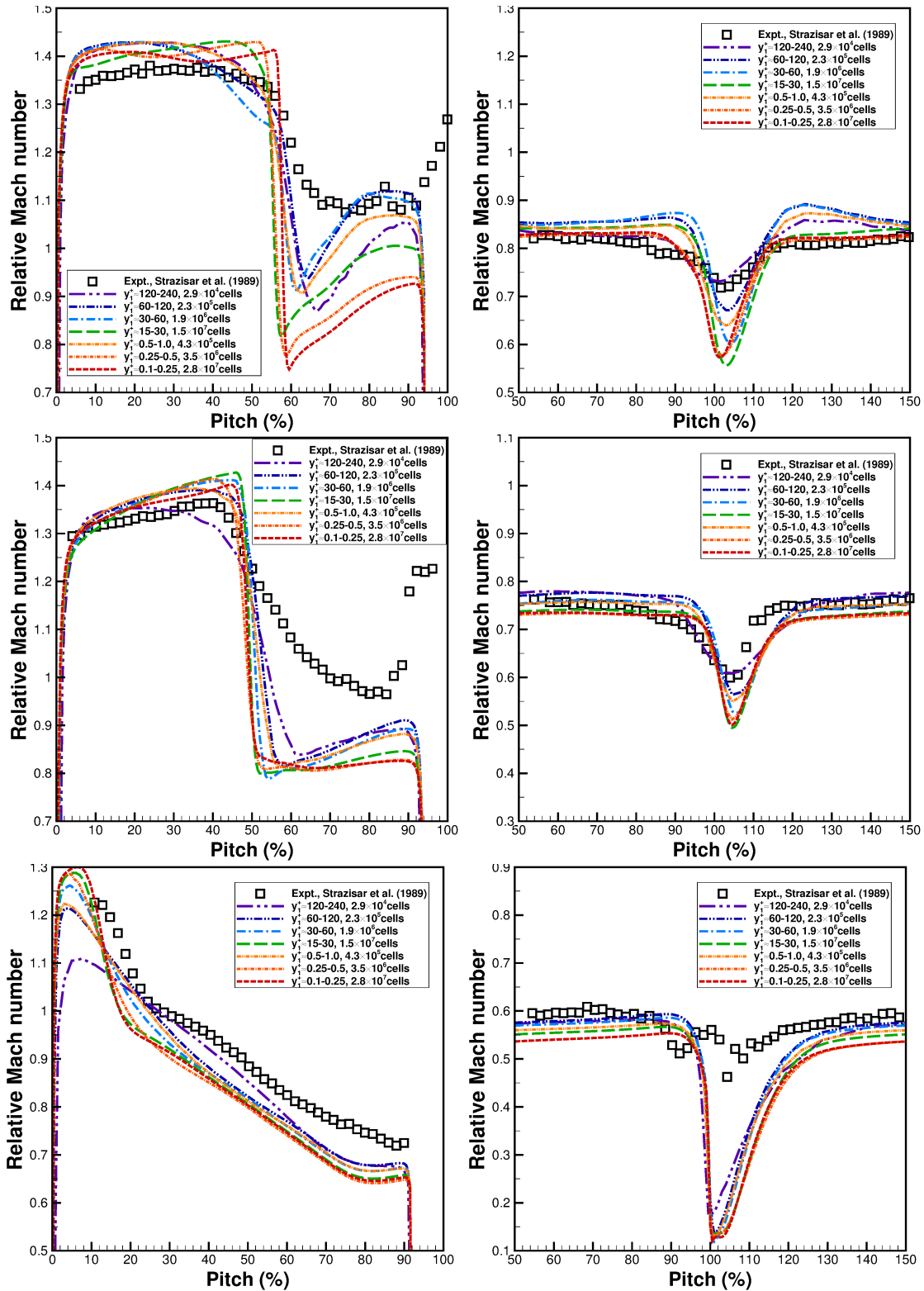


FIGURE 4.8. Relative Mach number at 10% (top), 30% (middle), and 70% (bottom) span from the shroud and at 20% (top-left), 123% (top-right), 20% (middle-left), 118% (middle-right), 7.5% (bottom-left), 110% (bottom-right) chord, for the rotor alone operating near stall.

We also examine the radial distributions of the total pressure, total temperature, static pressure, and relative flow angle. These profiles are compared to experimental profiles in Figures 4.9 – 4.10. Both operating conditions at peak efficiency and near the stall point are considered. Legends for these figures are identical to those used in Figures 4.1 – 4.8. Figure 4.9 shows the CFD radial profiles of total temperature, static pressure, and relative flow angle match the measured ones closely. Solutions show minimal dependence upon the grid size. The total pressure is underpredicted near the tip region. Additionally, it fails to capture the minima near 60% span from the shroud. Total pressure also appears to be much more sensitive to grid size than the other variables. Predictions using grids with smaller y_1^+ match the measured values more closely, especially near the tip. Figure 4.10 shows that the predicted total temperature, static pressure, and relative flow angle agree closely with the measured data. Clearly, the CFD simulations at the near-stall point are more sensitive to the mesh than those at the point near peak efficiency. Similarly to the cases near peak efficiency, the profile of total pressure appears very dependent upon the grid size, and grids with greater resolution near the wall match measured results more closely. Total pressure is again underpredicted near the tip; however, the finest mesh produces a solution that matches the experimental data well.

It is worth noting that, overall, the results shown in Figures 4.7 – 4.10 match results obtained by Chima [1] very closely.

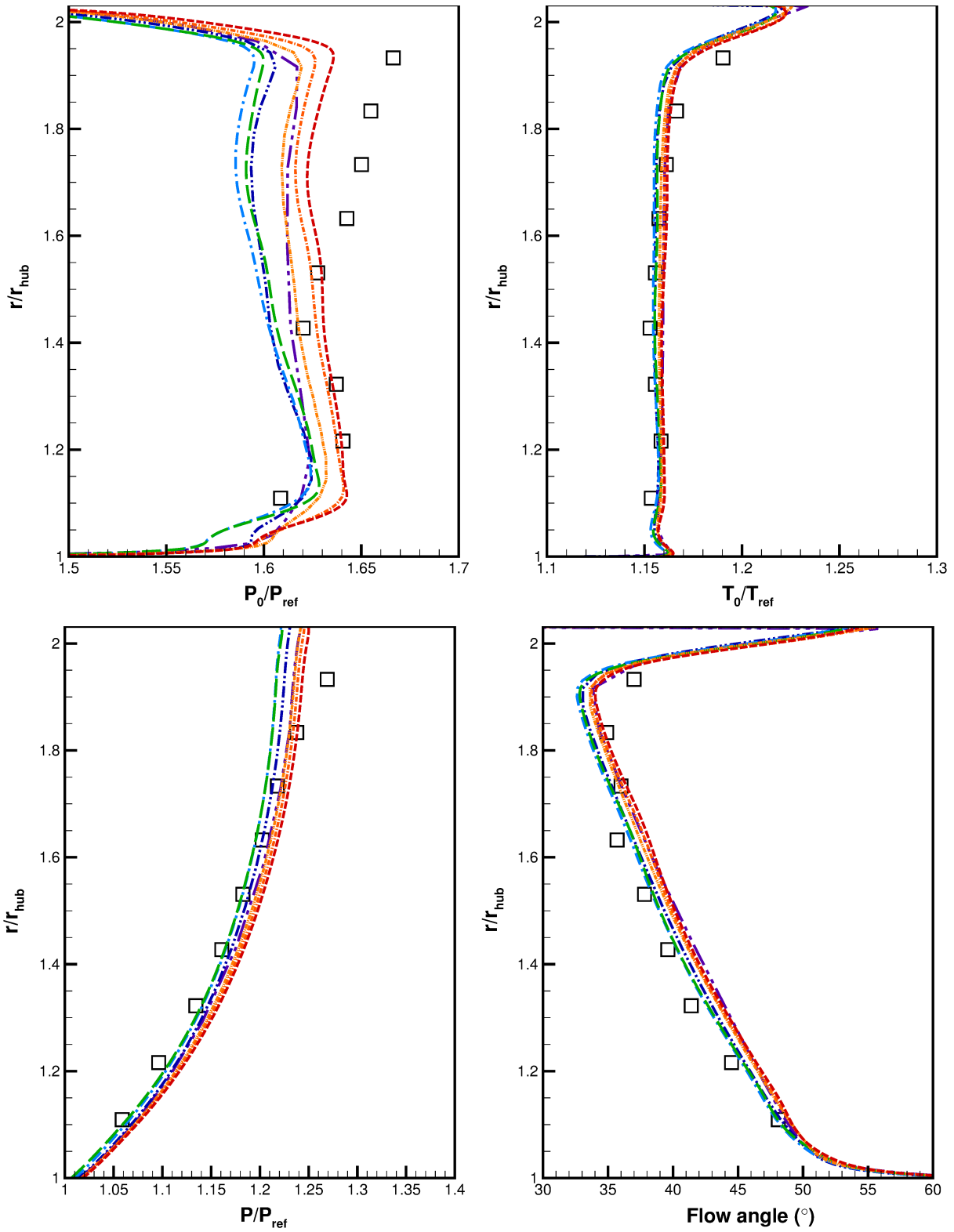


FIGURE 4.9. Spanwise distributions of total pressure (top-left), total temperature (top-right), static pressure (bottom-left), and exit flow angle (bottom-right) for the rotor alone operating near peak efficiency.

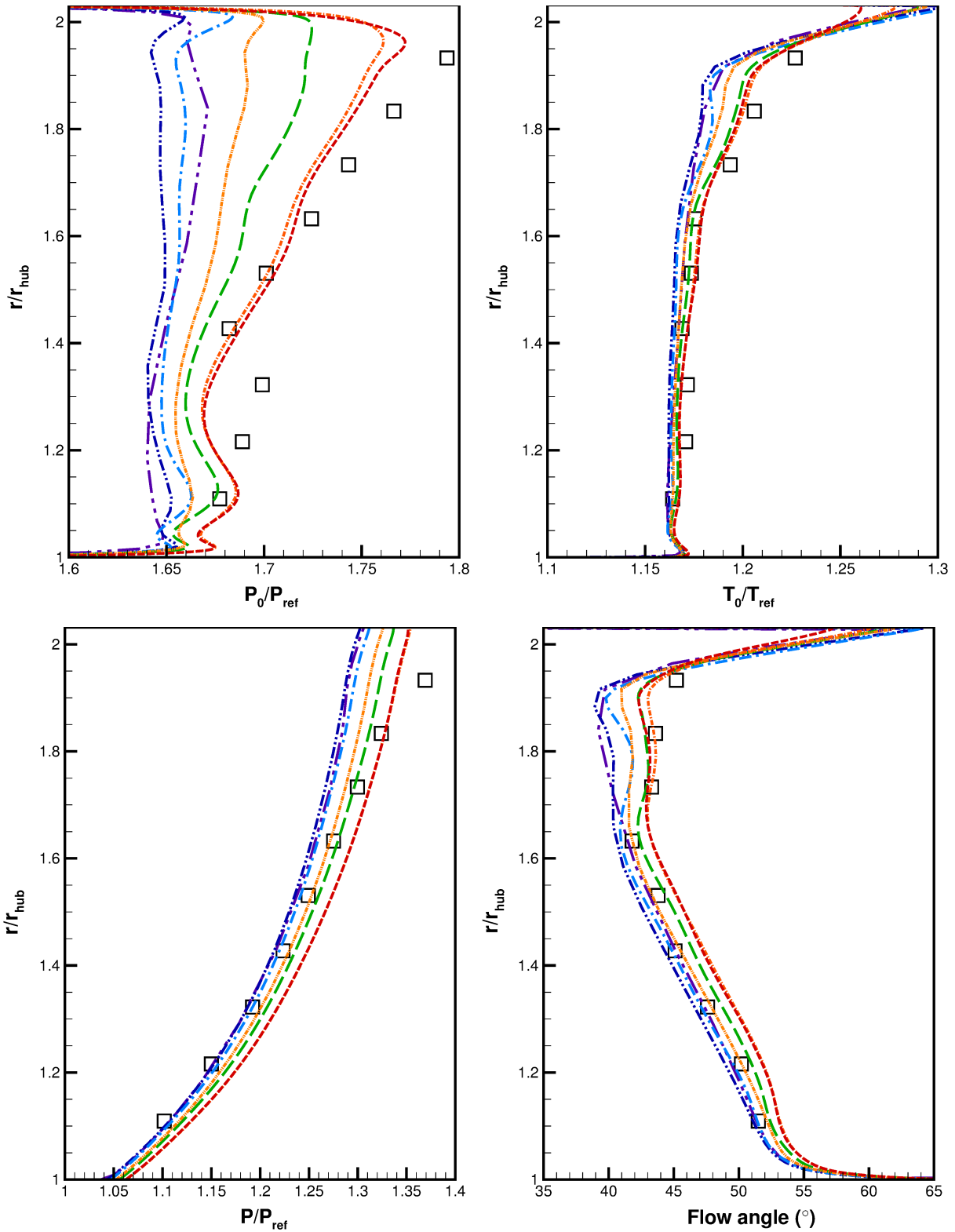


FIGURE 4.10. Spanwise distributions of total pressure (top-left), total temperature (top-right), static pressure (bottom-left), and exit flow angle (bottom-right) for the rotor alone operating near stall.

The details of contours of relative Mach number in the rotor passage for both operating conditions: near peak efficiency and near stall are examined. The Mach contours are studied for the three span locations, 10%, 30%, and 70%. Figures 4.11 – 4.12 present comparisons between the predicted and experimental contours. The latter were created from interpolated and smoothed LA data [3]. Figure 4.11 shows excellent agreement between the experimental contours and the CFD predictions, both qualitatively and quantitatively. Not surprisingly, the complex shockwave structures at 10% span and 30% span, including a detached leading edge shock and a normal shock in the passage, are much more resolved in the CFD data than the experimental, due to spatial resolutions. However, the wake shown in the contour from measured data at 70% span, is offset from the blade, which is not observed in the CFD solutions.

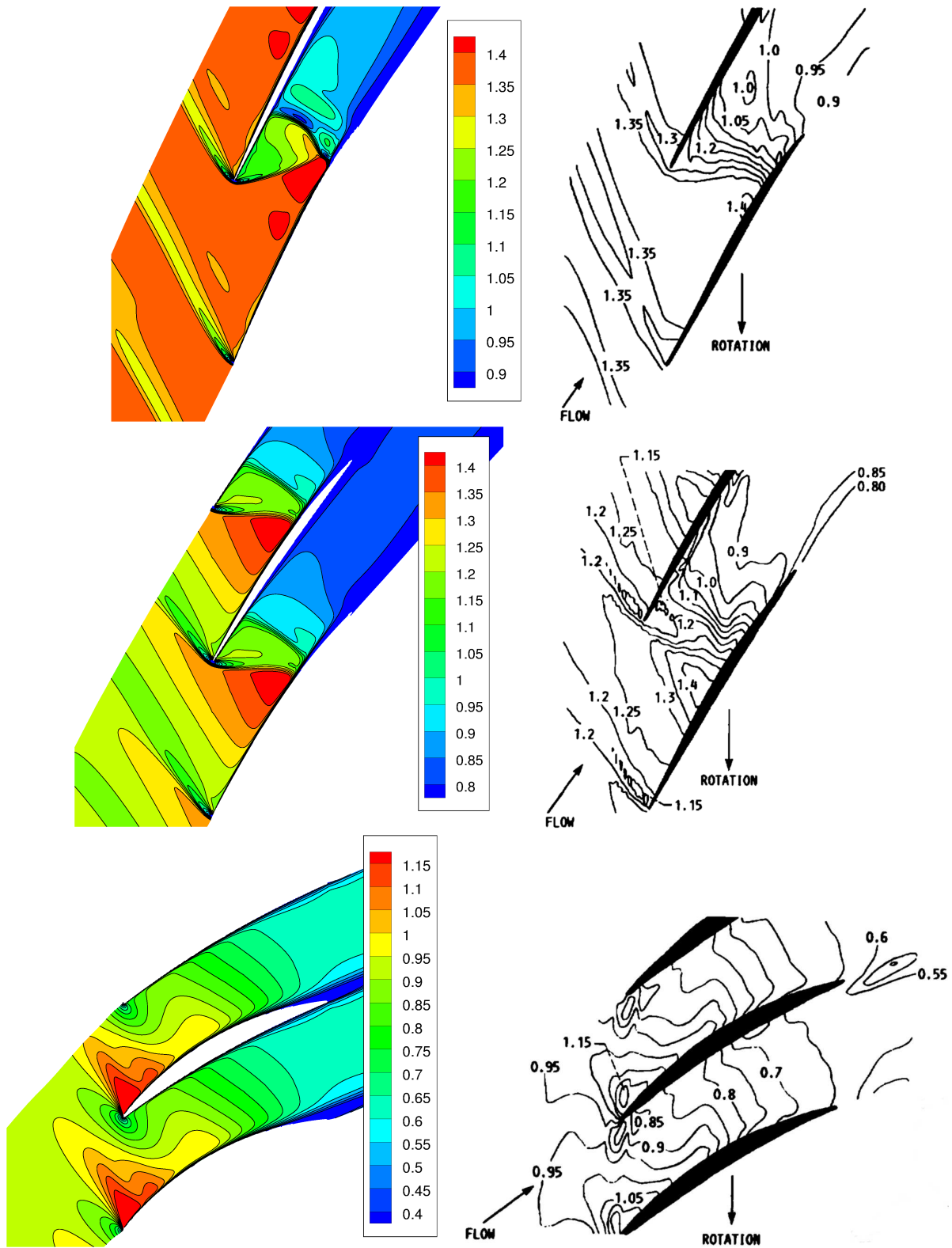


FIGURE 4.11. Contours of relative Mach number for the rotor alone operating at peak efficiency. Experimental (left) and CFD results were calculated on a grid with 2.8×10^7 cells and $y_1^+ < 1$ (right); 10% span from the shroud (top), 30% span from the shroud (middle), and 70% span from the shroud (bottom).

Figure 4.12 compares the contours for an operating point near stall. At 10% span, the shock predicted by CFD is stronger, farther forward, and more orthogonal to the flow than that from the experiment. This may account for the discrepancies in radial profiles of total pressure near the tip, as shown in Figure 4.10. Interestingly, although the CFD simulations include tip gap, the predictions are very similar to those by Chima [1], in which the tip gap was not included. This may indicate that the interaction of the tip vortex with the shock is not captured properly in the present CFD simulations, despite a large number of cells in this region. For the contours of 30% span and 70% span, a good agreement between the CFD results and experimental results is observed. The change in position of the shock is clear between the two operating points. The normal shock sits in front of the leading edge for the rotor operating point near stall, whereas it is swallowed in the peak efficiency case.

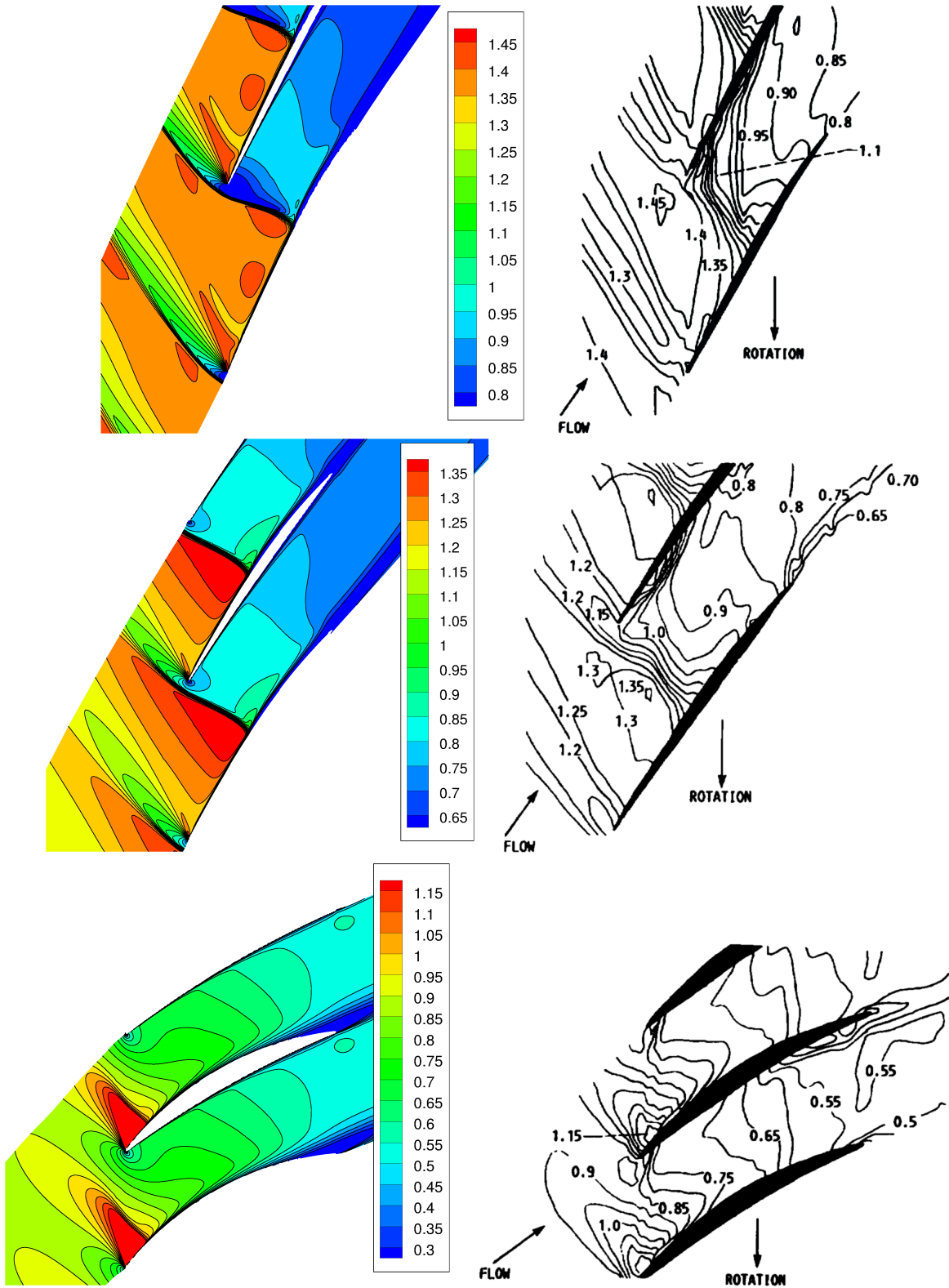


FIGURE 4.12. Contours of relative Mach number for the rotor alone operating near stall. Experimental (left) and CFD results were calculated on grid with 2.8×10^7 cells and $y_1^+ < 1$ (right); 10% span from the shroud (top), 30% span from the shroud (middle), and 70% span from the shroud (bottom).

Furthermore, the grid's effect on the flow dynamics was studied. Figures 4.13 and 4.14 show grid dependence of the solutions for the flow at the 10% span location. As expected, shocks are more dissipated on coarser grids. Shock induced boundary layer separation is clearly demonstrated in solutions on all grids.

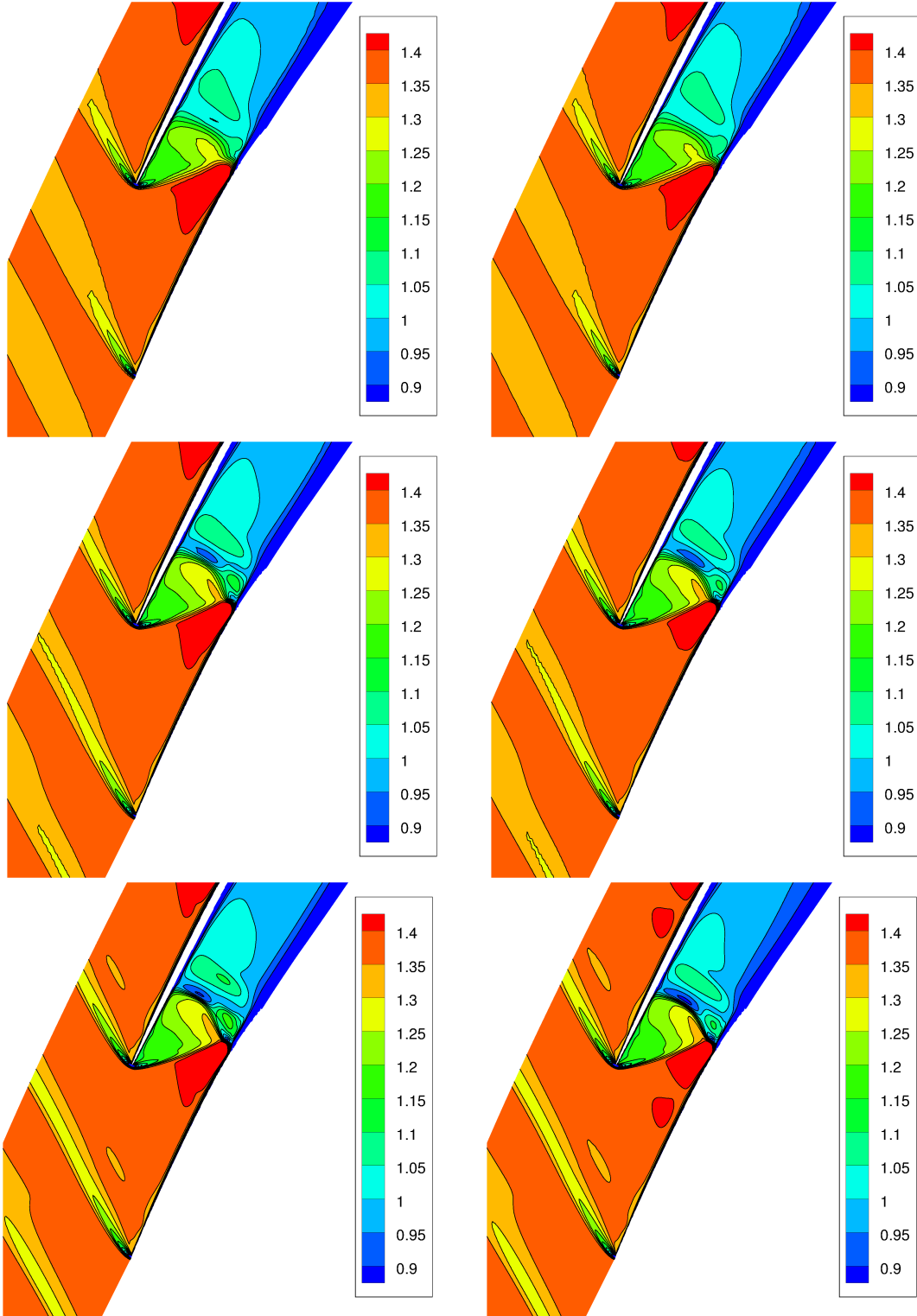


FIGURE 4.13. Contours of relative Mach number at 10% span from the shroud for the rotor alone operating at peak efficiency; 2.3×10^5 cells (top-left), 4.3×10^5 cells with $y_1^+ < 1$ (top-right), 1.9×10^6 cells (middle-left), 3.5×10^6 cells with $y_1^+ < 1$ (middle-right), 1.5×10^7 cells (bottom-left), and 2.8×10^7 cells with $y_1^+ < 1$ (bottom-right)

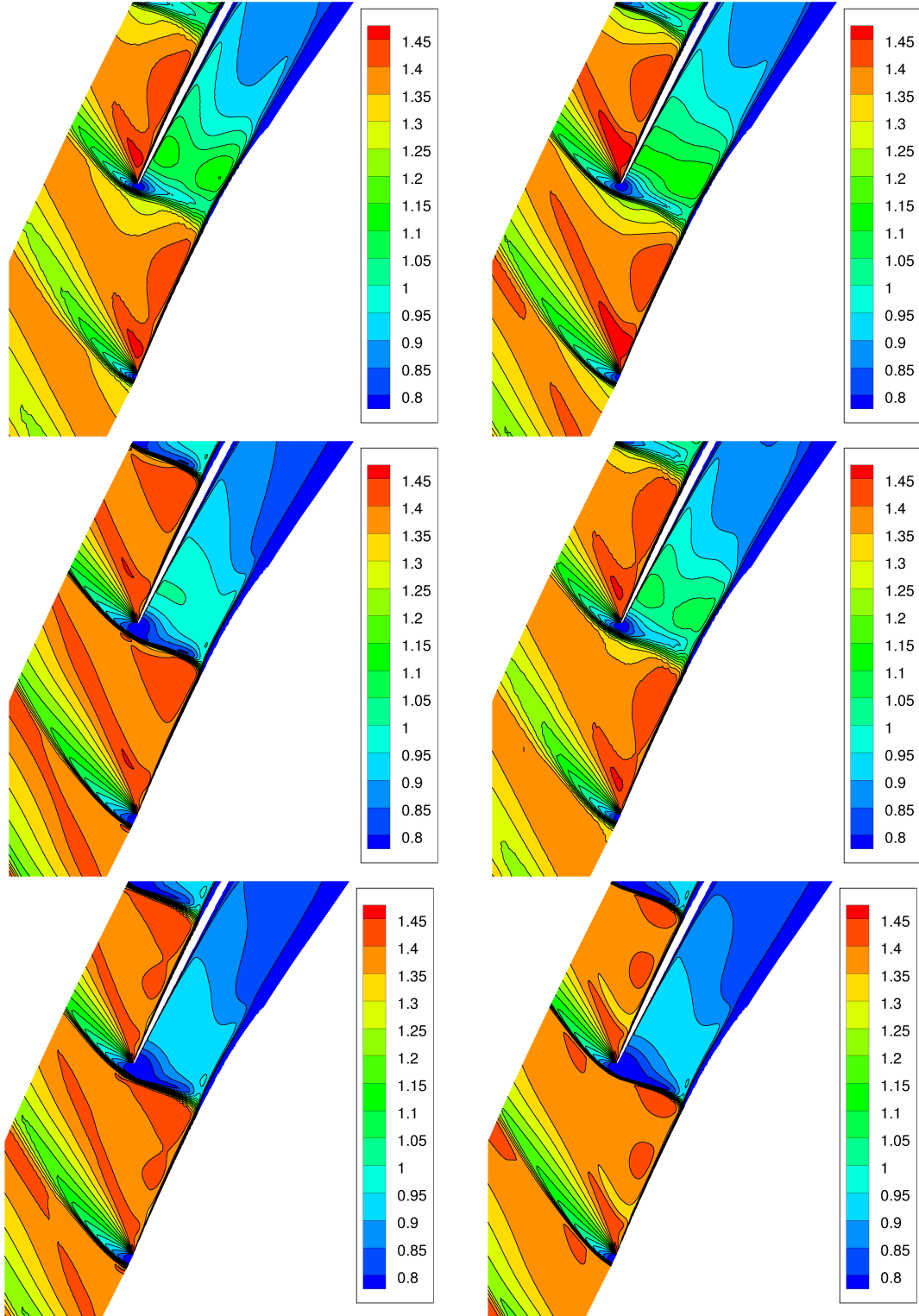


FIGURE 4.14. Contours of relative Mach number at 10% span from the shroud for the rotor alone operating near stall; 2.3×10^5 cells (top-left), 4.3×10^5 cells with $y_1^+ < 1$ (top-right), 1.9×10^6 cells (middle-left), 3.5×10^6 cells with $y_1^+ < 1$ (middle-right), 1.5×10^7 cells (bottom-left), and 2.8×10^7 cells with $y_1^+ < 1$ (bottom-right)

Additional insight into the flows may be gained through the examination of fan performance maps. Figures 4.15 – 4.16 show the isentropic efficiency and total pressure ratio across the fan, respectively, for the rotor alone operating at 100% speed. The experimental data include both the Strazisar data from 1989 (denoted by squares) [3], as well as data from follow up testing performed in 2004 and shown by Fidalgo *et al.* [2] (denoted by diamonds). All but the coarsest grid solutions yield efficiency curves falling within the spread of experimental values. Coarser grids result in lower efficiencies, with the wall spacing correlating most significantly with this result. The grid with the finest off-body mesh and a large y_1^+ had nearly identical efficiency predictions to that with the coarsest off-body mesh and small y_1^+ . Also, finer grids converged at lower mass flow rates than did coarse grids. Figure 4.16 shows that higher total pressure ratios were predicted on finer grids. The two finest grids are in excellent agreement with the experimental results.

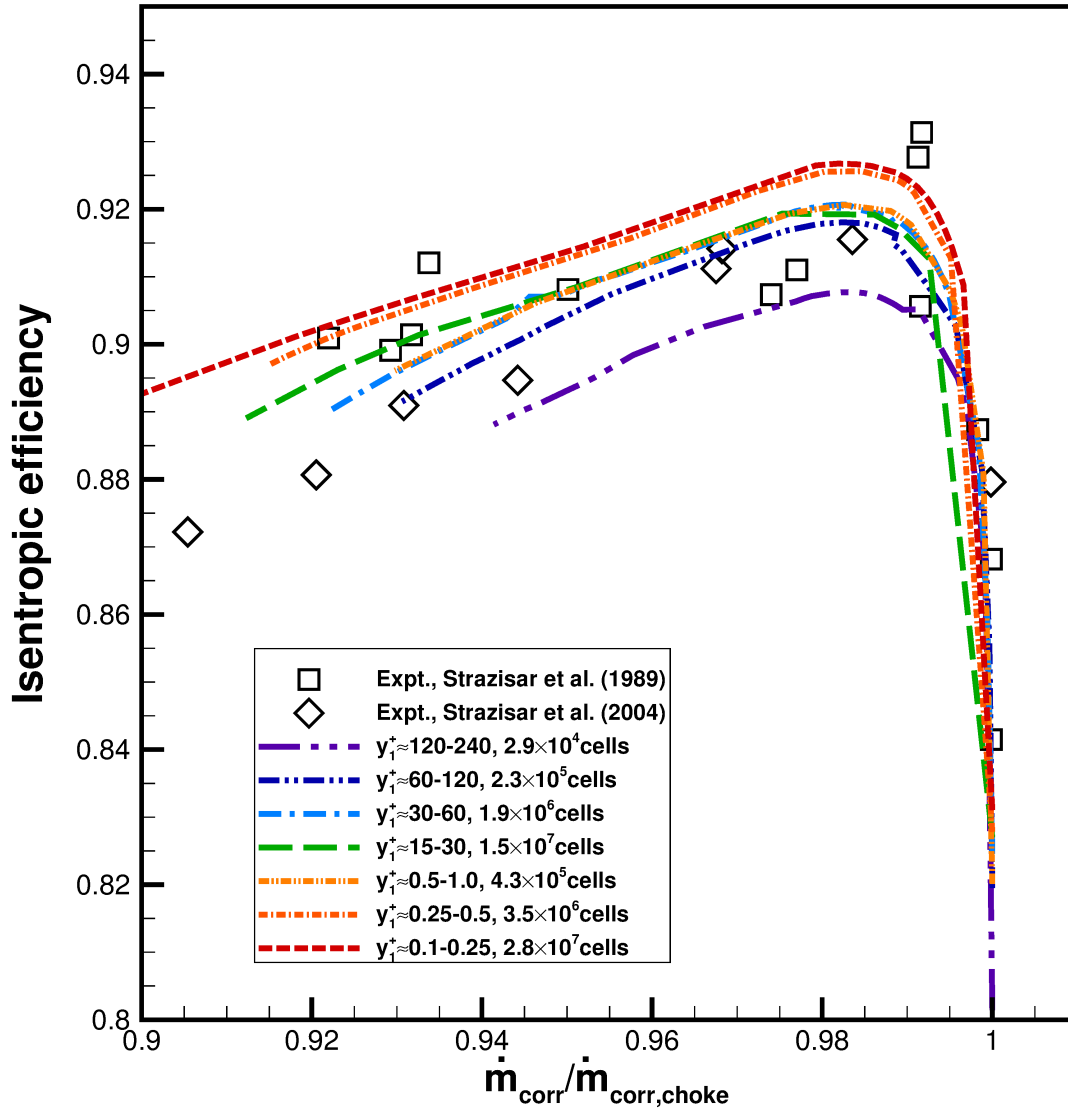


FIGURE 4.15. Isentropic efficiency for the rotor alone operating at 100% of design speed.

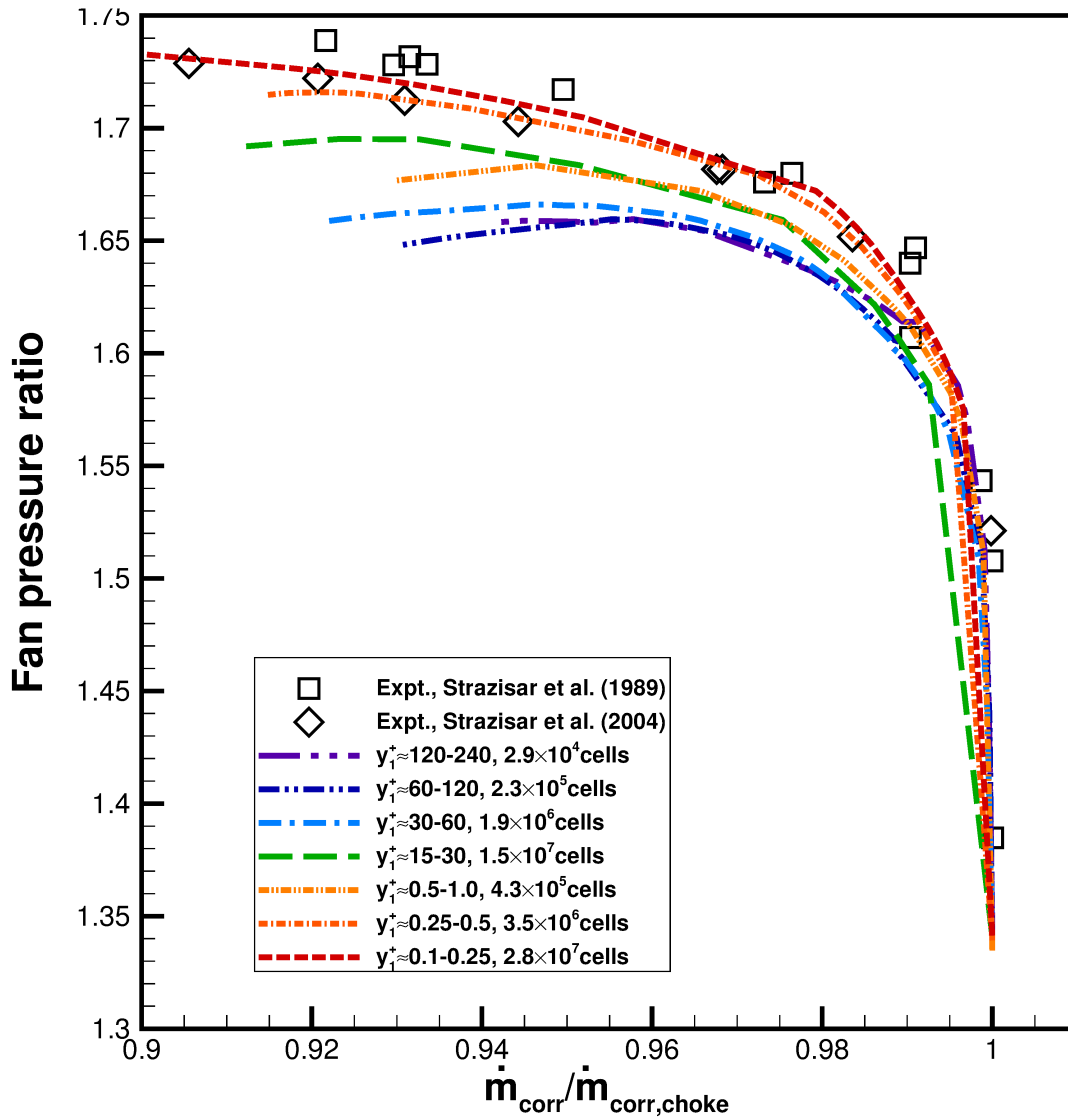


FIGURE 4.16. Total pressure for the rotor alone operating at 100% of design speed.

When comparing to experimental data, it is important to consider the method of integration used at the stations. Figures 4.17 – 4.19 compare CFD data for efficiency and total pressure ratios post-processed by using rake and slice data to experimental data. Efficiency is significantly affected by choice of integration type, while total pressure ratio is not. Slice integration results in lower efficiencies, especially for grids with large wall spacings using wall function boundary conditions. This is not surprising as the total pressure deficits found in the boundary layers at the hub and shroud are largely discounted by the rake integration technique. Differences in efficiency predictions between rake integration and slice integration are on the order of 1%, which is significant.

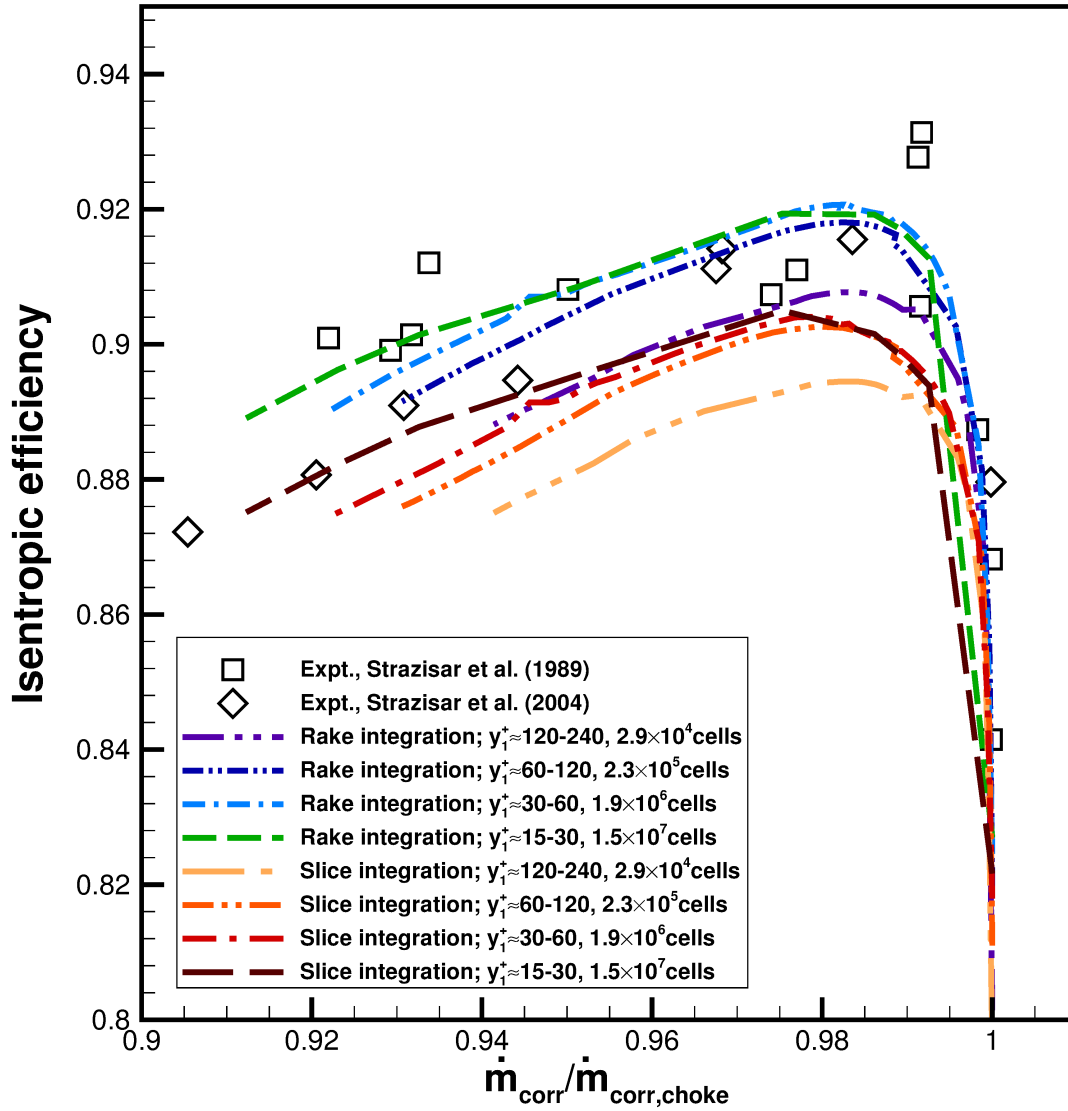


FIGURE 4.17. Total pressure for the rotor alone operating at 100% of design speed; rake integration and slice integration shown for coarse grid series.

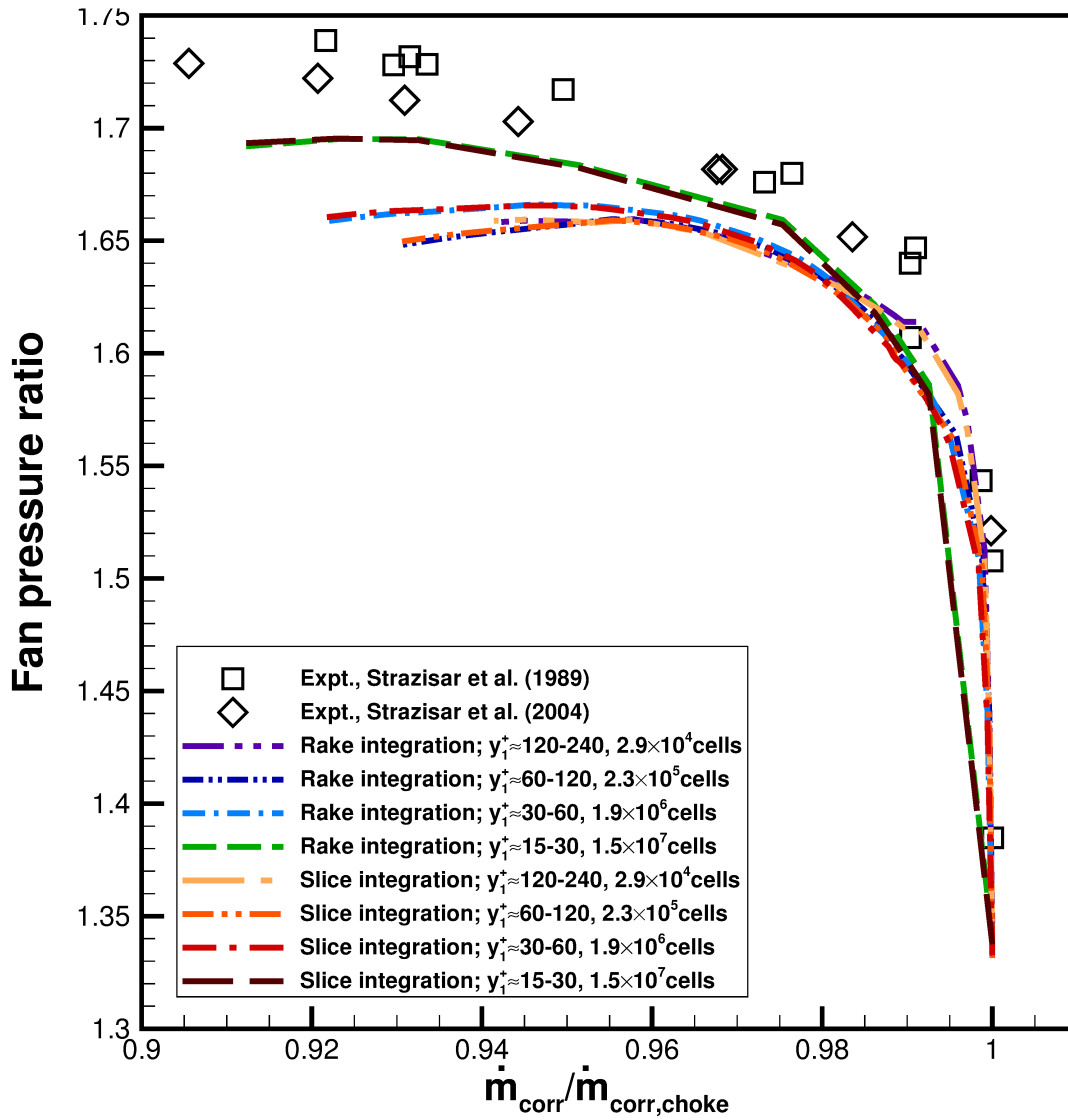


FIGURE 4.18. Total pressure for the rotor alone operating at 100% of design speed; rake integration and slice integration shown for coarse grid series.

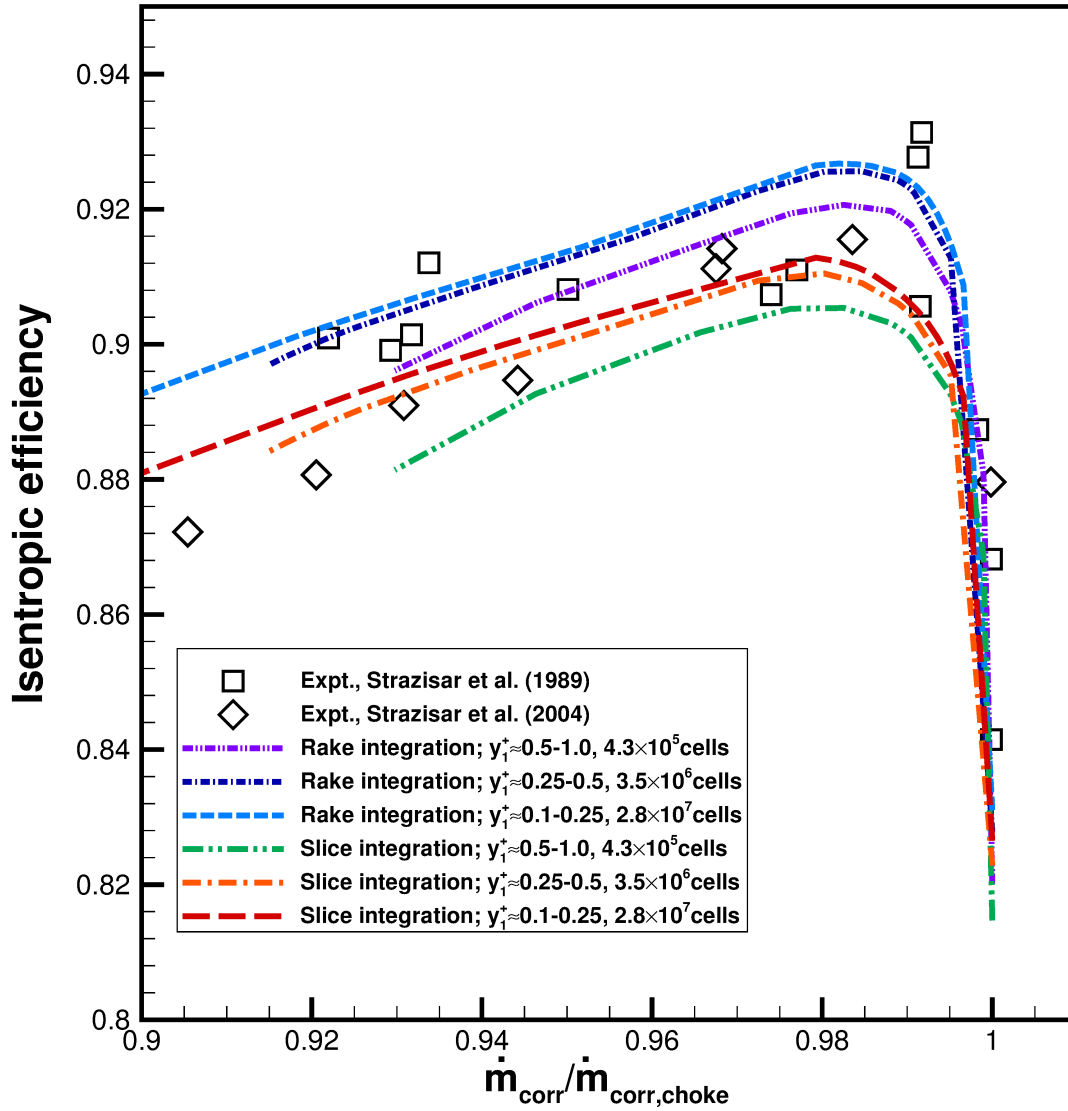


FIGURE 4.19. Total pressure for the rotor alone operating at 100% of design speed; rake integration and slice integration shown for fine grid series.

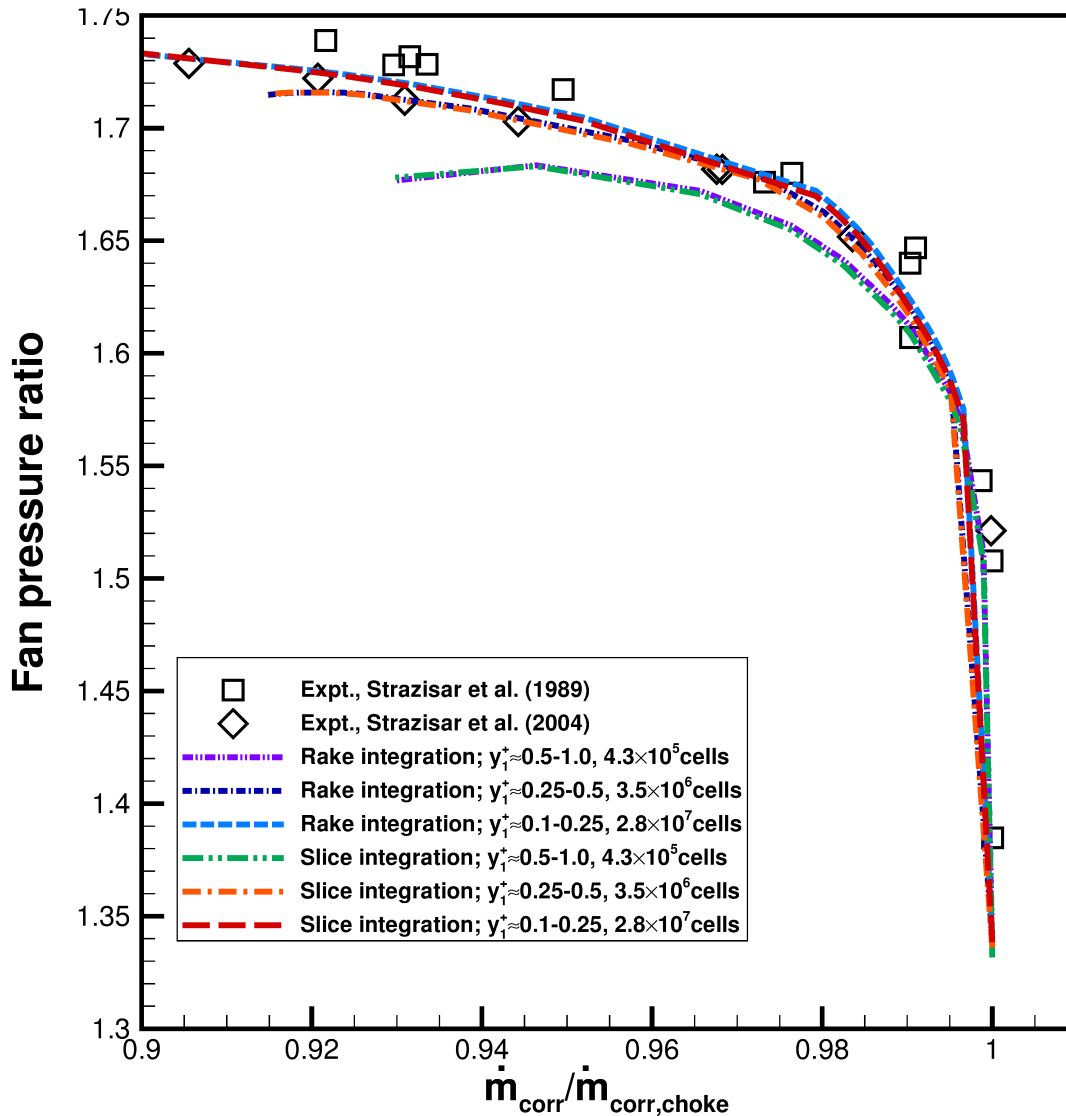


FIGURE 4.20. Total pressure for the rotor alone operating at 100% of design speed; rake integration and slice integration shown for fine grid series.

Four turbulence models including the realizable $k-\epsilon$ model, cubic $k-\epsilon$ model, Spalart-Allmaras (S-A) model, and SST model were investigated to study the effects on flow predictions. Figures 4.21 – 4.27 show comparisons of CFD solutions computed using the four turbulence models on an identical grid. The grid consisted of 2.3×10^5 cells with $60 < y_1^+ < 120$. Wall-functions were employed for all of the cases investigated. Not all models converged near

the stall condition as depicted in Figures 4.26 – 4.27. Therefore, detailed comparisons of the flow are only done for an operating condition near peak efficiency.

Figure 4.21 shows relative Mach number along a line of constant 50% pitch, at 10% span from the shroud, for an operating point near peak efficiency. The SST model predicts the shock location to be further downstream than the other models. The cubic $k-\epsilon$ model predicts the shock location farthest upstream, which agrees closest with the experimental data. The SST model also predicts higher relative Mach number exiting the blade passage than the other models. Predictions from the realizable $k-\epsilon$ and S-A models are almost identical to each other.

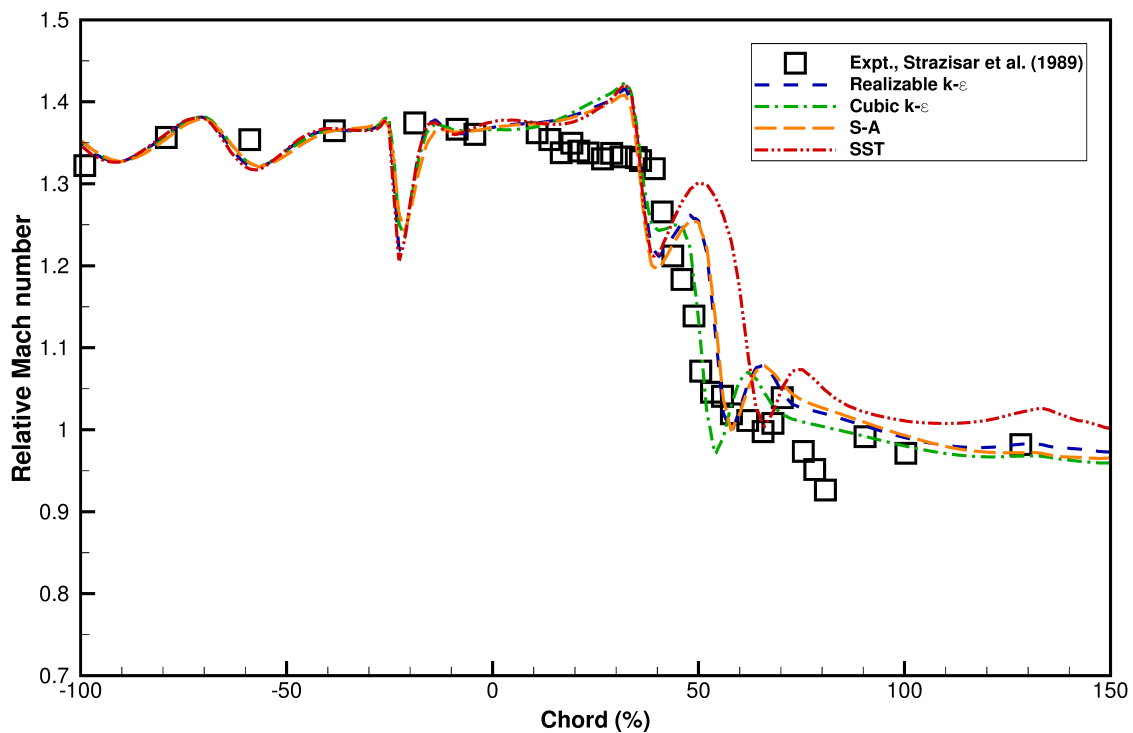


FIGURE 4.21. Relative Mach number at 10% span from the shroud and at 50% pitch, for the rotor alone operating near peak efficiency with four turbulence models.

Figure 4.22 shows similar differences between the SST model and the other models as those observed in Figure 4.21. The shock location predicted by the SST model is downstream

of that predicted by other models. The SST model also predicts a higher relative Mach number for the flow exiting the blade row.

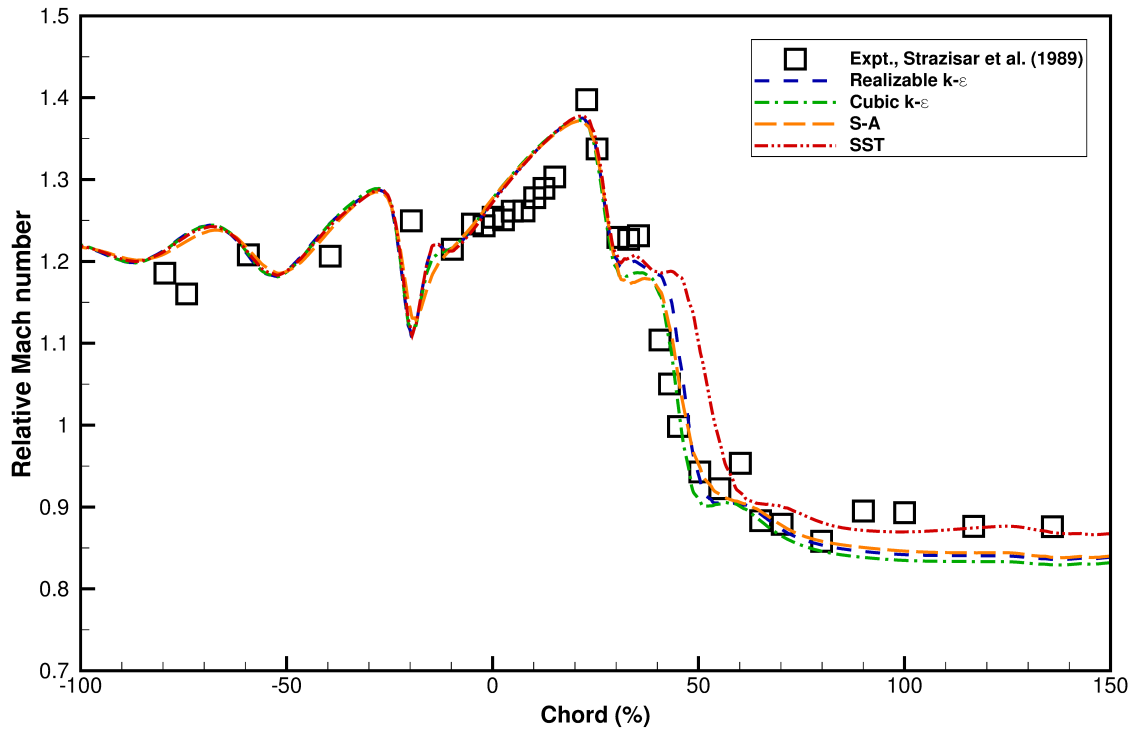


FIGURE 4.22. Relative Mach number at 30% span from the shroud and at 50% pitch, for the rotor alone operating near peak efficiency with four turbulence models.

The differences in predictions near 50% chord, by all turbulence models, decrease at span locations closer to the hub. Figure 4.23 shows that the SST model predicts greater flow acceleration immediately after the shock at 70% span from the shroud. The S-A model predicts slightly lower maximum relative Mach number at the upstream edge of the shock compared to the other models.

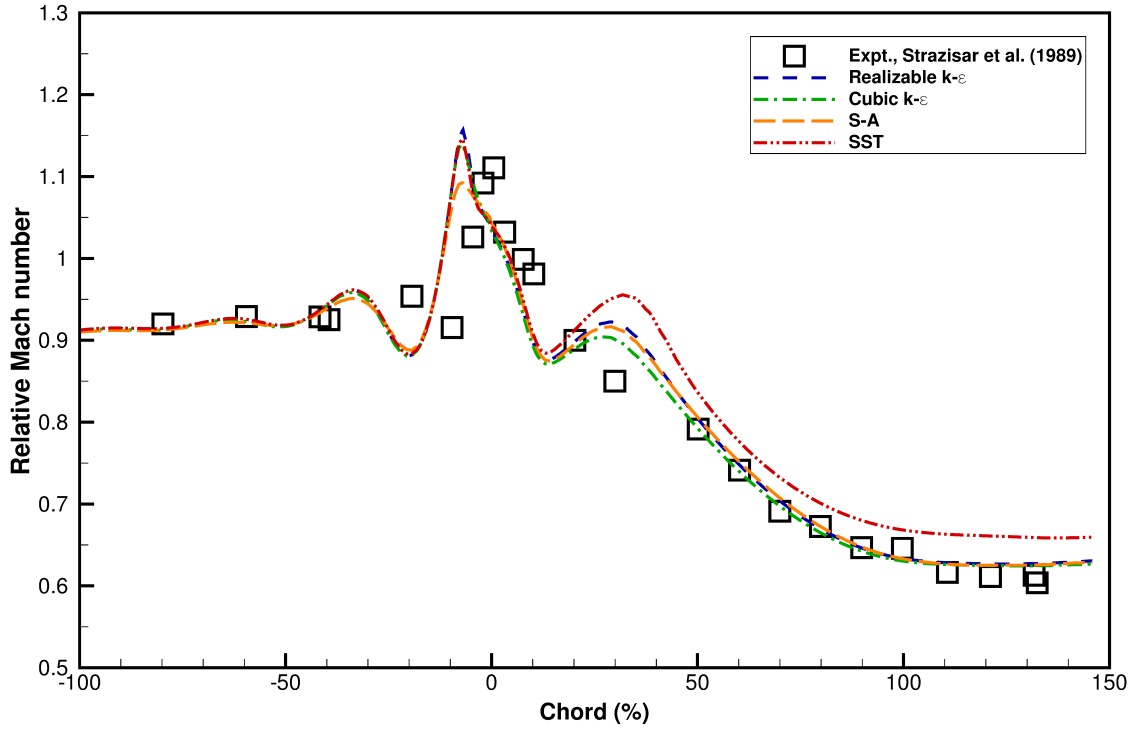


FIGURE 4.23. Relative Mach number at 70% span from the shroud and at 50% pitch, for the rotor alone operating near peak efficiency with four turbulence models.

Figure 4.24 presents radial profiles of total pressure, total temperature, static pressure, and flow angle. Predictions attained with the SST model are again significantly different than those from other models, with all quantities being underpredicted, especially near the tip region. Other models yield very similar predictions to each other.

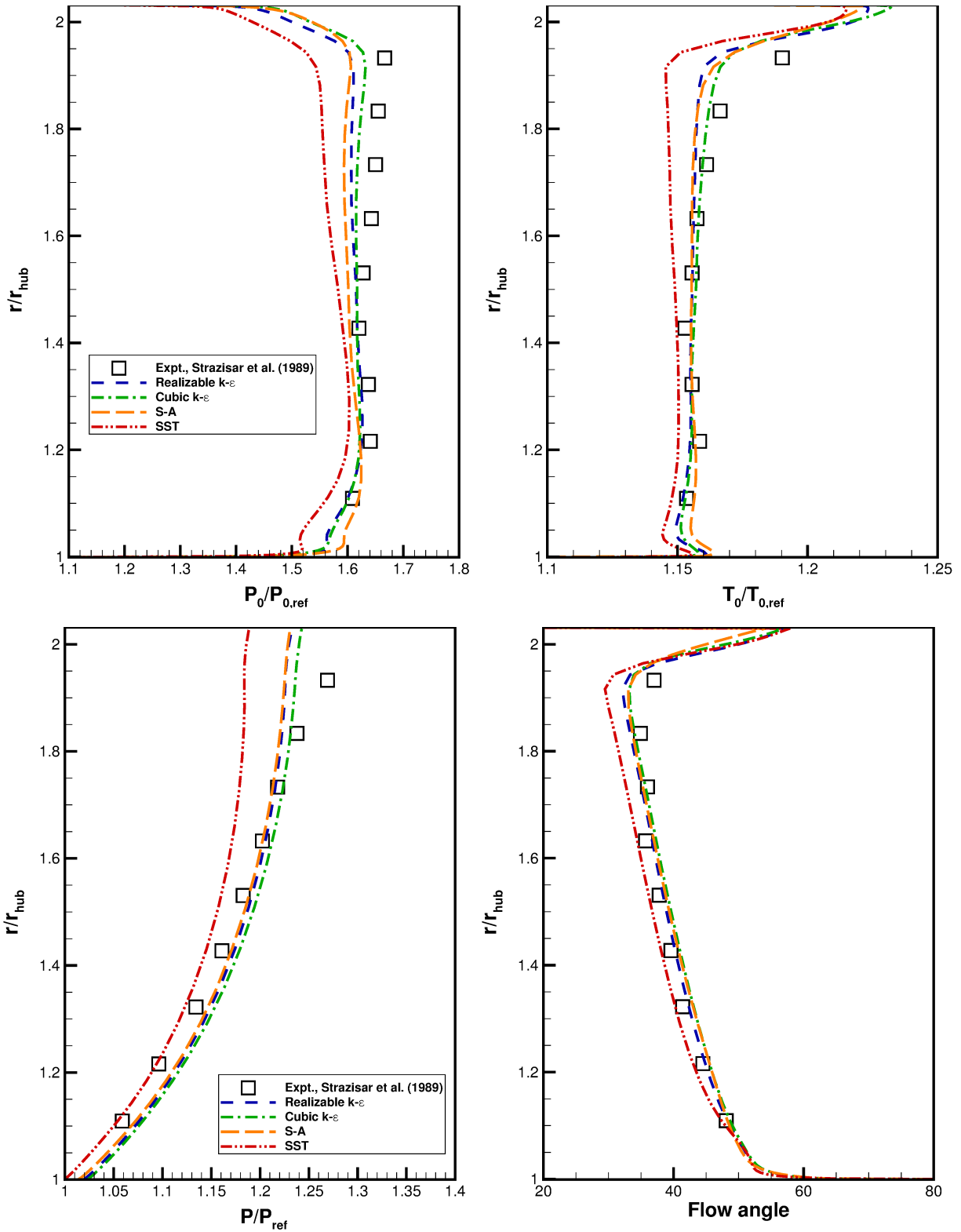


FIGURE 4.24. Spanwise distributions of total pressure (top-left), total temperature (top-right), static pressure (bottom-left), and exit flow angle (bottom-right) for the rotor alone operating near peak efficiency with four turbulence models.

Contours of relative Mach number at 10% span from the shroud, as shown in Figure 4.25, clearly show the trends observed in Figure 4.21. The location of the passage shock predicted with the cubic $k-\epsilon$ model is upstream of the other models, while that predicted with the SST models is much further downstream. The relative Mach number of flow exiting the blade passage is higher in the contour predicted with the SST model. Flow upstream of the leading edge shock appears to be unaffected by the choice of turbulence models.

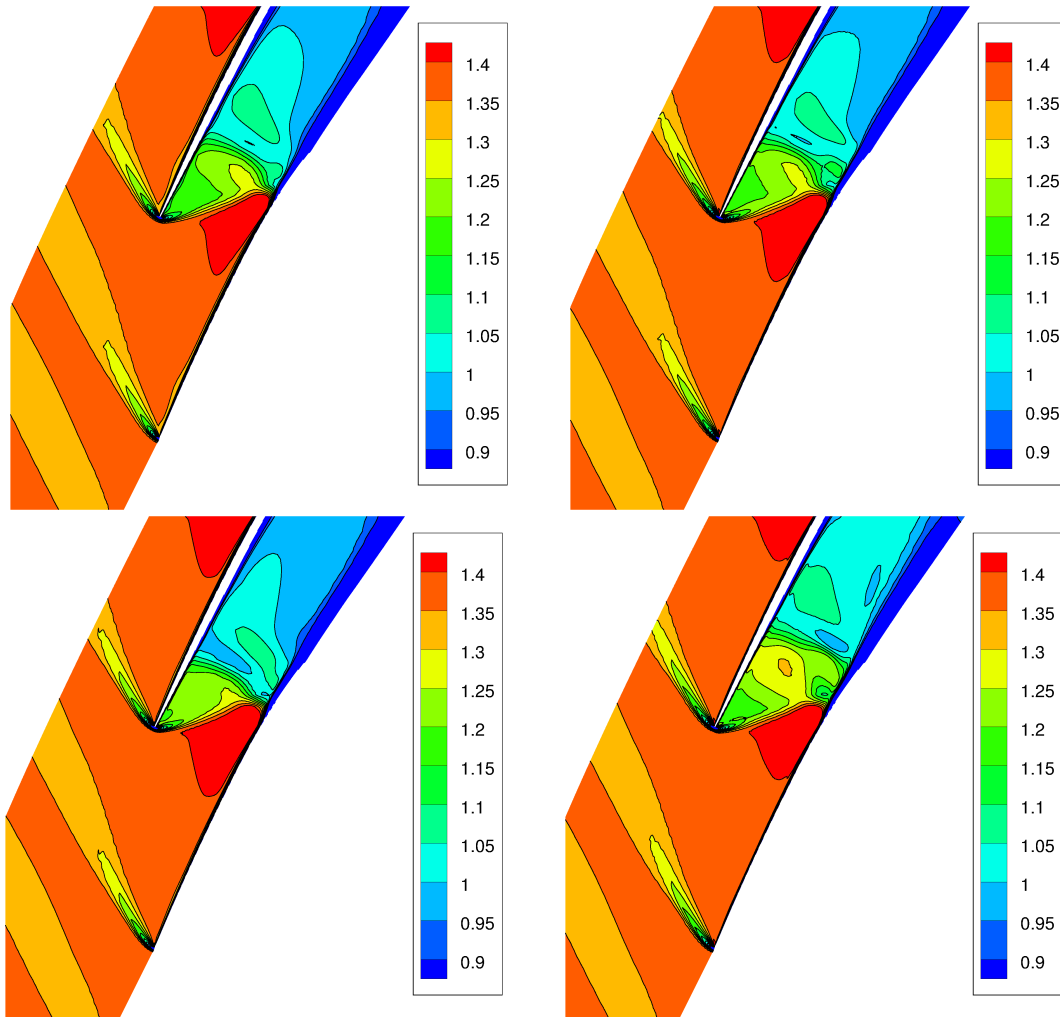


FIGURE 4.25. Contours of relative Mach number at 10% span from the shroud for the rotor alone operating at peak efficiency; 2.3×10^5 cells; S-A model (top-left), $k-\epsilon$ model (top-right), cubic $k-\epsilon$ model (bottom-left), and SST model (bottom-right).

Figure 4.26 shows isentropic efficiency as computed using each of the four turbulence models. The choice of turbulence model has a significant effect on the predicted efficiency. The S-A model predicts the lowest peak efficiency while the SST model predicts the highest, but at a lower mass flow rate than the predictions by the other models and the experimental data. Not all models converged to the near-stall condition. The cubic k - ϵ model converged to the lowest mass flow rate, while the SST model failed to converge at comparatively high mass flow rates.

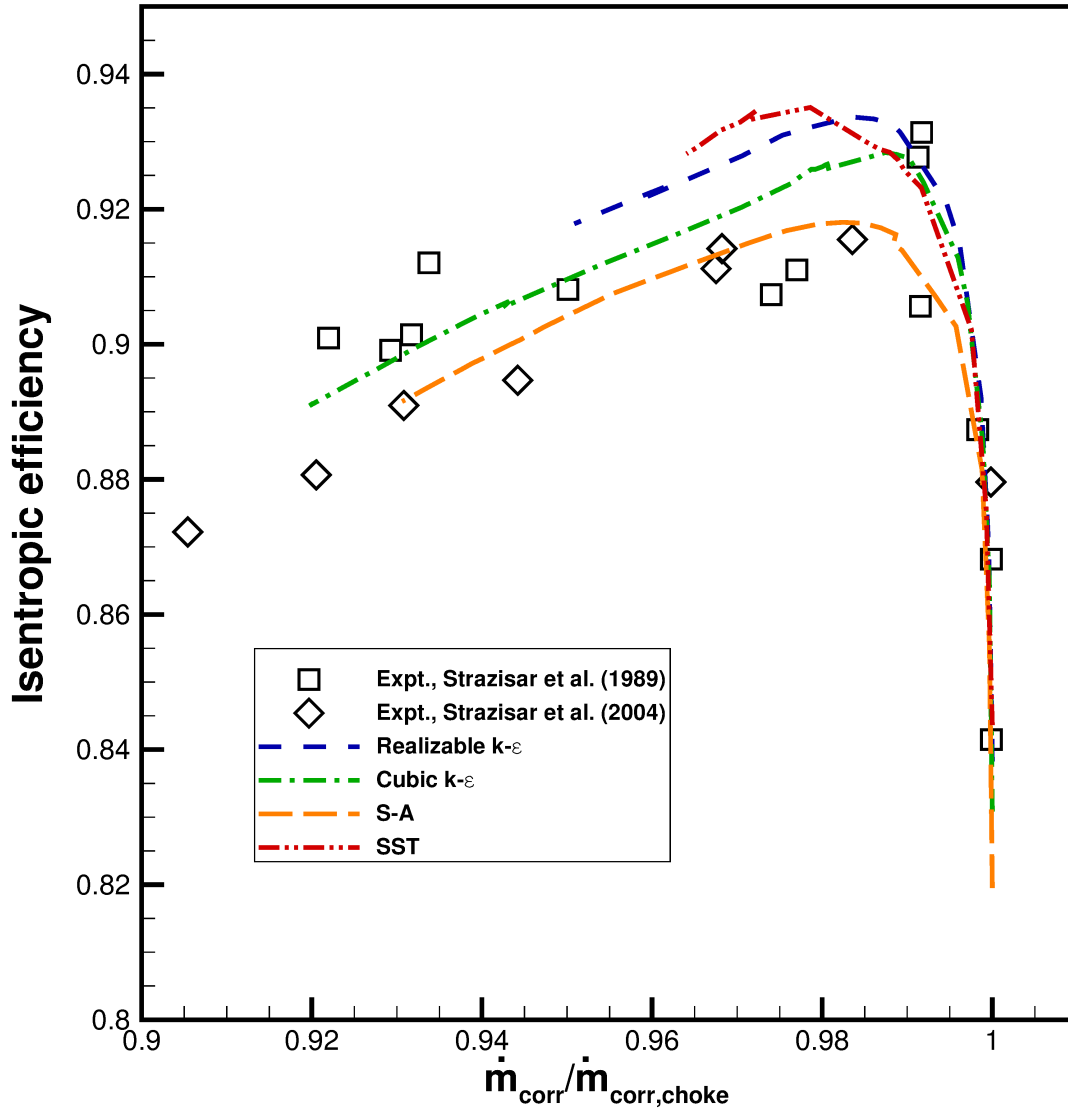


FIGURE 4.26. Isentropic efficiency for the rotor alone simulated with four turbulence models.

Figure 4.27 shows the total pressure ratio across the fan operating at a point near peak efficiency. The cubic $k-\epsilon$ model predicts the highest total pressure ratio, matching the experimental values most closely. The SST model significantly underpredicts the total pressure ratio.

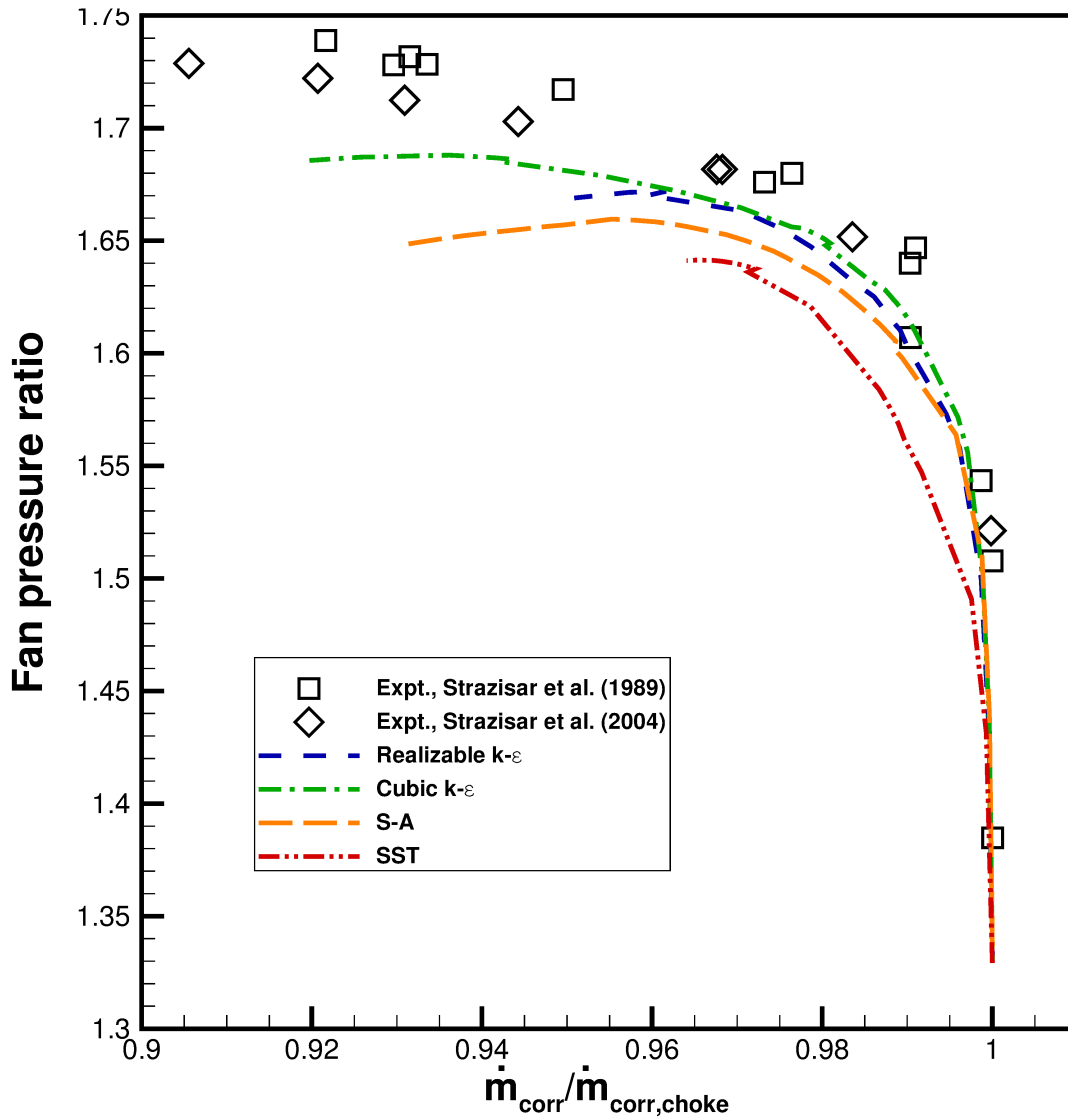


FIGURE 4.27. Total pressure ratio for the rotor alone operating near peak efficiency with four turbulence models.

4.1.2. ROTOR-ALONE WITH CENTER-BODY. The inclusion of the spinning center-body geometry depicted in Figure 2.4 results in slightly lower isentropic efficiencies, as shown in Figure 4.28. The difference between the solution obtained for this geometry and that for the rotor-alone geometry is approximately 0.5% and is consistent across all grids. Cases on a fine grid did not converge to a mass flow rate as near to the stall point when the center-body

was included. This trend is inconsistent with results of the grid dependence study for the rotor-alone case.

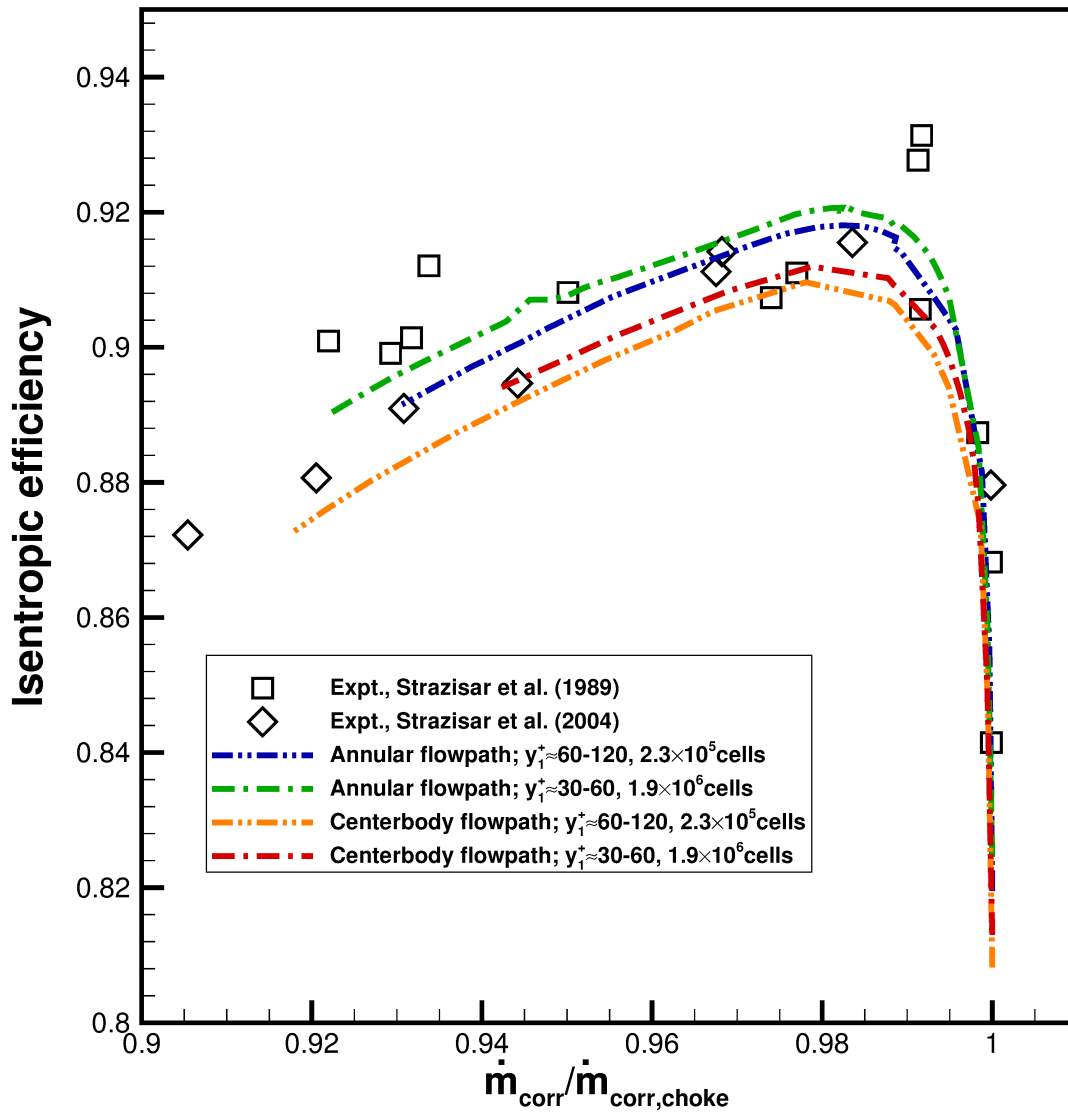


FIGURE 4.28. Isentropic efficiency for the rotor alone, with annular and center-body flowpaths, operating at 100% of design speed.

The center-body geometry appears to have less of an effect on total pressure ratio than efficiency, as indicated by Figure 4.29. The difference is more significant on the fine grid than on the coarse grid.

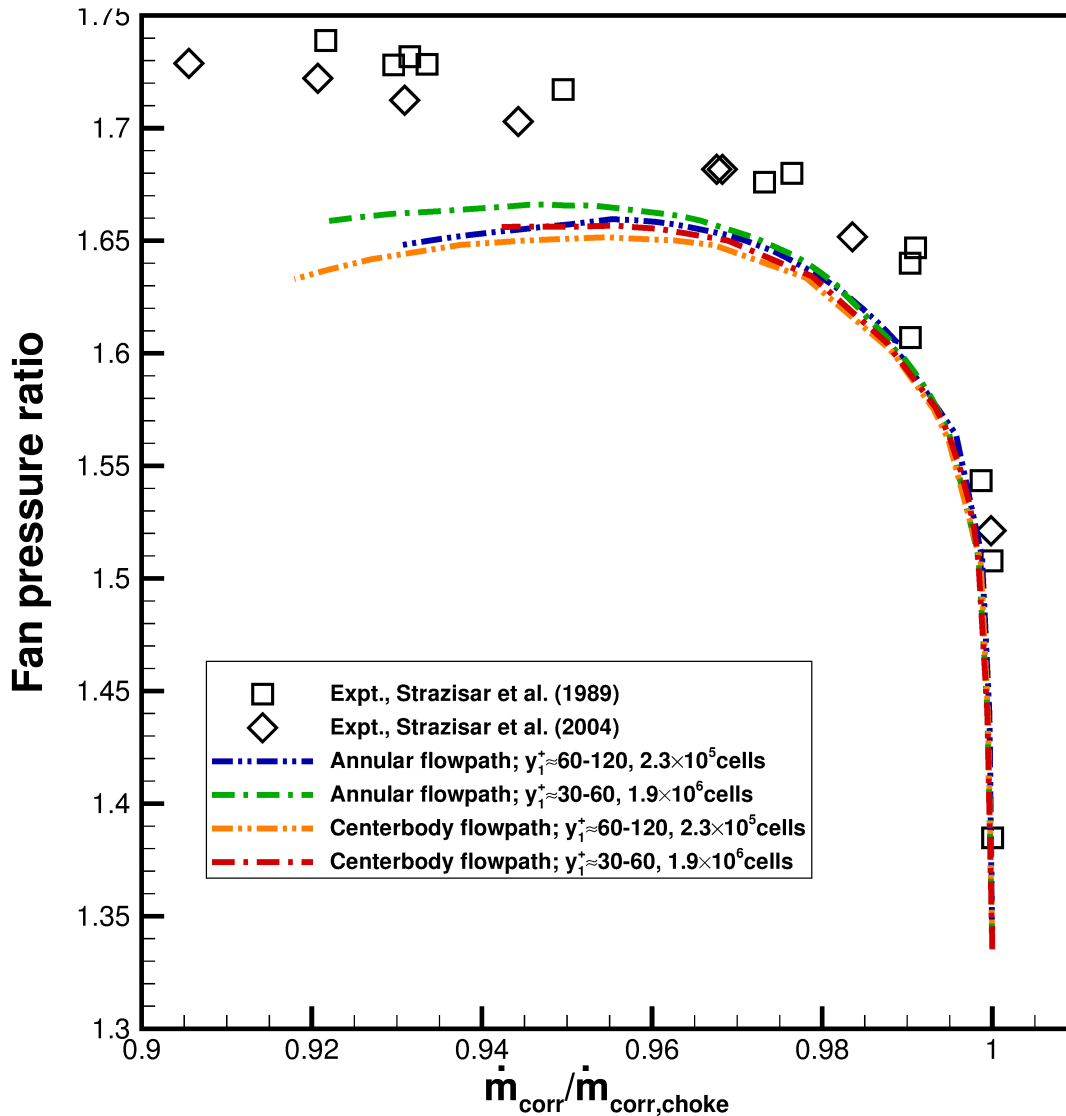


FIGURE 4.29. Total pressure for the rotor alone, with annular and centerbody flowpaths, operating at 100% of design speed.

Figure 4.30 shows the predicted isentropic efficiency of the rotor alone with the center-body geometry, at 60%, 70%, 80%, 90% and 100% speeds. The CFD result underpredicts the efficiency at lower speeds. None of the cases converged to the experimentally measured stall condition. This is likely due to the lack of resolution in the tip-clearance region where stall inception typically occurs.

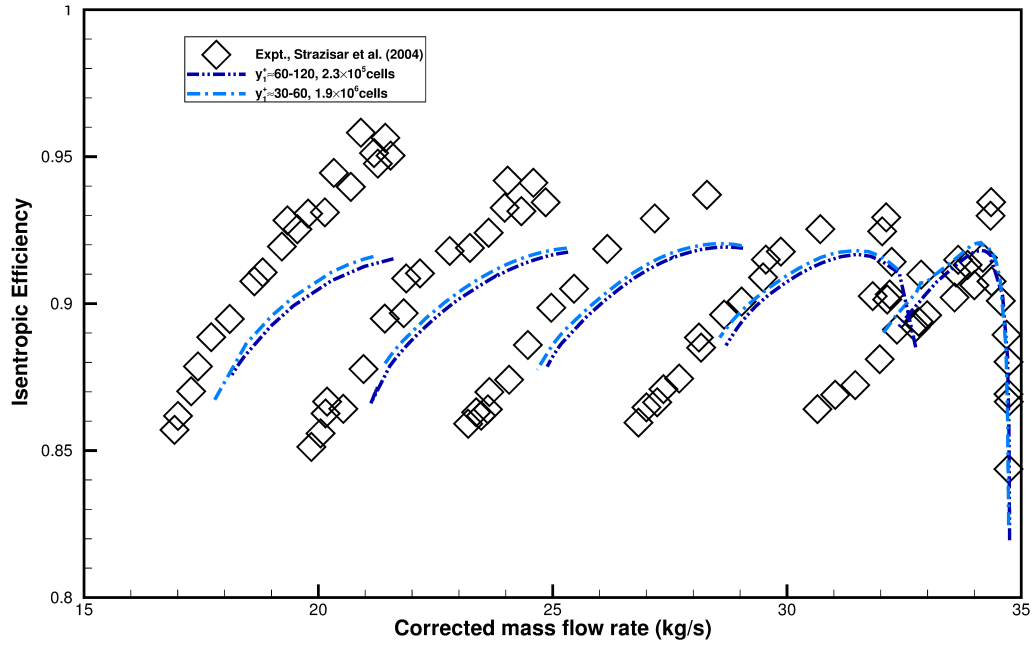


FIGURE 4.30. Isentropic efficiency for the rotor alone, with center-body flow-path, operating at 60%, 70%, 80%, 90% and 100% of design speed, from left to right.

The total pressure ratios of the CFD predictions agree well with the experimental data at lower speeds (such as 60% – 80% of design speed), but are underpredicted at higher speeds as shown in Figure 4.31. The dependence upon grid resolution appears to be less at lower fan speeds than at higher fan speeds.

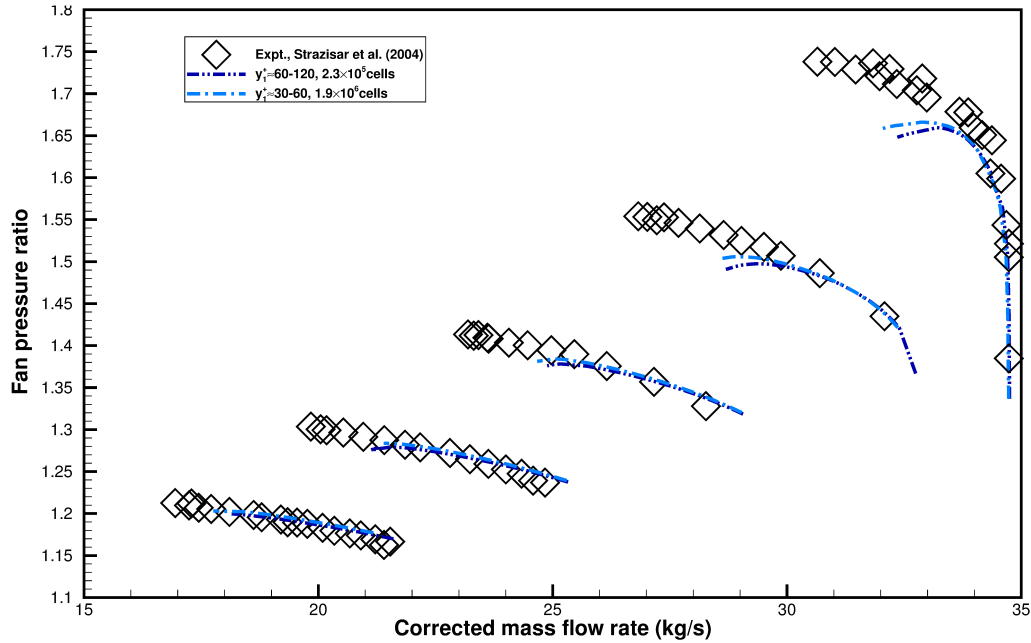


FIGURE 4.31. Total pressure ratio for the rotor alone, with center-body flow-path, operating at 60%, 70%, 80%, 90% and 100% of design speed.

4.1.3. STAGE WITH CENTER BODY. CFD predictions of the stage performance are compared with experimental data in Figures 4.32 – 4.33. It is worth noting that the location of the data collected downstream of the stator in the experiment is unknown, and likely does not match that used for the CFD results. For the predicted performance data, stagnation quantities were averaged at the trailing edge of the stator. The location in the experimental setup was likely further downstream. This could result in higher efficiencies being calculated for CFD results. However, another factor affecting the calculation of efficiency is the choice of integration (rake or slice). While the experimental results would necessarily use rake integration, the CFD results were post-processed using slice integration. This method was used because of the unavailability of rake probe locations used for experimental measurements. Therefore, uncertainties exist which may result in significant (but possibly offsetting) errors in the comparison of stage efficiency between CFD and experimental data. Figure 4.32 shows experimental data at 70% speed (blue), 80% speed (green), 90% speed (orange), and 100%

speed (red). The CFD predictions agree reasonably well with the experimental data, especially at 100% of the design speed. Similarly to the rotor-alone cases, converged solutions were not obtained near the experimentally determined stall point.

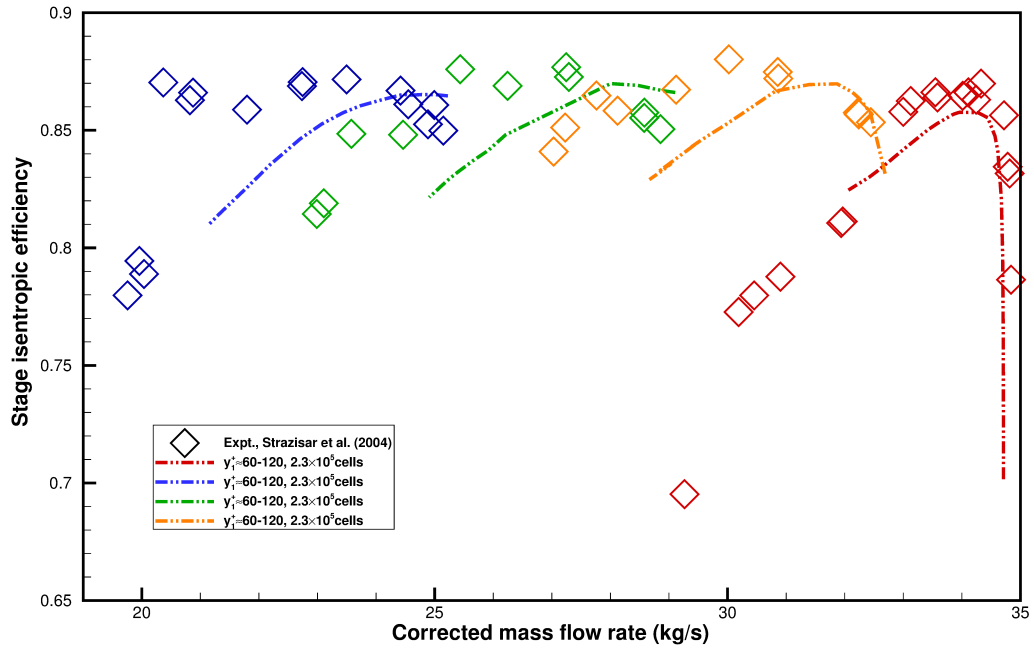


FIGURE 4.32. Isentropic efficiency for the stage operating at 70%, 80%, 90% and 100% of design speed.

The CFD and experimental results are in reasonable agreement for the stage's total pressure ratio, as seen in Figure 4.33.

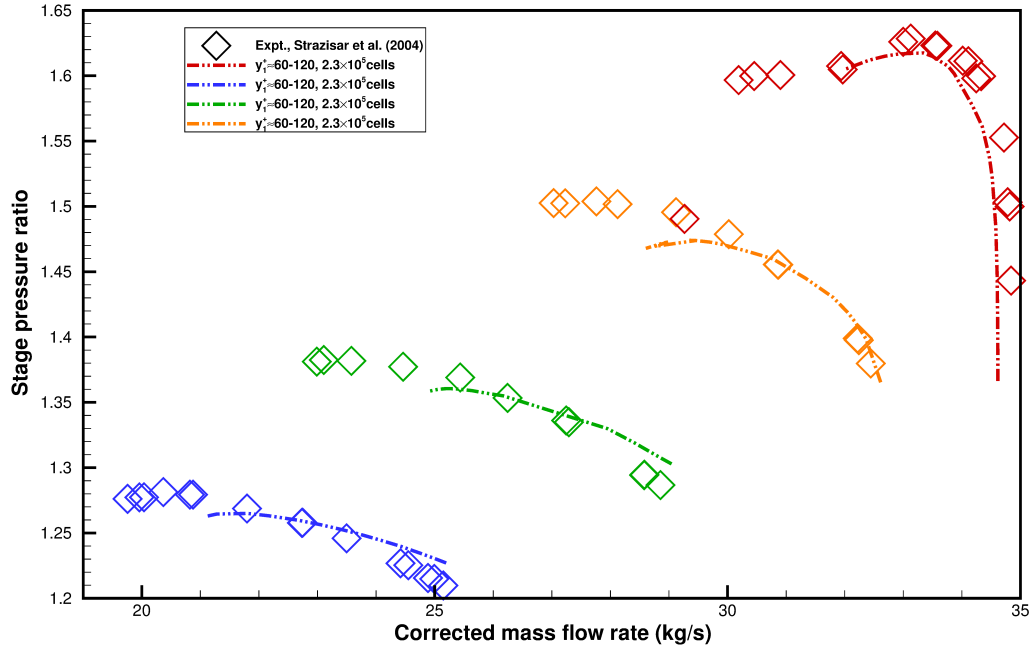


FIGURE 4.33. Total pressure ratio for the stage operating at 70%, 80%, 90% and 100% of design speed.

4.1.4. STAGE WITH CENTER BODY, NACELLE, AND NOZZLE. The complete geometry, as shown in Figure 2.4, includes the rotor-stator stage, spinning center-body, nacelle, and nozzle. For the complete fan system, operating lines at relevant conditions are of interest. Three operating conditions are investigated; static, take-off, and cruise conditions as defined in Section 3.6. Figure 4.34 plots the rotor isentropic efficiency versus the corrected mass flow rate. In the figure, the blue, green, and red lines are operating lines for the static, take-off, and cruise condition, respectively. The black line corresponds to the operating line of the rotor-alone geometry. Along each solid line, the symbols represent steady-state operating points, which are determined by the nozzle. Nine nozzle geometries were used, each with a unique exit area, as seen in Figures 2.2 – 2.3. Each operating point along the operating lines corresponds to a different nozzle geometry. For the static condition, only seven nozzles provided steady-state solutions, with solution for the other two geometries diverging. For the take-off condition, the solution on one nozzle failed to converge. Converged solutions

were achieved for all nine nozzle geometries at the cruise condition. On each operating line, a single, larger symbol with a black border is shown. These indicate solutions obtained on the nozzle geometry used for later URANS simulations.

The large, bordered symbols indicate that as the freestream Mach number increases, the mass flow rate for a given geometry increases as well. The efficiency at the cruise condition closely matches that obtained with rotor alone simulations. The efficiency at the take-off condition is the highest at all operating points, and the efficiency at the static condition is bounded by the cruise and take-off conditions. A similar mass flow rate near stall was obtained, at each condition, albeit for different nozzle geometries. The minimum mass flow rate for all conditions was around 30 kg/s . The maximum difference in efficiency between the static, take-off, and cruise conditions is approximately 1%.

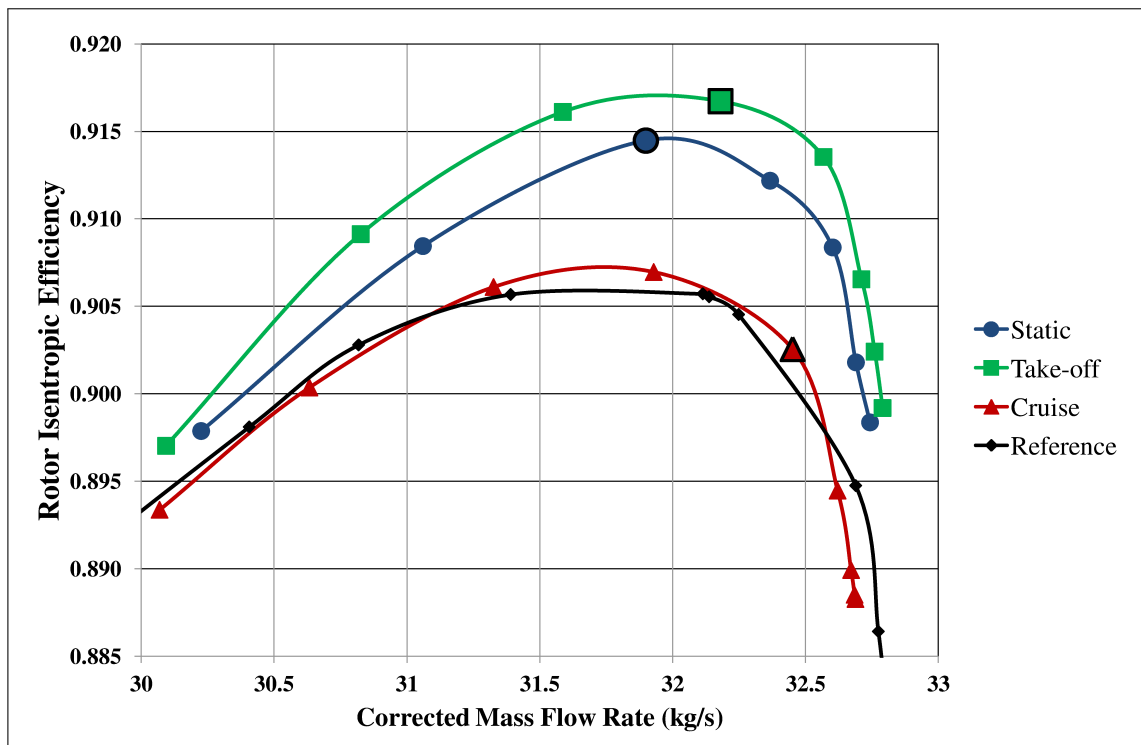


FIGURE 4.34. Isentropic efficiency ratio across the rotor for stage with nacelle and nozzle at static, take-off and cruise conditions. Reference isentropic efficiency is from rotor-alone simulation.

Figure 4.35 shows the total pressure ratio of the stage. The static and take-off condition have total pressure ratio lines that closely follow the reference line, while the total pressure ratio at the cruise condition is lower than the others. However, all the pressure ratio lines behave qualitatively with a consistent trend.

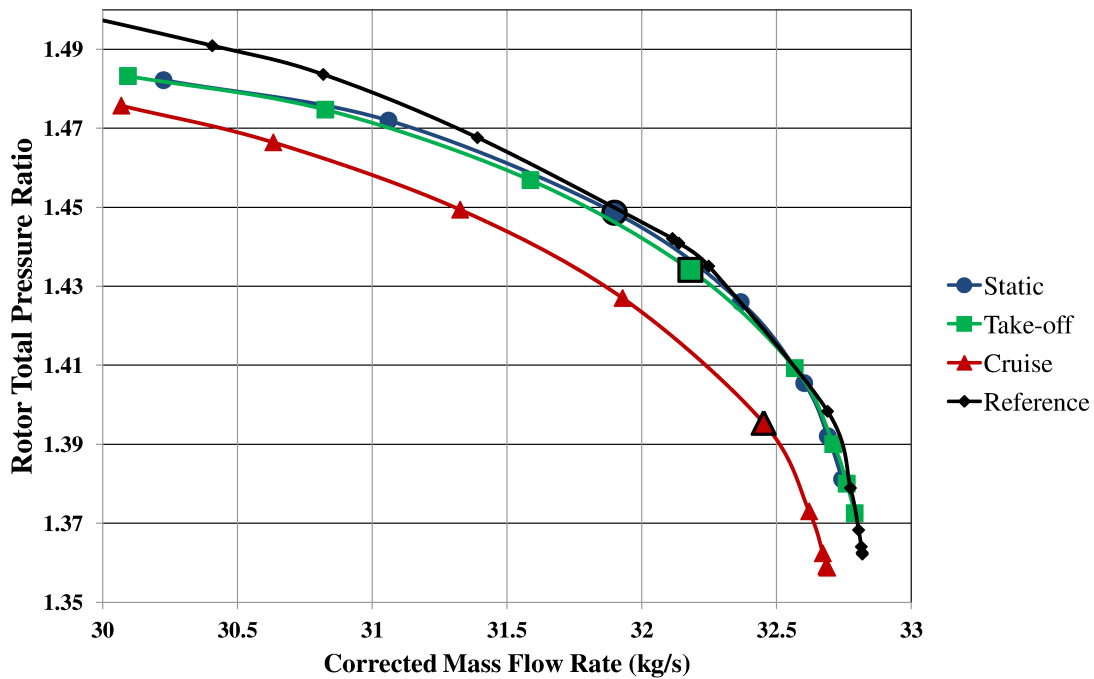


FIGURE 4.35. Total pressure ratio across the rotor for stage with nacelle and nozzle at static, take-off and cruise conditions. Reference total pressure ratio is from rotor-alone simulation.

4.2. 3D FULL ANNULUS

4.2.1. STAGE WITH CENTER BODY. Full-annulus simulations results, for the stage with center-body geometry shown in Figure 2.4, are presented in Figures 4.36 – 4.45. The total pressure distortion at the domain’s inlet is described in Section 3.6 and identical to those observed in Figure 1.2. In Figure 4.36, the inlet total pressure and the total pressure distortion at approximately two rotor chords upstream of the rotor’s leading edge are shown. As the flow nears the fan, the initial total pressure distortion results in a decrease in static pressure

in the distorted region. Consequently, the flow is driven toward the distorted region from the clean region. This causes changes in the absolute flow angle, especially near the spinner. Figure 4.37 plots the absolute whirl angle for the z -plane which is about two chord lengths upstream of the rotor. Additionally, radial flow results from the static pressure heterogeneity near the rotor inlet. This outward radial flow is strongest at the hub and is apparent from the meridional flow angle shown in Figure 4.37.

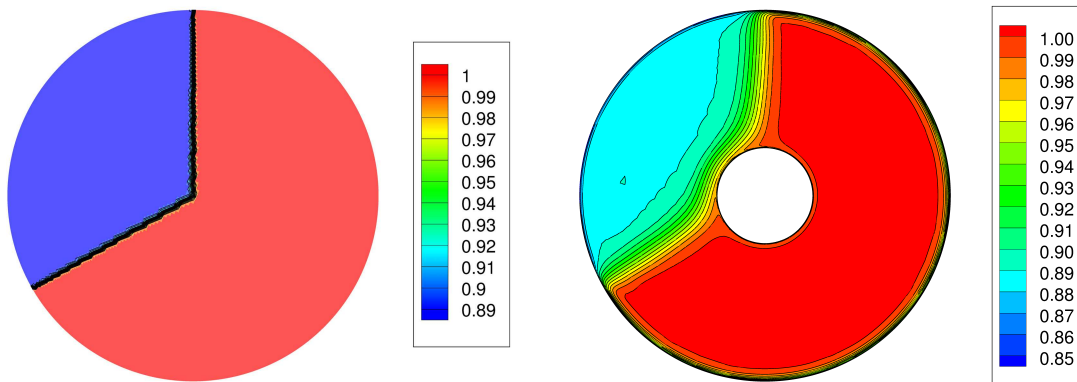


FIGURE 4.36. Total pressure at inlet (left) and at approximately 2 chords upstream of the rotor (right).

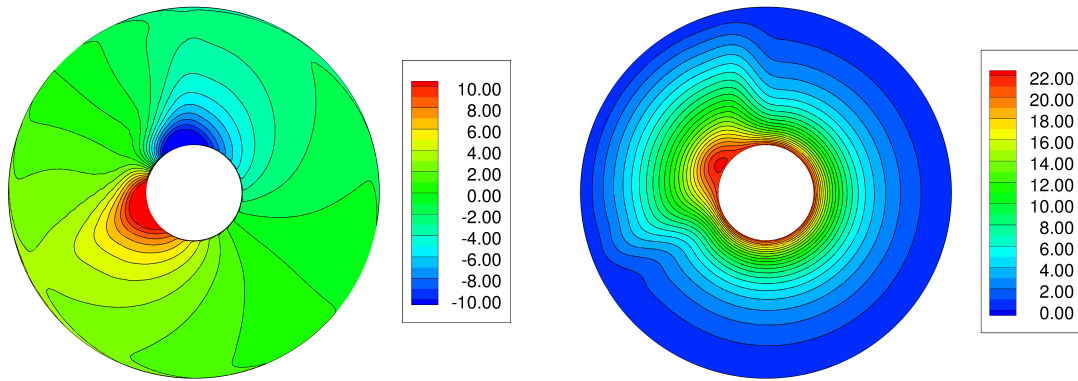


FIGURE 4.37. Contours of absolute whirl angle in degrees (left) and meridional flow angle in degrees (right) at a station approximately 2 chord lengths upstream of the rotor.

At the leading edge of the rotor, the co-swirl and counter-swirl caused by the distortion are still significant, as shown in Figure 4.38. The flow entering the fan has a circumferential velocity, so the angle of incidence on each blade is different, resulting in different local aerodynamic performances of the blades. This is further compounded by non-uniformities in mass flow, as shown in Figure 4.38. The differences in incoming mass flow rates and flow angles cause the work done by the rotor to vary significantly around the annulus.

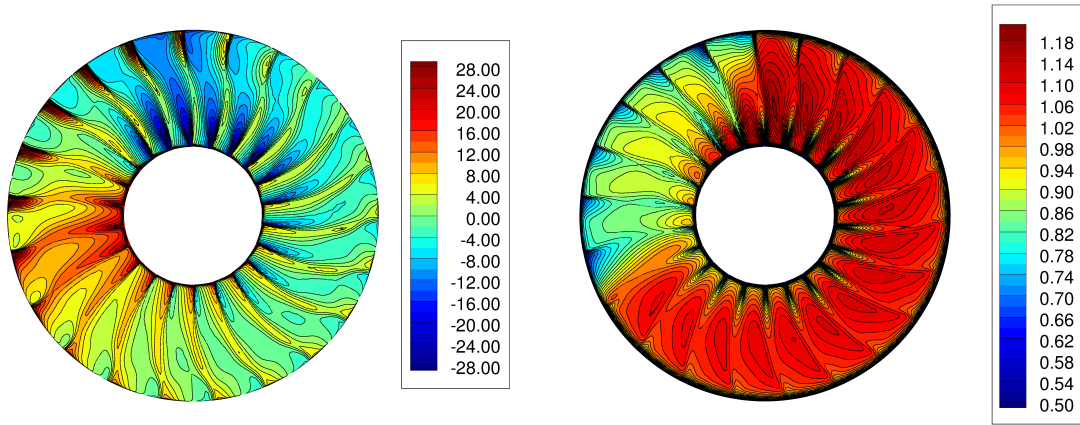


FIGURE 4.38. Absolute whirl angle (left) and mass flux distribution $\left(\frac{\rho U}{\rho U_{\text{inlet, clean}}}\right)$ (right) at the leading edge of the rotor.

The effect of the inlet incidence angle can be seen in the total pressure and total temperature contours downstream of the rotor and stator. Figures 4.39 – 4.40 show the total pressure and total temperature contours downstream of the rotor, respectively. The quantities are plotted based on two averaging approaches: time-averaging and time-pitch-averaging. The latter provides smoother contours than the former. In the co-swirl region at the rotor inlet, less work is done on the flow by the rotor. Therefore, lower total pressure and temperature are observed downstream of the rotor in this region. The converse is true for the counter-swirl region. Static pressure non-uniformities can be seen downstream of the rotor in Figure 4.40. From Figures 4.41 – 4.42, it is evident that the differences in total pressure and total temperature are convected through the stator. Downstream of the stator, the absolute whirl angles are generally diminished since the stator deswirls the flow. However, separated regions on the stator blades, near the shroud, result in high absolute whirl angle in this region, as seen in Figure 4.42.

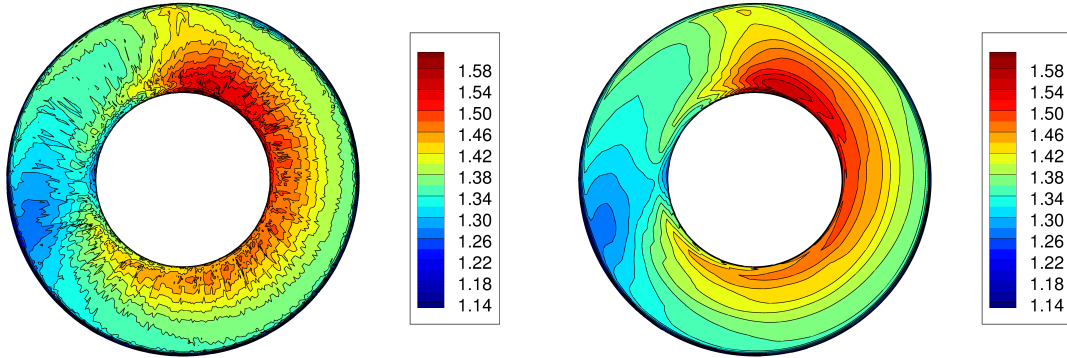


FIGURE 4.39. Total pressure downstream of rotor for time-averaged solution (left) and time-pitch-averaged solution (right).

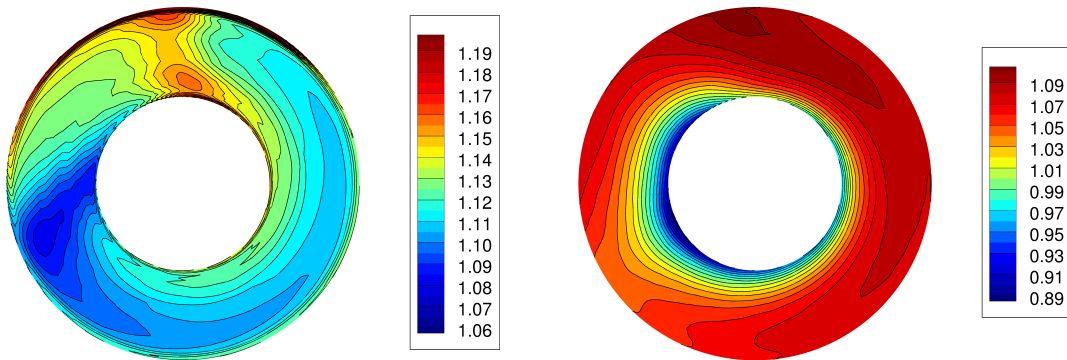


FIGURE 4.40. Total temperature (left) and static pressure (right) downstream of rotor for time-pitch-averaged solution.

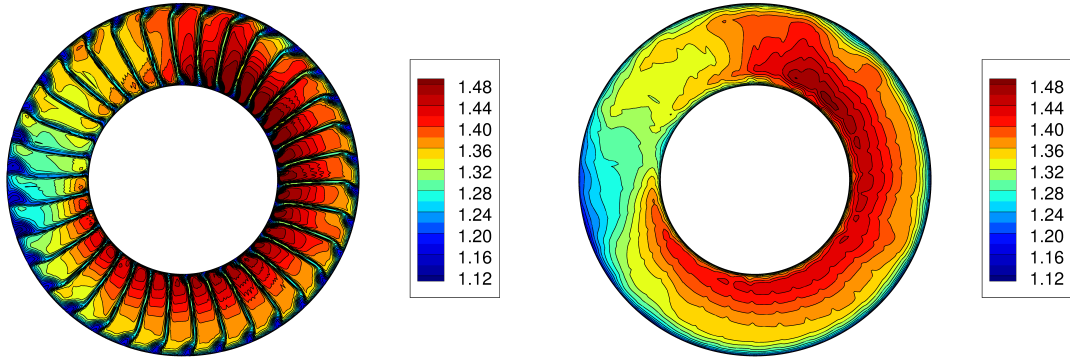


FIGURE 4.41. Total pressure downstream of stator for time-averaged solution (left) and time-pitch-averaged solution (right).

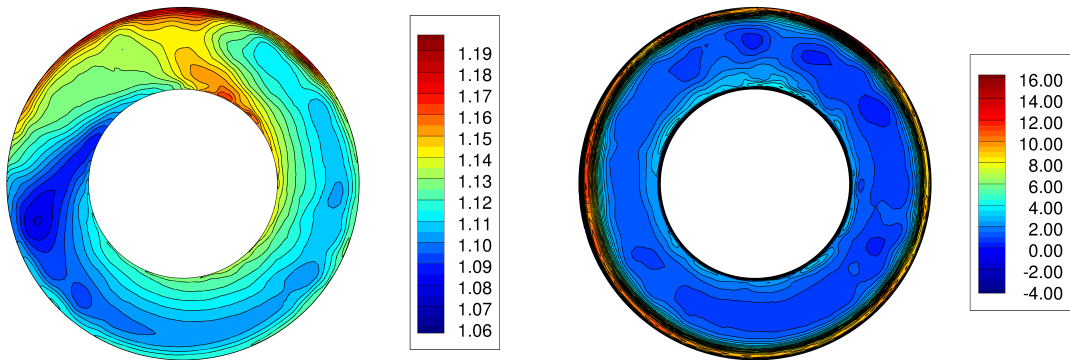


FIGURE 4.42. Total temperature (left) and absolute whirl angle (right) downstream of stator for time-pitch-averaged solution.

The effects of co-swirl and counter-swirl are clearly seen in the blade-to-blade total pressure and temperature contours shown in Figures 4.43 – 4.44. This result is in excellent agreement with results shown by Fidalgo *et al* [2]. The nonuniform stagnation quantities downstream of the rotor, resulting from the fan-distortion interaction, are convected through the stator row with only small changes. However, distortions in static pressure appear to be suppressed in the rotor, as observed in Figure 4.45.

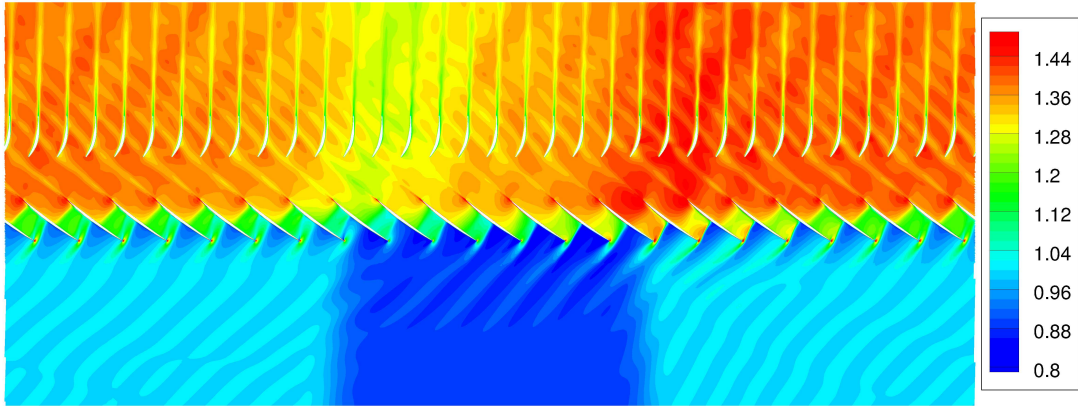


FIGURE 4.43. Total pressure $\left(\frac{P_0}{P_{0_{\text{inlet, clean}}}}\right)$ contours for an unwrapped constant radius slice at 90% span at the rotor's trailing edge.

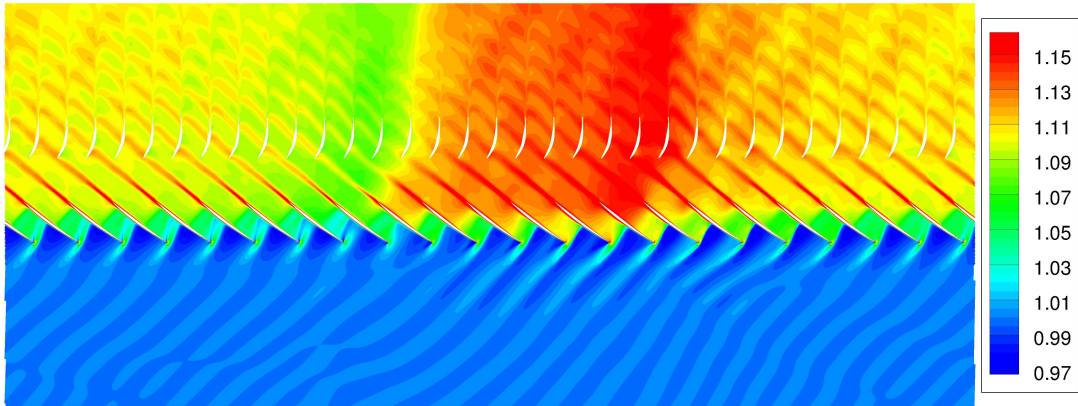


FIGURE 4.44. Total temperature $\left(\frac{T_0}{T_{0_{\text{inlet, clean}}}}\right)$ contours for an unwrapped constant radius slice at 90% span at the rotor's trailing edge.

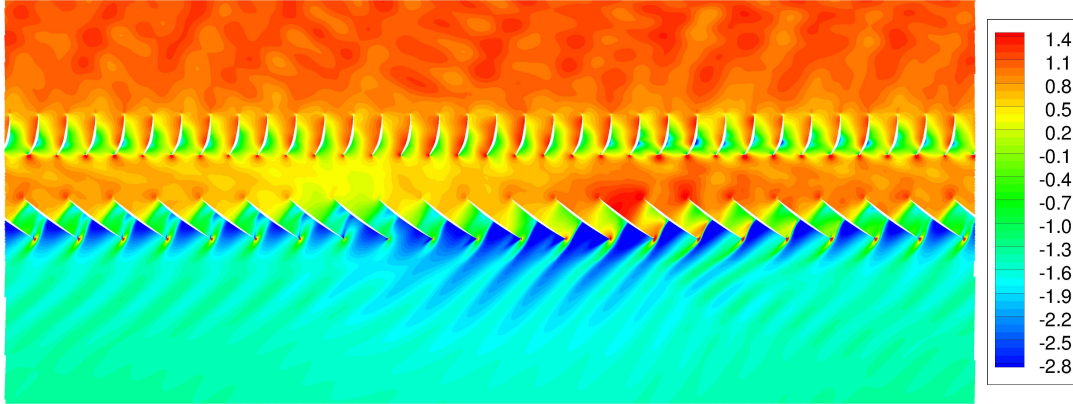


FIGURE 4.45. Static pressure $\left(\frac{P - P_{0\text{inlet, clean}}}{P_{0\text{inlet, clean}} - P_{\text{avg, stn1}}}\right)$ contours for an unwrapped constant radius slice at 90% span at the rotor's trailing edge.

4.2.2. STAGE WITH CENTER BODY, NACELLE, AND NOZZLE. The overall flow domain for the complete system was investigated. Figure 4.46 shows the exhaust jet from the stage, simulated at an AOA of 30° . The figure indicates lower total pressures at the spreading edges of the jet due to mixing. Unsteady low pressure waves propagate from the fan to the outlet of the nacelle. The interaction of the fan with the upstream flow is illustrated in Figure 4.47. In the figure, the flows obtained from two configurations with the same mass flow rate and AOA are compared; the left is the nacelle without the fan stage and the right contains the actual fan stage. Separation is observed on the nacelle when the fan is not present, but such separation is not observed in the presence of the fan. This is consistent with the physics elucidated by the case with purely circumferential distortion, and can be explained by the fact that the fan draws harder from the regions of low total pressure.

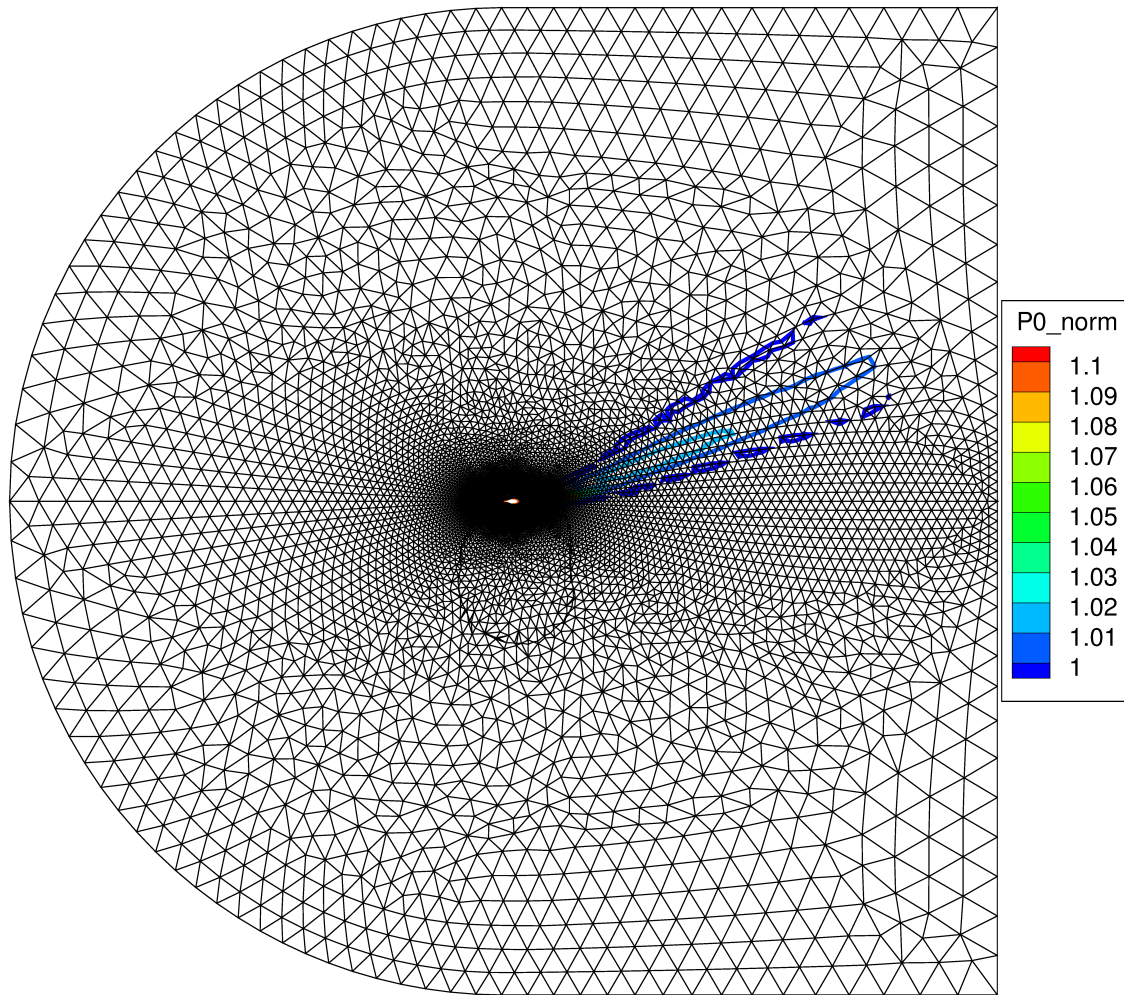


FIGURE 4.46. Contours of total pressure on a planar slice defined by the in-flow direction and axis of rotation, showing free jet dissipation. $M_\infty = 0.25$

The interaction between the fan and the flow in the nacelle can also be seen in Figure 4.48, in which a large region of separated flow is observed along the inner surface of the bottom wall in the case without the fan stage, and only a slightly thickened boundary layer is observed in the case with the fan stage. Waves of low total pressure, propagating upstream from the leading edge shocks, are also visible in the case where the fan stage is included.

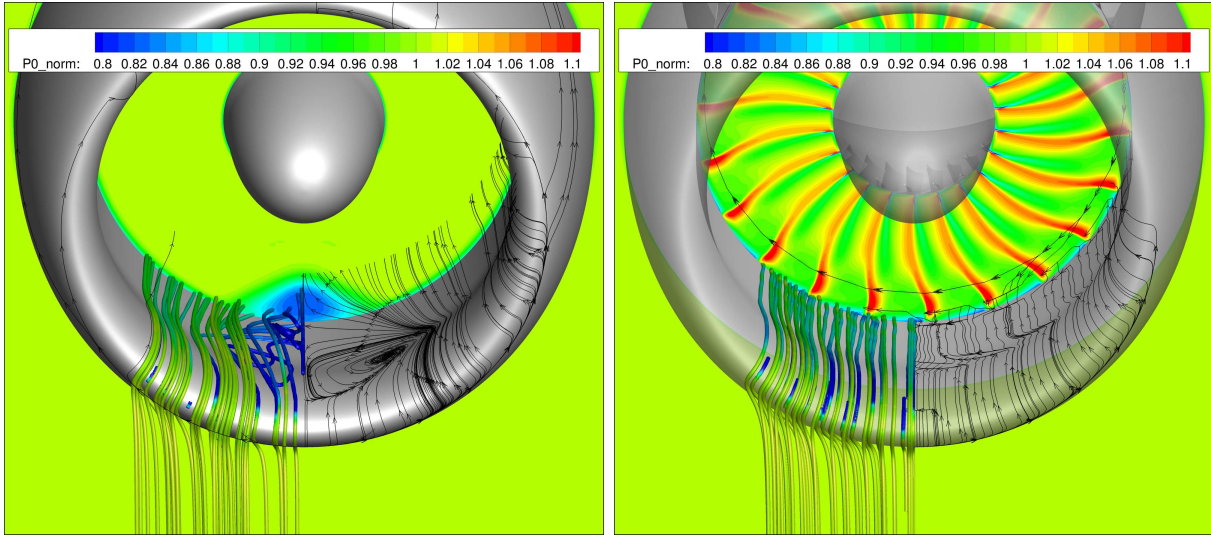


FIGURE 4.47. Total pressure contours, volume streamlines colored by total pressure, and surface streamlines for configurations without the fan stage (left) and with the fan stage (right), both passing the same mass flow and at 30° AOA.

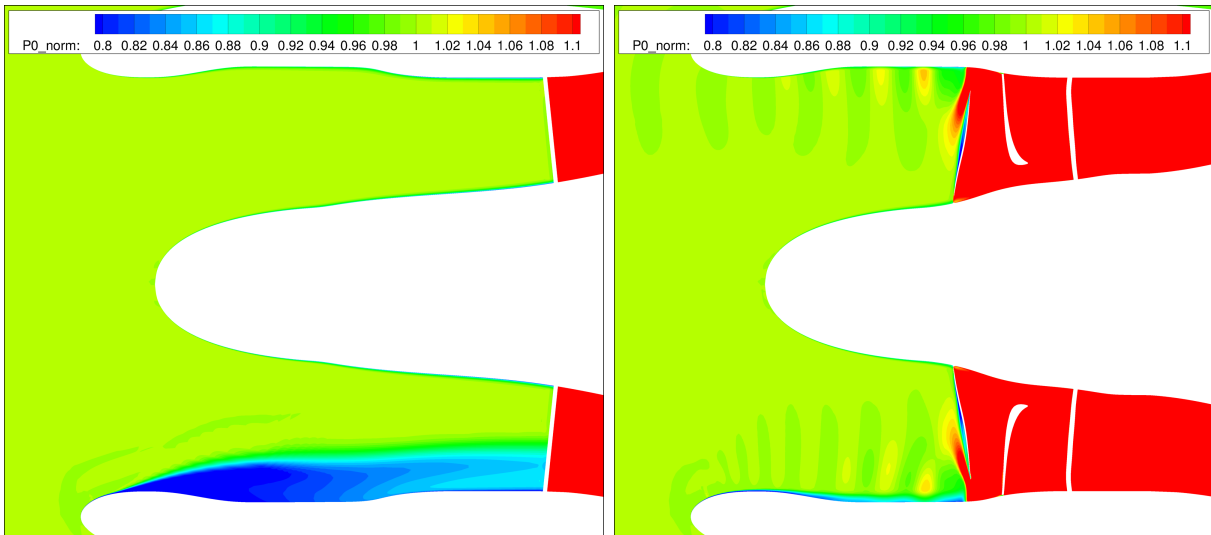


FIGURE 4.48. Contours of total pressure on a planar slice defined by AOA vector and axis of rotation; without the fan stage (left) and with the fan stage (right). $M_\infty = 0.25$

The static pressure distribution within the nacelle is also markedly affected by the fan. From Figure 4.49 it can be seen that the influence of the fan extends to the lip of the nacelle, as indicated by comparison of the size of the region of lowest static pressure, for the cases with

and without the fan.

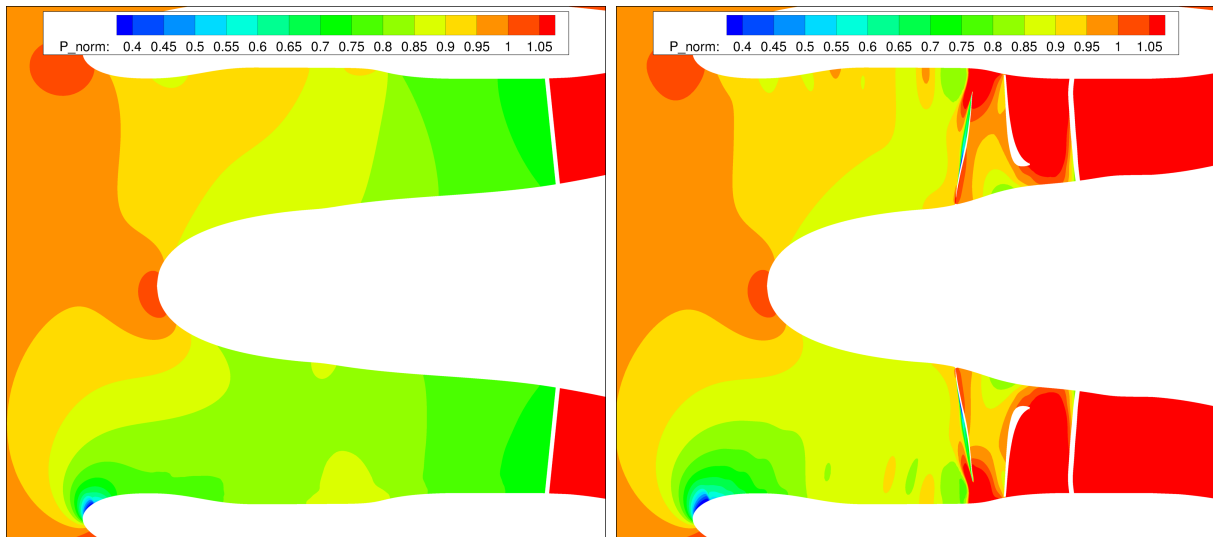


FIGURE 4.49. Contours of static pressure on a planar slice defined by AOA vector and axis of rotation; without the fan stage (left) and with the fan stage (right). $M_\infty = 0.25$

This thesis research is unique in that the flow physics of fan-distortion interaction that have been elucidated for purely circumferential distortion can be observed to change the interaction of fan system components in a geometry more representative of the propulsion system found in commercial aircraft.

CHAPTER 5

CONCLUSIONS AND FUTURE WORK

5.1. CONCLUSIONS

This thesis work has contributed to an in-depth understanding of flow dynamics and their influence on aerodynamic performance, in the single passage and the full annulus configuration of the engine fan/nacelle system with realistic operating conditions. The primary findings for the single passage flow are listed below.

- (1) The flow characteristics predicted by the CFD study are in good agreement with the experimental data for both local distributions of flow quantities and the overall fan performance.
- (2) The overall flow field of the passage and upstream of the rotor is relatively insensitive to spatial resolution and choice of turbulence model. However, aerodynamic performance is sensitive to both the grid resolution and the choice of turbulence model. Convergence of cases near the stall point is also sensitive to these factors.

The findings for the full annulus configuration are listed below.

- (1) Without the nacelle and nozzle added to the configuration, the results agree well with those obtained by Fidalgo *et al.* [2], including physics such as strong fan-distortion interactions. The fan acts to reduce the total pressure distortion field, resulting in distortions in the static pressure and in the flow angles (both whirl angle and radial flow angle).
- (2) With the addition of nacelle and nozzle to the configuration, initial results demonstrate similar trends as those seen in the cases without nacelle and nozzle. However,

fan-distortion interaction becomes strong as the flow develops, and the separation in the nacelle is largely suppressed.

5.2. FUTURE WORK

The following list suggests potential options for future follow-up research

- (1) Simulation of full geometry in cross-flow.
- (2) High-fidelity simulation using large eddy simulation, and/or improved delayed detached eddy simulation approaches.
- (3) Investigation of the effects of turbulence models near the stall condition.
- (4) Similar fan-distortion interaction study, but for shorter nacelle/spinner.

BIBLIOGRAPHY

- [1] R. V. Chima, "Viscous three-dimensional calculations of transonic fan performance," Technical Memorandum 103800, NASA, 1991.
- [2] V. J. Fidalgo, C. A. Hall, and Y. Colin, "A study of fan-distortion interaction within the NASA Rotor 67 transonic stage," *Journal of Turbomachinery*, vol. 134, no. 5, 2012.
- [3] A. J. Strazisar, J. R. Wood, M. D. Hathaway, and K. L. Suder, "Laser anemometer measurements in a transonic axial-flow fan rotor," Technical Paper 2879, NASA, Cleveland, Ohio, Nov 1989.
- [4] A. J. Strazisar, "Investigation of flow phenomenon in a transonic fan rotor using laser anemometry," Technical Memorandum 83555, NASA, Cleveland, Ohio, 1984.
- [5] M. D. Hathaway, "Unsteady flows in a single-stage transonic axial-flow fan stator row," Technical Memorandum 88929, NASA, Cleveland, Ohio, Dec 1986.
- [6] K. L. Suder, M. D. Hathaway, T. H. Okiishi, A. J. Strazisar, and J. J. Adamczyk, "Measurements of the unsteady flow field within the stator row of a transonic axial-flow fan: I - measurement and analysis technique," Technical Memorandum 88945, NASA, Cleveland, Ohio, Dec 1987.
- [7] M. D. Hathaway, K. L. Suder, T. H. Okiishi, A. J. Strazisar, and J. J. Adamczyk, "Measurements of the unsteady flow field within the stator row of a transonic axial-flow fan: II - results and discussion," Technical Memorandum 88946, NASA, Cleveland, Ohio, Dec 1987.
- [8] M. J. Pierzga and J. R. Wood, "Investigation of the three-dimensional flow field within a transonic fan rotor: Experiment and analysis," Technical Memorandum 83739, NASA, Cleveland, Ohio, 1984.

- [9] C. Hah and L. Reid, “A viscous flow study of shock-boundary layer interaction, radial transport, and wake development in a transonic compressor,” *Journal of Turbomachinery*, vol. 114, pp. 538–547, June 1992.
- [10] I. K. Jennions and M. G. Turner, “Three-dimensional Navier-Stokes computations of transonic fan flow using an explicit flow solver and an implicit - solver,” *Journal of Turbomachinery*, vol. 115, pp. 261–272, Apr 1993.
- [11] A. Arnone, “Viscous analysis of three-dimensional rotor flow using a multigrid method,” *Journal of Turbomachinery*, vol. 116, no. 3, 1994.
- [12] T. Arima, T. Sonoda, M. Shirotori, A. Tamura, and K. Kikuchi, “A numerical investigation of transonic axial compressor rotor flow using a low Reynolds number k-epsilon turbulence model,” in *Proceedings of ASME International Gas Turbine and Aeroengine Congress and Exhibition*, ASME, June 1997.
- [13] A. D. Grosvenor, “RANS prediction of transonic compressive rotor performance near stall,” in *Proceedings of ASME Turbo Expo 2007: Power for Land, Sea, and Air*, ASME, May 2007.
- [14] A. D. Grosvenor, “Numerical studies toward prediction, analysis and treatment of SWBLI in transonic compressors,” in *Proceedings of the International Conference on the Methods of Aerophysical Research*, 2008.
- [15] A. D. Grosvenor, G. S. Rixon, L. M. Sailer, M. A. Matheson, D. P. Gutzwiller, A. De-meulenaere, M. Gontier, and A. J. Strazisar, “High resolution RANS nonlinear harmonic study of stage 67 tip injection physics,” *Journal of Turbomachinery*, vol. 137, May 2015.
- [16] J. D. Adamczyk, “Model equation for simulating flows in multistage turbomachinery,” in *Proceedings of ASME Gas Turbine Conference and Exhibit*, ASME, March 1985.

- [17] T. Dang, S. Damle, and X. Qiu, “Euler-based inverse method for turbomachine blades, part 2: Three-dimensional flows,” *AIAA Journal*, vol. 38, pp. 2007–2013, 2000.
- [18] H.-D. Li, L. He, and R. Li, Y. S. Wells, “Blading aerodynamics design optimization with mechanical and aeromechanical constraints,” in *Proceedings of ASME Turbo Expo 2007: Power for Land, Sea, and Air*, pp. 1319–1328, ASME, May 2006.
- [19] S. Pierret, R. Filomeno Coelho, and H. Kato, “Multidisciplinary and multiple operating points shape optimization of three-dimensional compressor blades,” *Structural and Multidisciplinary Optimization*, vol. 33, no. 1, pp. 61–70, 2007.
- [20] J. Luo, F. Liu, and C. Zhou, “Multi-point design optimization of a transonic compressor blade by using an adjoint method,” in *Proceedings of the ASME Turbo Expo 2013: Turbine Technical Conference and Exposition*, ASME, Jun 2013.
- [21] H. Im, X. Chen, and G. Zha, “Detached-eddy simulation of rotating stall inception for a full-annulus transonic rotor,” *Journal of Turbomachinery*, vol. 28, no. 4, 2012.
- [22] H. Khaleghi, “Stall inception and control in a transonic fan, part a: Rotating stall inception,” *Aerospace Science and Technology*, vol. 41, pp. 250–258, 2015.
- [23] D. C. Urasek, W. T. Gorrel, and W. S. Cunnann, “Performance of two-stage fan having low-aspect-ratio, first-stage rotor blading,” Technical Paper 1493, NASA, 1979.
- [24] W. S. Cunnann, W. Stevans, and D. C. Urasek, “Design and performance of a 427-meter-per-second-tip-speed two-stage fan having a 2.40 pressure ratio,” Technical Paper 1314, NASA, 1978.
- [25] “<http://www.pointwise.com/>.”
- [26] “<http://www.metacomptech.com/>.”

- [27] X. Gao, S. M. J. Guzik, and P. Colella, “Fourth order boundary treatment for viscous fluxes on Cartesian grid finite-volume methods,” AIAA 2014-1277, 52nd AIAA Aerospace Sciences Meeting, 2014.
- [28] X. Gao and C. P. T. Groth, “A parallel solution-adaptive method for three-dimensional turbulent non-premixed combustions flows,” *J. Computational Phys.*, vol. 229, pp. 3250–3275, 2010.

APPENDIX A

TURBULENCE MODELS AND NEAR-WALL TURBULENCE TREATMENT

A.1. TURBULENCE MODELS

Briefly, the turbulence models used in the current work are summarized below.

(1) One equation Spalart-Allmaras model:

$$\frac{\partial \tilde{\nu}}{\partial t} + U_j \frac{\partial \tilde{\nu}}{\partial x_j} = c_{b1} \tilde{S} \tilde{\nu} - c_{w1} f_w \left(\frac{\tilde{\nu}}{d} \right)^2 + \frac{1}{\sigma} \frac{\partial}{\partial x_k} \left[(\nu + \tilde{\nu}) \frac{\partial \tilde{\nu}}{\partial x_k} \right] + \frac{c_{b2}}{\sigma} \frac{\partial \tilde{\nu}}{\partial x_k} \frac{\partial \tilde{\nu}}{\partial x_k}. \quad (22)$$

The kinematic eddy viscosity, ν_T , is given by

$$\nu_T = \tilde{\nu} f_{\nu 1}. \quad (23)$$

The source term, \tilde{S} , the mean rotation tensor, Ω_{ij} , and the vorticity magnitude, Ω , are defined by

$$\tilde{S} = \Omega + \frac{\tilde{\nu}}{\kappa^2 d^2} f_{\nu 2}, \quad \Omega_{ij} = \frac{1}{2} \left(\frac{\partial U_i}{\partial x_j} - \frac{\partial U_j}{\partial x_i} \right), \quad \Omega = \sqrt{2\Omega_{ij}\Omega_{ij}},$$

where d is the distance to nearest wall, κ is the Von Kàrmàn constant, and U is the freestream velocity. The closure coefficients and auxiliary relations are $c_{b1} = 0.1355$, $c_{b2} = 0.622$, $c_{\nu 1} = 7.1$, $\sigma = 2/3$, $c_{w1} = \frac{c_{b1}}{\kappa^2} + \frac{(1+c_{b2})}{\sigma}$, $c_{w2} = 0.3$, $c_{w3} = 2$, $\kappa = 0.41$, $f_{\nu 1} = \frac{\chi^3}{\chi^3 + c_{\nu 1}^3}$, $f_{\nu 2} = 1 - \frac{\chi}{1 + \chi f_{\nu 1}}$, $f_w = g \left[\frac{1 + c_{w3}^6}{g^6 + c_{w3}^6} \right]^{1/6}$, $\chi = \frac{\tilde{\nu}}{\nu}$, $g = r + c_{w2}(r^6 - r)$, where $r = \frac{\tilde{\nu}}{\tilde{S}\kappa^2 d^2}$.

(2) Two-equation realizable k - ϵ model:

The transport equations for turbulent kinetic energy, k , and the rate of dissipation of turbulent kinetic energy, ϵ , are given by

$$\frac{\partial(\rho k)}{\partial t} + \frac{\partial(\rho k U_j)}{\partial x_j} = \frac{\partial}{\partial x_j} \left[\left(\mu + \frac{\mu_t}{\sigma_k} \right) \frac{\partial k}{\partial x_j} \right] + 2\mu_t S_{ij}^* S_{ij}^* - \rho \epsilon, \quad (24)$$

$$\frac{\partial(\rho \epsilon)}{\partial t} + \frac{\partial(\rho \epsilon U_j)}{\partial x_j} = \frac{\partial}{\partial x_j} \left[\left(\mu + \frac{\mu_t}{\sigma_\epsilon} \right) \frac{\partial \epsilon}{\partial x_j} \right] + \rho C_1 \sqrt{2S_{ij}^* S_{ij}^*} \epsilon - \rho C_2 \frac{\epsilon^2}{k + \sqrt{\nu \epsilon}}. \quad (25)$$

The mean strain-rate tensor, S_{ij}^* , and the eddy viscosity, μ_t , are defined by

$$S_{ij}^* = \frac{1}{2} \left(\frac{\partial U_i}{\partial x_j} + \frac{\partial U_j}{\partial x_i} \right) - \frac{1}{3} \frac{\partial U_k}{\partial x_k}, \quad \mu_t = \rho C_\mu \frac{k^2}{\epsilon},$$

where the closure coefficients and auxiliary relations are given by

$$C_1 = \max \left[0.43, \frac{\eta}{\eta + 5} \right], C_2 = 1.9, C_\mu = 0.09, \eta = \sqrt{2S_{ij}^* S_{ij}^*} \frac{k}{\epsilon}, \sigma_k = 1.0, \sigma_\epsilon = 1.2.$$

(3) The two-equation nonlinear (cubic) k - ϵ model:

The transport equations for turbulent kinetic energy, k , and the rate of dissipation of turbulent kinetic energy, ϵ , are given by

$$\frac{\partial(\rho k)}{\partial t} + \frac{\partial(\rho U_i k)}{\partial x_i} = \frac{\partial}{\partial x_i} \left[\left(\mu + \frac{\mu_t}{\sigma_k} \right) \frac{\partial k}{\partial x_i} \right] + P_k - \rho \epsilon, \quad (26)$$

$$\frac{\partial(\rho \epsilon)}{\partial t} + \frac{\partial(\rho U_i \epsilon)}{\partial x_i} = \frac{\partial}{\partial x_i} \left[\left(\mu + \frac{\mu_t}{\sigma_\epsilon} \right) \frac{\partial \epsilon}{\partial x_i} \right] + (C_{\epsilon 1} P_k - [C_{\epsilon 2} \rho \epsilon - E]) T_t^{-1}, \quad (27)$$

where $P_k = -\overline{\rho u'_i u'_j} \frac{\partial U_i}{\partial x_j}$ and $\overline{\rho u'_i u'_j}$ is modeled by

$$\begin{aligned}
\overline{\rho u'_i u'_j} = & \rho \frac{2}{3} k \delta_{ij} - \mu_t \tilde{S}_{ij} \\
& + c_1 \frac{\mu_t k}{\epsilon} \left(\tilde{S}_{ij} \tilde{S}_{kj} - \frac{1}{3} \tilde{S}_{kl} \tilde{S}_{kl} \delta_{ij} \right) \\
& + c_2 \frac{\mu_t k}{\epsilon} \left(\Omega_{ik} \tilde{S}_{kj} + \Omega_{jk} \tilde{S}_{ki} \right) \\
& + c_3 \frac{\mu_t k}{\epsilon} \left(\Omega_{ij} \Omega_{jk} - \frac{1}{3} \Omega_{lk} \Omega_{lk} \delta_{ij} \right) \\
& + c_4 \frac{\mu_t k^2}{\epsilon^2} \left(\Omega_{lj} \tilde{S}_{ki} + \Omega_{li} \tilde{S}_{kj} \right) \tilde{S}_{kl} \\
& + c_5 \frac{\mu_t k^2}{\epsilon^2} \left(\Omega_{il} \Omega_{lm} \tilde{S}_{mj} + \Omega_{lm} \Omega_{mj} \tilde{S}_{il} - \frac{2}{3} \Omega_{mn} \Omega_{nl} \tilde{S}_{lm} \delta_{ij} \right) \\
& + c_6 \frac{\mu_t k^2}{\epsilon^2} \tilde{S}_{ij} \tilde{S}_{kl} \tilde{S}_{kl} \\
& + c_7 \frac{\mu_t k^2}{\epsilon^2} \tilde{S}_{ij} \Omega_{kl} \Omega_{kl}.
\end{aligned}$$

The mean strain rate tensor, \tilde{S}_{ij} , mean rotation tensor, Ω_{ij} , non-dimensional strain rate magnitude, S^* , and non-dimensional vorticity magnitude, Ω^* , are defined as

$$\tilde{S}_{ij} = \left(\frac{\partial U_i}{\partial x_j} + \frac{\partial U_j}{\partial x_i} \right) - \frac{2}{3} \frac{\partial U_k}{\partial x_k} \delta_{ij}, \quad \Omega_{ij} = \left(\frac{\partial U_i}{\partial x_j} - \frac{\partial U_j}{\partial x_i} \right), \quad S^* = \frac{k}{\epsilon} \sqrt{\frac{1}{2} \tilde{S}_{ij} \tilde{S}_{ij}}, \quad \Omega^* = \frac{k}{\epsilon} \sqrt{\frac{1}{2} \Omega_{ij} \Omega_{ij}}.$$

The eddy viscosity is calculated as $\mu_t = \frac{C_\mu^* f_\mu \rho k^2}{\epsilon}$.

For the above equations, the following relations are prescribed:

$$\begin{aligned}
\tau = \frac{k}{\epsilon}, \quad T_t = \tau \max\{1, \xi^{-1}\}, \quad \text{where } \xi = \frac{\sqrt{R_t}}{C_\tau}, \quad \text{with } R_t = \frac{k^2}{\nu \epsilon}, \quad \text{and } C_\tau = \sqrt{2}, \\
C_\mu^* = \frac{2/3}{A_1 + S + 0.9\Omega^*}, \quad C_{\mu G} = \min\left\{ \frac{0.09 + 0.13\phi}{1 + \phi^{2.5}}, C_\mu^* \right\}, \quad \phi = |\Omega^* - S^*|, \quad c_1 = \frac{3/4}{(1000 + S^{*3}) C_\mu^*}, \\
c_2 = \frac{15/4}{(1000 + S^{*3}) C_\mu^*}, \quad c_3 = \frac{-19/4}{(1000 + S^{*3}) C_\mu^*}, \quad c_4 = -10 C_\mu^{*2}, \quad c_5 = 0, \quad c_6 = -2 C_\mu^{*2}, \quad c_7 = -c_6, \quad f_\mu = \\
\frac{1 - e^{-A_\mu R_t}}{1 - e^{-\sqrt{R_t}}} \max\{1, \xi^{-1}\}, \quad E = A_{E_\tau} \rho \max\left[k^{\frac{1}{2}}, (\nu \epsilon)^{\frac{1}{4}} \right] \sqrt{\epsilon T_t} \Psi_\tau, \quad \Psi_\tau = \max\left\{ \frac{\partial k}{\partial x_j} \frac{\partial \tau}{\partial x_j}, 0 \right\}.
\end{aligned}$$

The model constants are

$$A_1 = 1.25, C_{\epsilon 1} = 1.44, C_{\epsilon 2} = 1.92, \sigma_k = 1.0, \sigma_\epsilon = 1.3, A_\mu = 0.0085, A_{E_\tau} = 0.15, \text{ and } C_s = 0.05.$$

(4) Two-equation shear stress transport (SST) model:

The Reynolds stresses are given by $\rho \overline{u_i u_j} = \frac{2}{3} \delta_{ij} \rho k - \mu_t \tilde{S}_{ij}$, with the mean strain rate tensor as $\tilde{S}_{ij} = \left(\frac{\partial U_i}{\partial x_j} + \frac{\partial U_j}{\partial x_i} - \frac{2}{3} \frac{\partial U_k}{\partial x_k} \delta_{ij} \right)$. The eddy viscosity is defined as $\nu_t = a_1 k / \max\{a_1 \omega, SF_2\}$. The turbulence kinetic energy transport equation is modeled by

$$\frac{\partial \rho k}{\partial t} + \frac{\partial}{\partial x_j} (U_j \rho k) = \tilde{P}_k - \beta^* \rho k \omega + \nabla \cdot [(\mu + \sigma_k \mu_t) \nabla k]. \quad (28)$$

The turbulence inverse time-scale transport equation is modeled by

$$\frac{\partial \rho \omega}{\partial t} + \frac{\partial}{\partial x_j} (U_j \rho \omega) = \frac{\gamma}{\hat{\nu}_t} P_k - \beta^* \rho \omega^2 + \nabla \cdot [(\mu + \sigma_\omega \mu_t) \nabla \omega] + 2(1 - F_1) \rho \sigma_{\omega 2} \frac{1}{\omega} \nabla k \cdot \nabla \omega, \quad (29)$$

where the turbulence production is computed by

$$P_k = \left[\mu_t \left(\frac{\partial U_i}{\partial x_j} + \frac{\partial U_j}{\partial x_i} + \frac{2}{3} \frac{\partial U_k}{\partial x_k} \delta_{ij} \right) - \frac{2}{3} \rho k \delta_{ij} \right] \frac{\partial U_i}{\partial x_j}.$$

In the k -equation, the turbulence generation term is limited as $\tilde{P}_k = \min(P_k, 10\beta^* \rho k \omega)$.

F_1 and F_2 are blending functions

$$F_1 = \tanh \left\{ \left\{ \min \left[\max \left(\frac{\sqrt{k}}{\beta^* \omega d}, \frac{500\nu}{d^2 \omega} \right), \frac{4\rho \sigma_{\omega 2} k}{CD_{k\omega} d^2} \right] \right\}^4 \right\}$$

with $CD_{k\omega} = \max(2\rho \sigma_{\omega 2} \frac{1}{\omega} \nabla k \cdot \nabla \omega, 10^{-10})$, and

$$F_2 = \tanh \left\{ \left[\max \left(\frac{2\sqrt{k}}{\beta^* \omega d}, \frac{500\nu}{d^2 \omega} \right) \right]^2 \right\}.$$

Blending is implemented by $\phi = \phi_1 F_1 + \phi_2 (1 - F_1)$ with ϕ_1 and ϕ_2 being model constants. Additional model constants are as follows: $\sigma_{k1} = 0.85$ (0.5 for baseline),

$\sigma_{\omega 1} = 0.5$, $\beta_1 = 0.075$, $\gamma_1 = \frac{\beta_1}{\beta^*} - \frac{\sigma_{\omega 1} \kappa^2}{\sqrt{\beta^*}}$, $\sigma_{k 2} = 1.0$, $\sigma_{\omega 2} = 0.856$, $\beta_2 = 0.0828$, $\beta^* = 0.09$, $\kappa = 0.41$, $a_1 = 0.31$, and $\gamma_2 = \frac{\beta_2}{\beta^*} - \frac{\sigma_{\omega 2} \kappa^2}{\sqrt{\beta^*}}$. For wall B.C.'s with $y^+ < 3$, k and ω are specified as $k = 0$ and $\omega = 800 \frac{\nu}{(\nabla y_1)^2}$. The eddy viscosity for the new ω equation is limited by $\hat{\nu}_t = \max(\nu_t, 10^{-8})$

A.2. NEAR-WALL TURBULENCE TREATMENT

The wall functions in the solver used for this work are based on a velocity scale of $k^{1/2}$, where k is the turbulence kinetic energy. The wall shear stress is given by

$$\tau_w = \begin{cases} \frac{\kappa^* \rho_W \sqrt{k_1} (U_{c1} - U_{tw})}{\ln(E y_1^*)} & , y_1^* > y_v^* \\ \frac{\mu_W (U_{c1} - U_{tw})}{y_1} & , y_1^* \leq y_v^* \end{cases}$$

where ρ is density, k is turbulence kinetic energy, μ is dynamic molecular viscosity, U_{tw} is the tangent-to-flow component of the wall velocity vector, $\kappa^* = c_\mu^{1/4} \kappa$, $c_\mu = 0.09$, $\kappa = 0.41$, $E = 8.8$, and $y_v^* = 11.2$. In addition,

$$y^* = \frac{c_\mu^{1/4} \rho_W y \sqrt{k}}{\mu_W}$$

where y is the coordinate normal to the wall surface, and U_c is the velocity tangential to the wall transformed to account for compressibility, heat transfer, and pressure gradient effects

using the van Driest approach described by

$$\begin{aligned}
U_c &= \sqrt{B} \left[\arcsin \left(\frac{A + \tilde{U}_t}{D} \right) - \arcsin \left(\frac{A}{D} \right) \right], \\
A &= (q/\tau)_W, \\
B &= 2 \frac{C_p}{Pr_t} T, \\
D &= \sqrt{A^2 + B}.
\end{aligned} \tag{30}$$

In the above equations, Pr_t is the turbulent Prandtl Number (typically 0.9), q_W is the wall heat transfer rate, and \tilde{U}_t is computed by

$$\tilde{U}_t = \begin{cases} U_t - \frac{1}{2} \frac{dp}{dx} \left[\frac{y_v}{\kappa^* \rho \sqrt{k}} \ln \left(\frac{y}{y_v} \right) + \frac{y - y_v}{\kappa^* \rho \sqrt{k}} + \frac{y_v^2}{\mu} \right], & y_1^* > y_t^*; \\ U_t, & y_1^* \leq y_t^*. \end{cases} \tag{31}$$

Also, the assumption is made that the wall is located at the viscous sublayer edge, and therefore

$$y_1^* = \max \{y_1^*, y_t^*\}. \tag{32}$$

Equations for k and ϵ are solved in the entire domain. When $y_1^* > y_v^*$, the wall boundary conditions for k and ϵ are determined from their behavior in the logarithmic overlap using

$$\{\partial k / \partial y\}_W = 0, \tag{33}$$

$$\epsilon_W = \epsilon_1 + C_{cal} \frac{y_1 u_\tau^5}{\kappa (y_v^* \nu)^2}, \tag{34}$$

where $\nu = \mu/\rho$, $u_\tau = c_\mu^{1/4} \sqrt{k}$ and C_{cal} is a calibration constant equal to 0.1. If $y_1^* = y_v^*$, the smooth wall boundary conditions for k and ϵ are specified as $k_w = 0$ and $\epsilon_w = \epsilon_1$. The

production and dissipation of k are set at the wall-adjacent centroid as follows. For flow without significant pressure gradient, the assumption of local equilibrium allows

$$P_k = \frac{(\tau/\rho)_W^2}{\kappa^* \sqrt{k_1} y_1}, \quad (35)$$

$$\epsilon = \frac{c_\mu^{3/4} k_1^{3/2}}{\kappa y_1}. \quad (36)$$

APPENDIX B

DATA POST-PROCESSING SCRIPTS FOR SINGLE-PASSAGE ROTOR-ALONE SIMULATIONS

B.1. BASH SCRIPT FOR CALCULATING PERFORMANCE USING BOTH RAKE AND SLICE INTEGRATION

```
#!/bin/bash
#Check for ../post_data/ and create if it does not exists
if [ ! -d ../post_data ]; then
    mkdir '../post_data'
fi
# Outlet boundaries:
# Rotor alone without spinner: 1
# Rotor alone with spinner: 2
# Set boundary in CFD++ to check the mass flow across
boundary=1
#Tecplot solution zone max
zonemax=11
#Tecplot zones
let src1=$zonemax+1
let src2=$zonemax+2
let dest1=$zonemax+3
let dest2=$zonemax+4
#Create header for map.txt
echo 'ratio iteration mdot/22 mdot_total rake_mdot_corr
rake_FRP rake_Eff slice_mdot_corr slice_FPR slice_Eff
mdot_norm rake_mdot_norm slice_mdot_norm' > '../post_data/
map.tmp.txt'
#Iterate over all cases in ../cases
for ratio in `find ../cases/ -maxdepth 1 -mindepth 1 -type d |
sort`;do
    ratio=$(basename "$ratio")
#Only iterate over cases with mcftec.bin
if [ -f "../cases/$ratio/mcftec.bin" ]; then
#Export variables needed in Tecplot macro
#For single passage, rotor alone cases, GRIDONE="stn1_interp.x
", GRIDTWO="stn2_interp.x"
export FILE="../cases/$ratio/mcftec.bin"
export XONE="-0.02473"
export XTWO="0.11"
```

```

export GRIDONE="../scripts/stn1_interp_med.x"
export GRIDTWO="../scripts/stn2_interp_med.x"
export OUTONE="stn1"
export OUTTWO="stn2"
export SRCONE="$src1"
export SRCTWO="$src2"
export DESTONE="$dest1"
export DESTTWO="$dest2"
echo "Input file is $FILE"
echo "Station 1 is at x=$XONE"
echo "Station 2 is at x=$XTWO"
echo "Interpolation grid for station 1 is $GRIDONE"
echo "Interpolation grid for station 2 is $GRIDTWO"
#Change directories to ../post_data
cd ../post_data
#Interpolate to structured grids with tecplot
#Tecplot macro writes to $OUTONE.dat, $OUTTWO.dat, PO.txt, and
  TO.txt
/opt/tecplot360ex/bin/tec360 -b -p ../scripts/output_slices.mcr
#split header from tecplot output file
sed -n '/DOUBLE )/,,$p' "$OUTONE".dat | tail -n +2 > "$OUTONE
  ""_data".dat"
sed '/DOUBLE )/q' "$OUTONE".dat > "$OUTONE""_header".dat"
sed -n '/DOUBLE )/,,$p' "$OUTTWO".dat | tail -n +2 > "$OUTTWO
  ""_data".dat"
sed '/DOUBLE )/q' "$OUTTWO".dat > "$OUTTWO""_header".dat"
#read array dimensions from first header
dimline=$(sed -n '/I=/p' "$OUTONE""_header".dat" )
stringarray=($dimline)
dimone=$(echo ${stringarray[0]} | sed 's/[^0-9]*//g')
dimtwo=$(echo ${stringarray[1]} | sed 's/[^0-9]*//g')
echo "Number of radial points in at station 1 is $dimone"
echo "Number of circumferential points at station 1 is $dimtwo"
#read array dimensions from second header
dimlinetwo=$(sed -n '/I=/p' "$OUTTWO""_header".dat" )
stringarraytwo=($dimlinetwo)
dimthree=$(echo ${stringarraytwo[0]} | sed 's/[^0-9]*//g')
dimfour=$(echo ${stringarraytwo[1]} | sed 's/[^0-9]*//g')
echo "Number of radial points in at station 2 is $dimthree"
echo "Number of circumferential points at station 2 is $dimfour"
"
#run MATLAB
cd ../scripts
/opt/matlab/bin/matlab -nojvm -nodisplay -nosplash -r "
  theta_mass_ave("$dimone","$dimtwo",'$OUTONE'), quit"

```

```

/opt/matlab/bin/matlab -nojvm -nodisplay -nosplash -r "
    theta_mass_ave("$dimthree","$dimfour",'$OUTTWO'), quit"
cd ../post_data
#edit Tecplot header
sed 's/"X"/"radius"/g' "$OUTONE"_header.dat > "$OUTONE"_
_header_avg.dat"
sed -i '3,4d' "$OUTONE"_header_avg.dat"
sed -i "s/J=$dimtwo,/J=1,/" "$OUTONE"_header_avg.dat"
sed 's/"X"/"radius"/g' "$OUTTWO"_header.dat > "$OUTTWO"_
_header_avg.dat"
sed -i '3,4d' "$OUTTWO"_header_avg.dat"
sed -i "s/J=$dimfour,/J=1,/" "$OUTTWO"_header_avg.dat"
cat "$OUTONE"_header_avg.dat "$OUTONE"_data_avg.dat > "
$outone"_avg.dat"
cat "$OUTTWO"_header_avg.dat "$OUTTWO"_data_avg.dat > "
$outtwo"_avg.dat"
cp "$OUTONE"_avg.dat "$ratio"_"$OUTONE"_avg.dat"
cp "$OUTTWO"_avg.dat "$ratio"_"$OUTTWO"_avg.dat"
# extract P0.txt and T0.txt values to variables
P0stn1=$(sed -n 2p ../post_data/P0.txt | cut -d " " -f 8 |sed '
s/....$//')
P0stn2=$(sed -n 3p ../post_data/P0.txt | cut -d " " -f 8 |sed '
s/....$//')
T0stn1=$(sed -n 2p ../post_data/T0.txt | cut -d " " -f 8 |sed '
s/....$//')
T0stn2=$(sed -n 3p ../post_data/T0.txt | cut -d " " -f 8 |sed '
s/....$//')
echo "Slice P01 = $P0stn1"
echo "Slice P02 = $P0stn2"
echo "Slice T01 = $T0stn1"
echo "Slice T02 = $T0stn2"
#Find mass flow rate
if [ -f "../cases/$ratio/mcfd.info1" ]; then
    mdot='sed -n '/'"nbc = $boundary,"'/{n;n;p}' "../
cases/$ratio/mcfd.info1" | tail -n 1 | cut -d ' ' -f
6 | sed 's/....$//'
    boolean='echo "$mdot > 1.7" | bc'
    if [ $boolean -eq 1 ]; then
        mdotnew=$(echo "scale=9; $mdot / 10" | bc)
        echo "$mdotnew"
        mdot="$mdotnew"
    fi
    echo 'Mass flow / 22 = '"$mdot"
    mdot_total=$(echo "$mdot*22" | bc)
    echo 'Total mass flow = '"$mdot_total"

```

```

        iter='grep "^nt" "../cases/$ratio/mcfd.info1" | tail -n
            1 | cut -d " " -f 2'
        echo 'Iterations = "$iter"'
        echo "$ratio" "$iter" "$mdot" "$mdot_total" "$rake_FPR"
            "$rake_Eff" "$slice_FPR" "$slice_Eff"
    else
        echo 'mcfd.info1 file does not exist for' "../cases/
            $ratio"
        echo "$ratio"
    fi
#run MATLAB
cd ../scripts
/opt/matlab/bin/matlab -nojvm -nodisplay -nosplash -r "
    performance("$dimone",'$OUTONE','$OUTTWO', "$P0stn1", "
        $P0stn2", "$T0stn1", "$T0stn2", "$mdot_total", "$iter"),
    quit"
cd ../post_data
rake_mdot_corr=$(cat "avg_perf.txt" | cut -d " " -f 1)
rake_FPR=$(cat "avg_perf.txt" | cut -d " " -f 2)
rake_Eff=$(cat "avg_perf.txt" | cut -d " " -f 3)
slice_mdot_corr=$(cat "avg_perf.txt" | cut -d " " -f 4)
slice_FPR=$(cat "avg_perf.txt" | cut -d " " -f 5)
slice_Eff=$(cat "avg_perf.txt" | cut -d " " -f 6)
rm avg_perf.txt
#check if the cases is at choked condition
check=$(echo "$ratio == 0.800" | bc)
echo check="$check"
#if at choked condition save values for normalization of mass
    flow rates
if [ "$check" -eq 1 ]; then
mdot_choke="$mdot_total"
slice_mdot_corr_choke="$slice_mdot_corr"
rake_mdot_corr_choke="$rake_mdot_corr"
echo mdot_choke="$mdot_total"
echo slice_mdot_corr_choke="$slice_mdot_corr"
echo rake_mdot_corr_choke="$rake_mdot_corr"
fi
echo mdot_choke="$mdot_total"
echo slice_mdot_corr_choke="$slice_mdot_corr"
echo rake_mdot_corr_choke="$rake_mdot_corr"
mdot_norm=$(echo "scale=13; $mdot_total/$mdot_choke" | bc)
slice_mdot_norm=$(echo "scale=13; $slice_mdot_corr/
    $slice_mdot_corr_choke" | bc)
rake_mdot_norm=$(echo "scale=13; $rake_mdot_corr/
    $rake_mdot_corr_choke" | bc)

```

```

echo mdot_norm=$(echo "scale=13; $mdot_total/$mdot_choke" | bc)
echo slice_mdot_norm=$(echo "scale=13; $slice_mdot_corr/
    $slice_mdot_corr_choke" | bc)
echo rake_mdot_norm=$(echo "scale=13; $rake_mdot_corr/
    $rake_mdot_corr_choke" | bc)
#Write
    if [ -f "../cases/$ratio/mcfd.info1" ]; then
        echo 'Iterations = '$iter"
        echo "$ratio" "$iter" "$mdot" "$mdot_total" "
            $rake_mdot_corr" "$rake_FPR" "$rake_Eff" "
            $slice_mdot_corr" "$slice_FPR" "$slice_Eff" "
            $mdot_norm" "$rake_mdot_norm" "$slice_mdot_norm">> '
            map.tmp.txt'
    else
        echo 'mcfd.info1 file does not exist for' "../cases/
            $ratio"
        echo "$ratio" >> 'map.tmp.txt'
    fi
#remove temporary files
rm *data* *header*
fi
#Write
echo 'ratio iteration mdot/22 mdot_total rake_mdot_corr
    rake_FRP rake_Eff slice_mdot_corr slice_FPR slice_Eff
    mdot_norm rake_mdot_norm slice_mdot_norm'
echo "$ratio" "$iter" "$mdot" "$mdot_total" "$rake_mdot_corr"
    "$rake_FPR" "$rake_Eff" "$slice_mdot_corr" "$slice_FPR" "
    $slice_Eff" "$mdot_norm $rake_mdot_norm $slice_mdot_norm"
done
#remove temporary files
rm "$OUTONE"'.dat' "$OUTTWO"'.dat' "$OUTONE"'_avg.dat' "$OUTTWO
    "'_avg.dat'
rm *.log
cat ./map.tmp.txt
cp ./map.tmp.txt map.txt
cd ../scripts
#import to tecplot and export as .dat file
/opt/tecplot360ex/bin/tec360 -b -p import_map.mcr

```

B.2. TECPLOT MACRO CALLED BY BASH SCRIPT IN APPENDIX A.1

```

#!MC 1400
# Created by Tecplot 360 build 14.0.2.35002
#import variables from bash script
$!VarSet |MFBD| = '.'

```

```

$!Varset |datafile| = '|$FILE|'
$!Varset |firstx| = '|$XONE|'
$!Varset |secondx| = '|$XTWO|'
$!Varset |firstgrid| = '|$GRIDONE|'
$!Varset |secondgrid| = '|$GRIDTWO|'
$!Varset |firstout| = '|$OUTONE|'
$!Varset |secondout| = '|$OUTTWO|'
$!Varset |firstsrc| = '|$SRCONE|'
$!Varset |secondsrc| = '|$SRCTWO|'
$!Varset |firstdest| = '|$DESTONE|'
$!Varset |seconddest| = '|$DETTWO|'
$!READDATASET  '"|MFBD|/|datafile|" '
  READDATAOPTION = NEW
  RESETSTYLE = YES
  INCLUDETEXT = NO
  INCLUDEGEOM = NO
  INCLUDECUSTOMLABELS = NO
  VARLOADMODE = BYNAME
  ASSIGNSTRANDIDS = YES
  INITIALPLOTTYPE = CARTESIAN3D
  VARNAMELIST = 'X" "Y" "Z" "P" "T" "U" "V" "W" "R" "M" "
    T_total" "P_total" "Y_plus" "VelMag" "Turb1" "U_Rel" "
    V_Rel" "W_Rel" "CPU_Number" "Cell_group" "Sound_speed"'
$!GLOBALTHREED SLICE{NORMAL{X = 1}}
$!GLOBALTHREED SLICE{NORMAL{Z = 0}}
$!GLOBALTHREED SLICE{ORIGIN{X = |firstx|}}
$!CREATESLICEZONEFROMPLANE
  SLICESOURCE = VOLUMEZONES
  FORCEEXTRACTIONTOSINGLEZONE = YES
  COPYCELLCENTEREDVALUES = NO
$!GLOBALTHREED SLICE{ORIGIN{X = |secondx|}}
$!CREATESLICEZONEFROMPLANE
  SLICESOURCE = VOLUMEZONES
  FORCEEXTRACTIONTOSINGLEZONE = YES
  COPYCELLCENTEREDVALUES = NO
$!READDATASET  '"STANDARDSYNTAX" "1.0" "APPEND" "Yes" "
  FILELIST_GRIDFILES" "2" "|MFBD|/|firstgrid|" "|MFBD|/|
  secondgrid|" "IINDEXRANGE" "1,,1" "JINDEXRANGE" "1,,1" "
  KINDEXRANGE" "1,,1" "AUTODETECT" "Yes" "LOADBOUNDARY" "No" "
  ASCIIISDOUBLE" "No" "ASCIIHASIBLANK" "No" "
  SOLUTIONSSHARESTRUCTURE" "Yes" "ASSIGNSTRANDIDS" "Yes" "
  ADDTOEXISTINGSTRANDS" "No" "UNIFORMGRIDSTRUCTURE" "Yes" "
  ASSIGNNEWSTRANDIDFOREACHTIMESTEP" "Yes" "
  EXTRACTTIMEFROMSOLFILENAMES" "No"'
DATASETREADER = 'PLOT3D Loader'

```

```

$! INVERSEDISTINTERPOLATE
SOURCEZONES = [|firstsrc|]
DESTINATIONZONE = |firstdest|
VARLIST = [4-21]
INVDISTEXPONENT = 3.5
INVDISTMINRADIUS = 0
INTERPPTSELECTION = OCTANTNPOINTS
INTERPNPOINTS = 4
$! INVERSEDISTINTERPOLATE
SOURCEZONES = [|secondsrc|]
DESTINATIONZONE = |seconddest|
VARLIST = [4-21]
INVDISTEXPONENT = 3.5
INVDISTMINRADIUS = 0
INTERPPTSELECTION = OCTANTNPOINTS
INTERPNPOINTS = 4
$! PLOTTYPE = CARTESIAN2D
$! TWODAXIS XDETAIL{VARNUM = 2}
$! TWODAXIS YDETAIL{VARNUM = 3}
$! LINEARINTERPOLATE
SOURCEZONES = [|firstsrc|]
DESTINATIONZONE = |firstdest|
VARLIST = [1,4-21]
LINEARINTERPCONST = 0
LINEARINTERPMODE = DONTCHANGE
$! LINEARINTERPOLATE
SOURCEZONES = [|secondsrc|]
DESTINATIONZONE = |seconddest|
VARLIST = [1,4-21]
LINEARINTERPCONST = 0
LINEARINTERPMODE = DONTCHANGE
$! WRITEDATASET "|MFBD|/|firstout|.dat"
INCLUDETEXT = NO
INCLUDEGEOM = NO
INCLUDECUSTOMLABELS = NO
ASSOCIATELAYOUTWITHDATAFILE = NO
ZONELIST = [|firstdest|]
BINARY = NO
USEPOINTFORMAT = YES
PRECISION = 18
TECPLOTVERSIONTOWRITE = TECPLOTCURRENT
$! WRITEDATASET "|MFBD|/|secondout|.dat"
INCLUDETEXT = NO
INCLUDEGEOM = NO
INCLUDECUSTOMLABELS = NO

```

```

ASSOCIATELAYOUTWITHDATAFILE = NO
ZONELIST = [|seconddest|]
BINARY = NO
USEPOINTFORMAT = YES
PRECISION = 18
TECPLOTVERSIONTOWRITE = TECPLOTCURRENT
$!PLOTTYPE = CARTESIAN3D
$!EXTENDEDCOMMAND
COMMANDPROCESSORID = 'CFDAnalyzer4'
COMMAND = 'SetFieldVariables ConvectionVarsAreMomentum=\`F\`
    UVar=6 VVar=7 WVar=8 ID1=\`Pressure\` Variable1=4 ID2=\`
    Temperature\` Variable2=5'
$!EXTENDEDCOMMAND
COMMANDPROCESSORID = 'CFDAnalyzer4'
COMMAND = 'Integrate [|firstsrc|-|secondsrc|] VariableOption
    =\`MassFlowWeightedAverage\` XOrigin=0 YOrigin=0 ZOrigin=0
    ScalarVar=12 Absolute=\`F\` ExcludeBlanked=\`F\`
    XVariable=1 YVariable=2 ZVariable=3 IntegrateOver=\`Cells
    \` IntegrateBy=\`Zones\` IRange={MIN =1 MAX = 0 SKIP = 1}
    JRange={MIN =1 MAX = 0 SKIP = 1} KRange={MIN =1 MAX = 0
    SKIP = 1} PlotResults=\`F\` PlotAs=\`Result\` TimeMin=0
    TimeMax=0'
$!EXTENDEDCOMMAND
COMMANDPROCESSORID = 'CFDAnalyzer4'
COMMAND = 'SaveIntegrationResults FileName=\`|MFBD|/P0.txt\`'
$!EXTENDEDCOMMAND
COMMANDPROCESSORID = 'CFDAnalyzer4'
COMMAND = 'Integrate [|firstsrc|-|secondsrc|] VariableOption
    =\`MassFlowWeightedAverage\` XOrigin=0 YOrigin=0 ZOrigin=0
    ScalarVar=11 Absolute=\`F\` ExcludeBlanked=\`F\`
    XVariable=1 YVariable=2 ZVariable=3 IntegrateOver=\`Cells
    \` IntegrateBy=\`Zones\` IRange={MIN =1 MAX = 0 SKIP = 1}
    JRange={MIN =1 MAX = 0 SKIP = 1} KRange={MIN =1 MAX = 0
    SKIP = 1} PlotResults=\`F\` PlotAs=\`Result\` TimeMin=0
    TimeMax=0'
$!EXTENDEDCOMMAND
COMMANDPROCESSORID = 'CFDAnalyzer4'
COMMAND = 'SaveIntegrationResults FileName=\`|MFBD|/T0.txt\`'
$!RemoveVar |MFBD|

```

B.3. MATLAB SCRIPT TO COMPUTE CIRCUMFERENTIAL AVERAGES; CALLED BY BASH

SCRIPT IN APPENDIX A.1

```
function [] = theta_mass_ave(dimone,dimtwo,fileroot)
```

```

    filein=strcat('..../post_data/', fileroot, '_data.dat')
    fileout=strcat('..../post_data/', fileroot, '_data_avg.dat')
%Import excel data file
IN=dlmread(filein);
%Split xyz data from variable data
XYZ=IN(:,1:3);
D=IN(:,4:end);
%Specify which column contains density in original tecplot file
rhocol=9;
%Shift rhocol by -3 to account for the removal of x, y, and z
rhocol=rhocol-3;
%Specify which column contains U in original tecplot file
ucol=6;
%Shift ucol by -3 to account for the removal of x, y, and z
ucol=ucol-3;
%specify how many points in each passage in the radial
    direction
r=dimone;
%specify how many points in each passage in the circumferential
    direction
c=dimtwo;
%calculate radii
YZ_values=XYZ(1:r,2:3);
radius=sqrt(YZ_values(:,1).^2+YZ_values(:,2).^2);
%Separate D into c pages with r rows each (one theta/page)
for i=1:c
    E(:,:,i)=D(((i-1)*r+1:i*r),:);
end
%initialize AVG with same size as E
AVG=zeros((size(E,1)),(size(E,2)));
%%Calculate averages in circumferential direction
mdot_total=zeros(r,1); %intialize mdot_total
mdot_times_vars_total=zeros(r,size(E,2)); %intialize the array
    summing variables*mdot_theta
    for j=1:c %average interval in theta
        mdot_j=E(:,rhocol,j).*E(:,ucol,j); %calculate mdot at
            theta=j (vector operation at all radii)
        for k=1:size(E,2)
            mdot_times_vars(:,k)=mdot_j.*E(:,k,j);
        end
        mdot_total=mdot_total+mdot_j;%add mdot for the current
            theta to mdot_total
        mdot_times_vars_total=mdot_times_vars_total+
            mdot_times_vars; %add mdot_theta*vars to mdot*vars
            total
    end
end

```

```

    end
    for l=1:size(E,2)
        AVG(:,l)=mdot_times_vars_total(:,l)./mdot_total; %
            average all variable at given theta
    end
%add xyz coordinate back to array
OUT=horzcat(radius,AVG);
%output space-delimited, theta-averaged, data for tecplot
    dlmwrite(fileout,OUT,'delimiter',' ','precision',18);

```

B.4. MATLAB SCRIPT TO COMPUTE AERODYNAMIC PERFORMANCE; CALLED BY BASH SCRIPT IN APPENDIX A.1

```

function [] = theta_mass_ave(dimone,fileone,filetwo, Ptotone,
    Ptottwo, Ttotone, Ttottwo, mdot, iteration)
%dimone=169
%fileone='stn1'
%filetwo='stn2'
Ptotone=Ptotone*10^5
Ptottwo=Ptottwo*10^5
Ttotone=Ttotone*10^2
Ttottwo=Ttottwo*10^2
fileinone=strcat('../post_data/', fileone, '_data_avg.dat');
fileintwo=strcat('../post_data/', filetwo, '_data_avg.dat');
fileout='../post_data/avg_perf.txt';
%Import data file
D=dlmread(fileinone);
E=dlmread(fileintwo);
%Specify which column contains Ptot in original tecplot file
Ptotcol=12;
%Shift rhocol by -2 to account for the removal of y and z
Ptotcol=Ptotcol-2;
%Specify which column contains Ttot in original tecplot file
Ttotcol=11;
%Shift rhocol by -2 to account for the removal of y and z
Ttotcol=Ttotcol-2;
%Specify which column contains U in original tecplot file
ucol=6;
%Shift ucol by -3 to account for the removal of y and z
ucol=ucol-2;
%Specify which column contains rho in original tecplot file
rhocol=9;
%Shift ucol by -3 to account for the removal of y and z
rhocol=rhocol-2;

```

```

%Create vectors with radial points at stn1 and stn2 used to
  calculate performance
rone=[24.2570; 22.6873; 21.1988; 19.6469; 18.0645; 16.4414;
  14.7396; 12.9591; 11.0084];
rtwo=[23.2258; 22.0320; 20.8280; 19.6164; 18.3947; 17.1526;
  15.8902; 14.6126; 13.3299];
rone=rone.*0.01;
rtwo=rtwo.*0.01;
%Create vectors with areas used in performance calculations
Aone=[324.789; 216.650; 205.222; 193.331; 181.811; 171.592;
  161.001; 151.339; 177.631];
Atwo=[241.362; 165.832; 158.120; 150.038; 142.327; 134.895;
  126.813; 117.615; 138.240];
Aone=Aone.*0.01^2;
Atwo=Atwo.*0.01^2;
%Interpolate data to radial coordinates in rone and rtwo
Dsamp=D(:,1);
Dint=interp1(Dsamp, D, rone);
Esamp=E(:,1);
Eint=interp1(Esamp, E, rtwo);
num=0;
denom=0;
for i=1:9;
    numi=((Dint(i,Ptotcol))^(.4/1.4))*Dint(i,rhocol)*Dint(i,
        ucol)*Aone(i,1);
    denomi=Dint(i,rhocol)*Dint(i,ucol)*Aone(i,1);
    num=num+numi;
    denom=denom+denomi;
end
Pavgstn1=(num/denom)^(1.4/.4);
num=0;
denom=0;
for i=1:9;
    numi=((Eint(i,Ptotcol))^(.4/1.4))*Eint(i,rhocol)*Eint(i,
        ucol)*Atwo(i,1);
    denomi=Eint(i,rhocol)*Eint(i,ucol)*Atwo(i,1);
    num=num+numi;
    denom=denom+denomi;
end
Pavgstn2=(num/denom)^(1.4/.4);
num=0;
denom=0;
for i=1:9;
    numi=Dint(i,Ttotcol)*Dint(i,rhocol)*Dint(i,ucol)*Aone(i,1);
    denomi=Dint(i,rhocol)*Dint(i,ucol)*Aone(i,1);

```

```

        num=num+numi;
        denom=denom+denomi;
    end
    Tavgstn1=(num/denom);
    num=0;
    denom=0;
    for i=1:9;
        numi=Eint(i,Ttotcol)*Eint(i,rhocol)*Eint(i,ucol)*Atwo(i,1);
        denomi=Eint(i,rhocol)*Eint(i,ucol)*Atwo(i,1);
        num=num+numi;
        denom=denom+denomi;
    end
    Tavgstn2=(num/denom);
    rake_FPR=Pavgstn2/Pavgstn1
    slice_FPR=Ptottwo/Ptotone
    rake_Eff=((rake_FPR^(.4/1.4))-1)/(Tavgstn2/Tavgstn1-1)
    slice_Eff=((slice_FPR^(.4/1.4))-1)/(Ttottwo/Ttotone-1)
    slice_mdot_corr=mdot*((Ttotone/288.15)^(1/2)/(Ptotone/101325))
    rake_mdot_corr=mdot*((Tavgstn1/288.15)^(1/2)/(Pavgstn1/101325))
    mdot
    Ptotone
    Ptottwo
    Ttotone
    Ttottwo
    Pavgstn1
    Pavgstn2
    Tavgstn1
    Tavgstn2
    %
    OUT=horzcat(rake_mdot_corr, rake_FPR, rake_Eff,
        slice_mdot_corr, slice_FPR, slice_Eff, mdot);
%output space-delimited, theta-averaged, data for tecplot
    dlmwrite(fileout,OUT,'delimiter',' ','precision',18);

```